Marine Geology 424 (2020) 106168

Contents lists available at ScienceDirect

Marine Geology

journal homepage: www.elsevier.com/locate/margo

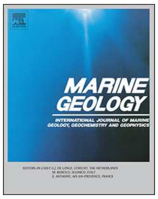

Rethinking the chronology of early Paleogene sediments in the western North Atlantic using diatom biostratigraphy

Jakub Witkowski[a,*], David M. Harwood[b], Bridget S. Wade[c], Karolina Bryłka[d]

[a] *Institute of Marine and Environmental Sciences, University of Szczecin, ul. Mickiewicza 18, 70-383 Szczecin, Poland*
[b] *Department of Earth and Atmospheric Sciences, University of Nebraska-Lincoln, Lincoln, NE 68588-0340, USA*
[c] *Department of Earth Sciences, University College of London, Gower Street, London WC1E 6BT, United Kingdom*
[d] *Department of Geology, Faculty of Science, Lund University, Sölvegatan 12, Lund, Sweden*

ARTICLE INFO

Editor: Edward Anthony

ABSTRACT

Ocean Drilling Program (ODP) Site 1051 (Blake Nose, western North Atlantic) is of crucial importance for reconstructing diatom evolution and biosiliceous sedimentation patterns through the early Cenozoic period of extreme greenhouse warmth followed by the progressive global cooling. The magnetostratigraphy in Hole 1051A, however, has been subject to divergent interpretations resulting in multi-million-year age control uncertainties, especially for events surrounding the early to middle Eocene transition. To resolve these uncertainties, we compare the stratigraphy of Hole 1051A to the neighboring Holes 1050A, C. We compile the published biomagnetostratigraphic data for both sites and identify three possible magnetostratigraphic solutions for Hole 1051A, the difference being the number of hiati and their duration. In order to identify the most plausible magnetostratigraphic solution for Hole 1051A, we employ the graphic correlation method, in which we compare the depth of individual magnetic reversals in both study sites against an independent proxy, i.e., 49 diatom evolutionary events identified in Holes 1050A,C and 1051A. The distribution of diatom bioevents lends strong support to the presence of two major hiati in both study sites: the upper hiatus juxtaposes magnetozone C21n on C22n, and the lower hiatus juxtaposes magnetozone C23n on C24n, eliminating the record of the initial part of the Early Eocene Climatic Optimum. Diatom, calcareous nannofossil and foraminiferal biostratigraphic markers also indicate that Hole 1051A terminated within magnetozone C28n rather than C27n. This age interpretation is strongly supported by the alignment of high-resolution weight percent biogenic SiO_2 records from both study sites. The revised age models developed here for Holes 1050A,C and 1051A have profound consequences for interpretations of western North Atlantic paleoceanographic and paleoclimatic history through the early Paleogene. We propose a revised labelling of the early Eocene carbon cycle perturbations identified to date in Hole 1051A, and show how published Blake Nose $\delta^{30}Si$ records change when data from Sites 1050 and 1051 are rescaled to the age models proposed herein. We emphasize that these refinements to the stratigraphy of Sites 1050 and 1051 are based on a study of diatom bioevents, which are here identified and calibrated to the Geomagnetic Polarity Timescale. This successful application of diatom biostratigraphy is a substantial advance toward their future utility in providing high-resolution age control for Paleogene deep-sea sites.

1. Introduction

Reconstructing climatic events of the warmer-than-present early Paleogene Period is of central importance to understanding and forecasting the behavior of the ocean-atmosphere system in our rapidly warming world. More than fifty years of deep-sea drilling has revealed numerous records of the key early Cenozoic climatic events, which are often viewed as analogs for the present anthropogenic global warming, including the Paleocene-Eocene Thermal Maximum (PETM) and the numerous transient warming events of the Early Eocene Climatic Optimum (EECO) (e.g., Cramer et al., 2003; Nicolo et al., 2007; Westerhold et al., 2018). The quality of these records, however, varies depending on the presence or absence of major sedimentary gaps, some of which cover large areas of the ocean floor. The most pronounced of these is the hiatus spanning the Early-Middle Eocene Transition (EMET; Aubry, 1995). Indeed, both deep-sea and onshore sites that do preserve EMET are sparse (Bornemann et al., 2016; Cappelli et al., 2019).

Unusually expanded early Paleogene successions were recovered

---

[*] Corresponding author.
E-mail address: jakub.witkowski@usz.edu.pl (J. Witkowski).

https://doi.org/10.1016/j.margeo.2020.106168
Received 16 December 2019; Received in revised form 26 February 2020; Accepted 27 February 2020

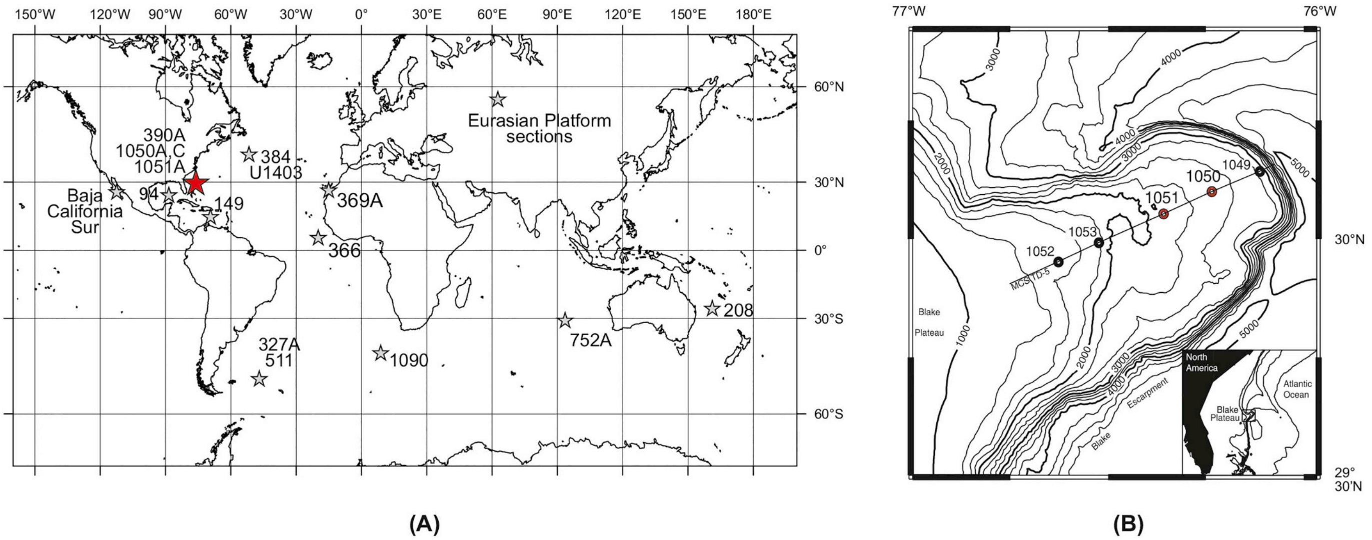

Fig. 1. A. Location of Blake Nose (red star), and deep-sea and onshore sites considered in this study for comparative purposes (grey stars). Base map: Ocean Drilling Stratigraphic Network, www.odsn.de. B. Location of study sites on Blake Nose. Modified from Norris et al. (1998a). (For interpretation of the references to color in this figure legend, the reader is referred to the web version of this article.)

Table 1

Intervals examined for this study in ODP Holes 1050A,C, and 1051A. Site data from Norris et al. (1998c, 1998d).

Hole	Latitude	Longitude	Water depth	Cores examined	Study interval (cmbsf)	Number of samples examined
1050A	30°06′N	76°14.1′W	2299.8	1050A-2H through 1050A-36X	11.04–314.90	35
1050C	30°06′N	76°14.1′W	2296.5	1050C-2R through 1050C-4R	328.07–336.13	3
1051A	30°03.17′N	76°21.46′W	1982.7	1051A-15H through 1051A-73X	129.36–643.20	59
Total: 97 samples						

from the western North Atlantic, at Ocean Drilling Program (ODP) Sites 1050 and 1051 (Fig. 1; Table 1), drilled as part of the Blake Nose Paleoceanographic Transect during ODP Leg 171B. The transect was drilled off northern Florida to investigate Cretaceous and Paleogene changes in circulation of the western North Atlantic Ocean (Norris et al., 1998a). Numerous studies have targeted the Paleocene through early Eocene interval at Site 1051 (e.g., Bains et al., 1999, 2000; Holmes et al., 2004; Cramer et al., 2003; Luciani and Giusberti, 2014; Luciani et al., 2016, 2017; Renaudie et al., 2018), and numerous carbon cycle perturbations have been identified. However, contrasting views have been expressed with regard to magnetostratigraphy, biostratigraphy, and the presence or absence of major stratigraphic discontinuities at Site 1051. For instance, the normal polarity interval immediately subjacent to the recovery gap between ~380 and 390 mbsf is interpreted either as magnetozone C22n or as magnetozone C23n (Ogg and Bardot, 2001 versus Luciani et al., 2016, 2017). These divergent interpretations result in age control uncertainties amounting to several million years. We hypothesize that these discrepancies could be resolved by a close comparison of the overlapping stratigraphic successions cored at Site 1051, and the neighboring Site 1050.

The main aim of this study is to develop a consistent biomagnetostratigraphic age model for Site 1051, which will enable a robust age control for future paleoceanographic studies in the western North Atlantic region. To this end, we (1) compile the available biomagnetostratigraphic data for the overlapping interval of Sites 1050 and 1051; (2) wherever available, check biostratigraphic datums against their published polarity patterns; (3) verify the resultant chron assignments by performing graphic correlation (e.g., Edwards, 1995) and testing the resultant line of correlation (LOC) against an independent biostratigraphic proxy, i.e., diatom bioevents. Finally, we (4) test the alignment of published geochemical records from Holes 1050A,C and 1051A against one another.

1.1. *Early Paleogene deep-sea diatoms in biostratigraphy - a historical perspective*

Early Paleogene diatoms are generally understudied (for a broader perspective, see Witkowski, 2018). Paradoxically, however, the reason for the scarcity of data on diatom evolution through the early Paleogene (e.g., Barron et al., 2015), has been pragmatic rather than scientific, namely the absence of diatomists on numerous ODP and Integrated Ocean Drilling Program (IODP) expeditions, including Leg 171B. Although Paleogene diatoms were reported to occur at all Leg 171B sites (Norris et al., 1998b, 1998c, 1998d, 1998e, 1998f), no large-scale diatom studies were undertaken to date (see Sanfilippo and Blome, 2001, for a radiolarian perspective). Thus far, the only papers that focused on Blake Nose (hereafter BN) diatoms targeted specific problems rather than the broad picture of the diatom record (Holmes et al., 2004; Witkowski et al., 2014; Renaudie et al., 2018; Witkowski, 2018). Considering the large gaps in our current understanding of diatom evolution through the Cenozoic, and the growing interest in diatom involvement in the key biogeochemical cycles in deep time (e.g., Penman, 2016; Conley et al., 2017), the early Paleocene through late Eocene BN diatom record represents a true Rosetta Stone for reconstructing the diatom depositional history.

As with other marine microfossil groups, diatom biostratigraphy underwent a rapid development since the advent of scientific deep-sea drilling in the late 1960s (for a broader perspective, see Scherer et al., 2007). The earliest deep-sea Paleogene diatom zonations (Fig. 2A–B; for calculations used to plot Fig. 2 see Table S1 in the online Supplementary Materials) were based on Southern Ocean Deep Sea Drilling Project (DSDP) cores from the Falkland Plateau (Hole 327A - Gombos, 1977) and Lord Howe Rise (Hole 208 - DePrado and Ling, 1981) (Fig. 1A). Although both these sites offer excellent diatom preservation, they represent short intervals of geological time, spanning ~63–60 Ma (Hole 208) and ~60–57 Ma (Hole 327A). Their utility as reference sections is

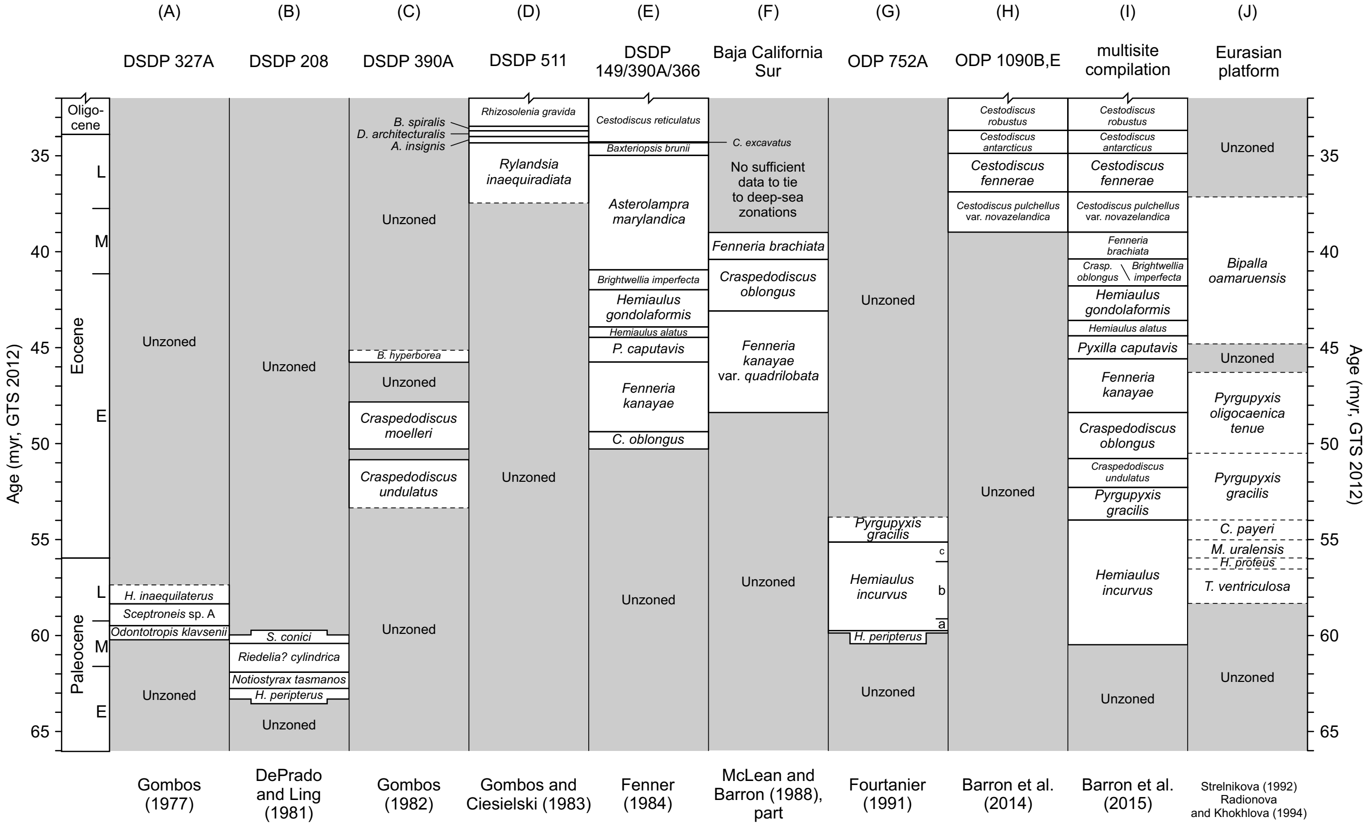

Abbreviations: *A.* = *Asterolampra*; *B.* = *Brightwellia*; *C.* = *Coscinodiscus*; *Crasp.* = *Craspedodiscus*; *D.* = *Distephanosira*; *H.* = *Hemiaulus*; *M.* = *Moisseevia*; *P* = *Pyrgupyxis*; *Rh.* = *Rhizosolenia*; *S.* = *Stephanopyxis*; *T.* = *Trinacria*.

Fig. 2. Summary of existing diatom zonations for the early Paleogene, based on deep-sea (columns A–E, G–I) and onshore sites (columns F and J). Dashed lines in columns A, C, D and G indicate zonal boundaries that lack a formal definition. In column J, dashed lines indicate tentative correlation to the deep-sea zonations. Zonal boundaries in columns F, H–J plotted using data from Barron et al. (2015). For depths and calculated ages of the zonal boundaries in columns A–E, G, see Table S1 in the online Supplementary materials.

also hindered by discontinuous recovery due to spot-coring (Hole 327A; Barker et al., 1977) and because of pervasive silicification (Hole 208; Burns et al., 1973). Further, subsequent work has shown that except for *Hemiaulus peripterus* and *H. inaequilaterus*, the taxa chosen as zonal markers by both Gombos (1977) and DePrado and Ling (1981) were most likely endemic and thus proved to have poor biostratigraphic utility beyond the Southern Ocean. Fourtanier (1991) was the first to propose a deep-sea diatom-based subdivision of the Paleocene-Eocene transition (Fig. 2G), based on the Indian Ocean ODP Hole 752A (Fig. 1A). Her biostratigraphic zonation relies on cosmopolitan taxa as zonal indicators. The zones, however, differ considerably in temporal span (Fig. 2G). For instance, Fourtanier's *Hemiaulus incurvus* Zone spans ~5 myrs, but includes three subzones that potentially enable a more precise correlation. In contrast, her *H. peripterus* Zone represents a narrow time interval (~60.3 through 60 Ma) within the late middle Paleocene (Fig. 2G). The subdivision of lower Eocene sediments in the deep-sea was first proposed by Gombos (1982) (Fig. 2C), who tentatively defined three zones for Hole 390A (Fig. 1A). Each zone, however, was bracketed by unzoned intervals (Fig. 2C). Partly building on Gombos (1982) subdivisions, Fenner (1984) integrated data from a number of Caribbean (Holes 94, 149; Fig. 1A) and Atlantic sites (Holes 366, 369A, 390A; Fig. 1A) in what was the first continuous low-latitude diatom biostratigraphic zonation spanning the interval from ~50 Ma in the early Eocene to the late Oligocene (Fig. 2E). This included 10 zones for the Eocene, yielding an average temporal resolution of ~1.6 myr per zone when compared to the timescale of Gradstein et al. (2012; hereafter GTS2012). An alternative zonation for the late early and middle Eocene was proposed by McLean and Barron (1988) (Fig. 2F), based on onshore successions exposed in Baja California Sur (Fig. 1A). Two diatom zonations were developed for the upper Eocene to date. Gombos and Ciesielski (1983) (Fig. 2D) proposed a series of narrowly-spaced zones based on the Falkland Plateau DSDP Hole 511 (Fig. 1A). Barron et al. (2014) developed an alternative zonation for the upper Eocene (Fig. 2H), composed of four zones based on ODP Site 1090 (Fig. 1A), drilled on Agulhas Ridge.

Elements of the four zonations, listed in stratigraphic order: Fourtanier (1991), Fenner (1984), McLean and Barron (1988) and Barron et al. (2014) were subsequently integrated in the Barron et al. (2015) study, which represents a comprehensive perspective on Eocene deep-sea diatom and silicoflagellate biostratigraphy. The combined zonation presented by Barron et al. (2015) (Fig. 2I) comprises 14 zones spanning late middle Paleocene through terminal Eocene, with an average duration of ~1.9 myr per zone. Further, the zonation by Barron et al. (2015) is tentatively correlated to the Russian Platform diatom zones (Fig. 2J), first developed by Strelnikova (1992) and subsequently expanded by Radionova and Khokhlova (1994). In their comprehensive review, however, Barron et al. (2015) provided no comments on diatom paleobiogeography and its possible impacts on biostratigraphic zonations, including isochroneity or diachroneity of diatom datums.

Notions of diachroneity and paleobiogeography, recognized and appreciated for decades in other marine microfossil groups, are only recently being introduced in Paleogene diatom biostratigraphy (Witkowski, 2018). Also, early Paleogene diatom biostratigraphy almost invariably relies on zones rather than evolutionary events (see Cody et al., 2008 for a Neogene Southern Ocean diatom perspective). Consequently, diatoms are commonly viewed as unsuitable for high-

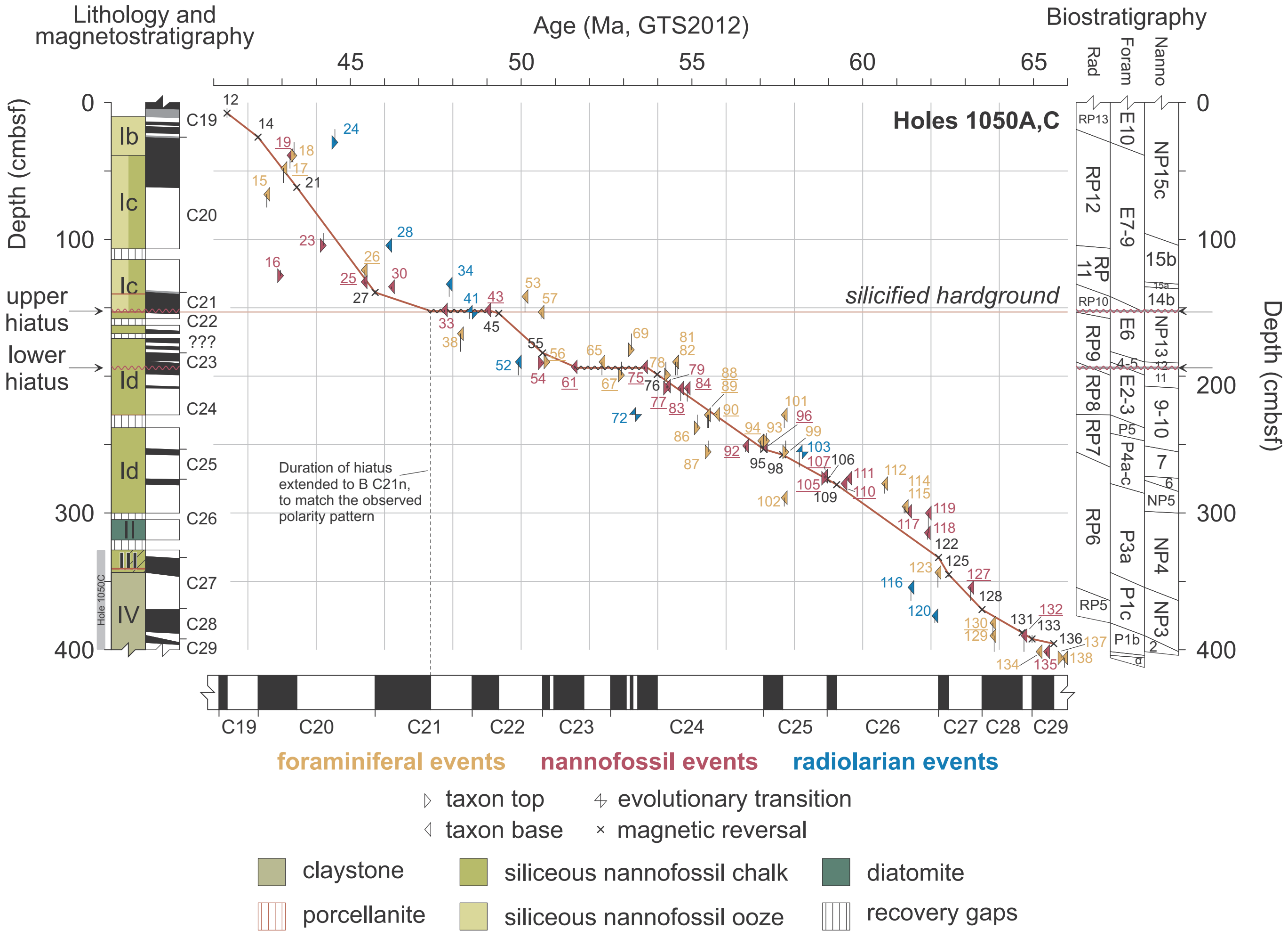

Fig. 3. Age-depth plot for Holes 1050A,C. For list of tiepoints and references see Tables 2 (biostratigraphy) and 4 (magnetostratigraphy). Lithology column based on data from Norris et al. (1998c). Magnetostratigraphy follows Ogg and Bardot (2001), except for Chrons C22r through C24n, which conform to age control Option 3 presented herein. Angled lines in polarity column represent error depths for each reversal. Underlined numbers indicate tiepoints that are consistent with polarity patterns. An oversized version of this plot is available as Fig. S1 in the online Supplementary materials.

resolution stratigraphic correlation in deep-sea Paleocene through Eocene sedimentary successions. Our long-term goal is therefore to promote early Paleogene diatoms as a means of high-fidelity stratigraphic correlation for siliceous microfossil-rich intervals.

2. Materials and methods

Both study sites were drilled on Blake Nose (Fig. 1), an ENE-trending projection of the Blake Plateau in the western North Atlantic Ocean. Site 1050 is the deeper site included in this study (~2300 m water depth, Table 1; Norris et al., 1998c). Most of the ~420 m Paleogene siliceous microfossil-bearing succession is composed of siliceous nannofossil ooze and chalk (lithologic unit I) (Fig. 3). Lithologic unit II is a narrow interval of calcareous diatomite, and lithologic unit III is composed of claystone. This study is based on the entire succession cored in Hole 1050A (Table 1). In Hole 1050C (Fig. 3), siliceous microfossil preservation is confined to Cores 1050C-1R through -3R (Table 1). In the stratigraphic discussion that follows, however, we consider Cores 1050C-1R through -10R, i.e., the basal Paleocene record (Norris et al., 1998c).

Site 1051 represents the shallower site included in this study (~1983 m water depth, Table 1; Norris et al., 1998d). Except for a few narrow dissolution intervals, siliceous microfossils occur throughout the succession cored at Site 1051 (Fig. 4). Hole 1051A recovered ~650 m of siliceous nannofossil ooze and chalk (lithologic units I and III), and was terminated within lithologic unit IV, composed of claystone (Fig. 4). A silicified interval distinguished as lithologic unit II was drilled through without coring (Norris et al., 1998d). In the present study, we examined Cores 1051A-15H through -73X (Table 1), i.e., those cores that stratigraphically overlap with the Paleogene succession cored at Site 1050, as indicated by the shipboard biomagnetostratigraphic data (Norris et al., 1998c, 1998d).

2.1. Revised depth scales

Most Leg 171B cores are characterized by considerable post-drilling expansion (Norris et al., 1998c, 1998d; marked with asterisks in the relevant figures in the present paper). At the same time, shipboard composite depth scales are either tentative (Site 1050; Norris et al., 1998c), or restricted to selected intervals (Site 1051) (Norris et al., 1998d). In order to avoid overlapping sample depths for the cores considered in this study, we constructed a revised depth scale for each hole (cmbsf = compacted meters below sea floor). This was achieved by establishing a compaction factor for each core. Using the compaction factor and core-top depth in meters below sea floor (mbsf), the depth of each sample within the respective core was proportionally reduced until all overlapping sample depths were eliminated. Compaction factors are tabulated for both study sites in the Supplementary Tables

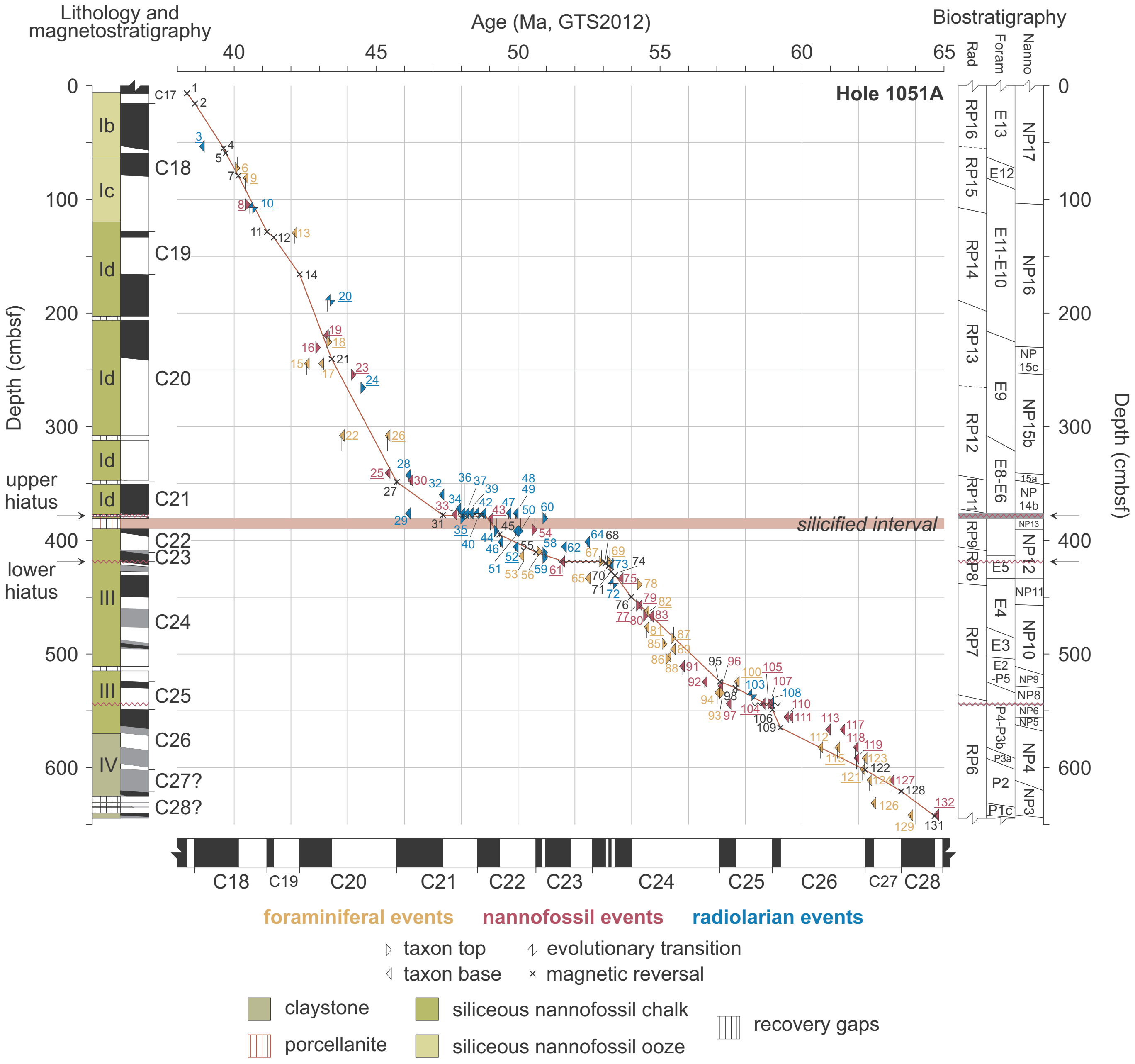

Fig. 4. Age-depth plot for Hole 1051A. For list of tiepoints and references see Tables 3 (biostratigraphy) and 5 (magnetostratigraphy). Lithology column based on data from Norris et al. (1998d). Magnetostratigraphy conforms to age control Option 3 presented herein. Angled lines in polarity column represent error depths for each reversal. Underlined numbers indicate tiepoints that are consistent with polarity patterns. An oversized version of this plot is available as Fig. S2 in the online Supplementary materials.

S2–S3.

2.2. Sample processing and slide preparation techniques

Samples for this study were freeze-dried and then treated with 10% HCl and 37% H_2O_2, with intermittent washes in deionized water. Except for freeze-drying, the sample and light microscope (LM) slide preparation techniques closely followed that used in studies by Witkowski et al. (2012, 2014).

2.3. Microscope examination

Slides were examined using either Zeiss Axio.A1, or Leica DMLB microscopes, with oil immersion ×100 plan-apochromatic lenses. Digital cameras used for photographic documentation were either Zeiss MRc (fitted on Axio.A1 microscope), or Nikon Digital Sight Fi-1 (fitted on Leica microscope). Additionally, Differential Interference Contrast (DIC) illumination was used for all slides examined with Zeiss Axio.A1 microscope. Diatom counts were performed following the convention proposed by Schrader and Gersonde (1978). Those diatom taxa that are characterized by especially poorly resolved taxonomy, were only identified to family level (e.g., early Cymatosiraceae). In range charts (Tables S4–S5 in the online Supplementary Materials), we report the number of valves counted in the slide area examined. "+" denotes the presence of identifiable valve fragments of the respective species. List of diatom taxa identified in the present study is also available as part of the online Supplementary materials. A detailed taxonomic account of the diatom assemblages from Sites 1050 and 1051 will be published

Table 2

Holes 1050A,C biostratigraphic tiepoints from published records. Abbreviations: Foram – foraminiferal bioevents; nanno – nannofossil bioevents; rad – radiolarian bioevents; Min depth – minimum depth; Max depth – maximum depth; mbsf – meters below sea floor; cmbsf – compacted meters below sea floor. GTS2012 – timescale of Gradstein et al. (2012); B – taxon range base; T – taxon range top; X – evolutionary transition.

#	Event	Microfossil group	Zone	Min depth (mbsf)	Min depth (cmbsf)	Max depth (mbsf)	Max depth (cmbsf)	Average depth (mbsf)	Average depth (cmbsf)	Consistent with polarity?	Age (Ma, GTS2012)	Reference	GTS2012 calibration	Comments
15	B *Globigerinatheka index*	Foram	Within E10	67.50	67.09	76.66	76.54	72.08	71.82	No	42.64	Norris et al. (1998c)	Gradstein et al. (2012)	
16	T *Nannotetrina fulgens*	Nanno	B NP16	122.47	122.47	126.54	126.54	124.51	124.51	No	42.87	Norris et al. (1998c)	Gradstein et al. (2012)	
17	B *Morozovelloides lehneri*	Foram	Within E10	48.34	48.09	57.83	58.58	53.09	53.34	C20n	43.15	Norris et al. (1998c)	Gradstein et al. (2012)	
18	T *Morozovella aragonensis*	Foram	B E10	29.61	29.07	38.72	38.59	34.17	33.83	No	43.26	Norris et al. (1998c)	Gradstein et al. (2012)	
19	B *Reticulofenestra umbilica*	Nanno	Within NP16	38.72	38.59	48.34	48.09	43.53	43.34	No	43.32	Norris et al. (1998c)	Gradstein et al. (2012)	
23	T *Chiasmolithus gigas*	Nanno	B NP15c	95.93	95.57	104.42	104.42	100.18	100.00	Mid C20r	44.12	Janus Database	Gradstein et al. (2012)	
24	T *Theocotyle venezuelensis*	Rad	Within RP13	20.18	19.58	29.61	29.07	24.90	24.33	No	44.46	Norris et al. (1998c)	Norris et al. (2014a)	
25	B *Chiasmolithus gigas*	Nanno	B NP15b	131.08	131.08	132.72	132.72	131.90	131.90	Lower C20r	45.49	Norris et al. (1998c)	Gradstein et al. (2012)	
26	B *Turborotalia possagnoensis*	Foram	Within E8	122.47	122.47	132.72	132.72	127.60	127.60	C20r	45.49	Norris et al. (1998c)	Gradstein et al. (2012)	
28	B *Eusyringium lagena*	Rad	B RP12	104.42	104.42	106.52	106.52	105.47	105.47	No	46.21	Norris et al. (1998c)	Norris et al. (2014a)	
30	B *Nannotetrina fulgens*	Nanno	B NP15a	134.65	134.65	136.12	136.12	135.39	135.39	No	46.29	Norris et al. (1998c)	Gradstein et al. (2012)	
33	B *Blackites inflatus/ Rhabdosphaera inflata*	Nanno	B NP14b	151.77	151.60	153.37	153.19	152.57	152.40	C21n	47.84	Janus Database	Gradstein et al. (2012)	Probably not the actual base; range consistent with polarity pattern.
34	B *Dictyoprora mongolfieri*	Rad	B RP11	132.72	132.72	141.80	141.80	137.26	137.26	No	47.98	Norris et al. (1998c)	Norris et al. (2014a)	
38	B *Turborotalia frontosa*	Foram	B E7b	168.95	168.95	182.16	181.98	175.56	175.47	No	48.31	Norris et al. (1998c)	Gradstein et al. (2012)	
41	X *Theocotyle nigriniae/ Theocotyle cryptocephala*	Rad	B RP10	153.37	153.19	157.95	157.95	155.66	155.57	No	48.57	Norris et al. (1998c)	Norris et al. (2014a)	
43	B *Discoaster sublodoensis*	Nanno	B NP14a	151.77	151.60	153.37	153.19	152.57	152.40	C22n	49.11	Janus Database	Gradstein et al. (2012)	Probably not the actual base; range consistent with polarity pattern. Number of rays unspecified.
52	B *Theocorys anaclasta*	Rad	B RP9	191.82	189.60	199.29	199.29	195.56	194.45	No	50.05	Norris et al. (1998c)	Norris et al. (2014a)	Tentative
53	B *Acarinina cuneicamerata*	Foram	B E7a	141.80	141.80	153.37	153.19	147.59	147.50	No	50.20	Norris et al. (1998c)	Gradstein et al. (2012)	
54	T *Tribrachiatus orthostylus*	Nanno	B NP13	191.82	189.60	190.25	190.24	191.04	189.92	No	50.50	Janus Database	Gradstein et al. (2012)	
56	T *Morozovella subbotinae*	Foram	B E6	182.16	181.98	191.82	189.60	186.99	185.79	C23n.1n	50.67	Norris et al. (1998c)	Gradstein et al. (2012)	
57	B *Acarinina pentacamerata*	Foram	Within E5	153.37	153.19	157.95	157.95	155.66	155.57	No	50.67	Norris et al. (1998c)	Gradstein et al. (2012)	
61	B *Coccolithus crassus*	Nanno	Within NP12	193.24	193.20	194.70	194.64	193.97	193.92	C23n.2n	51.64	Norris et al. (1998c)	Norris et al. (2014b)	Calibration from Site U1410
65	B *Morozovella aragonensis*	Foram	B E5	191.82	189.60	199.29	199.20	195.56	194.40	No	52.54	Norris et al. (1998c)	Gradstein et al. (2012)	
67	T *Morozovella marginodentata*	Foram	Within E4	191.82	189.60	199.29	199.20	195.56	194.40	C24n.1n	52.85	Norris et al. (1998c)	Gradstein et al. (2012)	

(*continued on next page*)

Table 2 (*continued*)

#	Event	Microfossil group	Zone	Min depth (mbsf)	Min depth (cmbsf)	Max depth (mbsf)	Max depth (cmbsf)	Average depth (mbsf)	Average depth (cmbsf)	Consistent with polarity?	Age (Ma, GTS2012)	Reference	GTS2012 calibration	Comments
69	T *Morozovella lensiformis*	Foram	Within E4	168.95	168.95	182.16	181.98	175.56	175.47	No	53.14	Norris et al. (1998c)	Gradstein et al. (2012)	
72	X *Pterocodon(?) anteclinata/ Buryella clinata*	Rad	B RP8	228.22	228.01	228.28	228.28	228.25	228.15	–	53.35	Norris et al. (1998c)	Norris et al. (2014a)	
75	B *Discoaster lodoensis*	Nanno	B NP12	193.24	193.20	194.70	194.64	193.97	193.92	C24n.3n	53.70	Norris et al. (1998c)	Gradstein et al. (2012)	
77	T *Tribrachiatus contortus*	Nanno	B NP11	207.39	207.22	208.97	208.77	208.18	208.00	Upper C24r	54.17	Janus Database	Gradstein et al. (2012)	
78	T *Morozovella aequa*	Foram	Within E4	191.82	189.60	199.29	199.20	195.56	194.40	No	54.20	Norris et al. (1998c)	Gradstein et al. (2012)	
79	B *Tribrachiatus orthostylus*	Nanno	Within NP10	207.39	207.22	208.97	208.77	208.18	208.00	Upper C24r	54.37	Norris et al. (1998c)	Gradstein et al. (2012)	
81	B *Morozovella formosa*	Foram	B E4	191.82	189.60	199.29	199.20	195.56	194.40	Bracketing recovery gap	54.61	Norris et al. (1998c)	Gradstein et al. (2012)	
82	B *Morozovella lensiformis*	Foram	Within E3	191.82	189.60	199.29	199.20	195.56	194.40	Bracketing recovery gap	54.61	Norris et al. (1998c)	Gradstein et al. (2012)	
83	B *Tribrachiatus contortus*	Nanno	Within NP10	208.97	208.77	218.26	217.97	213.62	213.37	Upper C24r	54.76	Janus Database	Gradstein et al. (2012)	
84	B *Discoaster diastypus*	Nanno	Within NP10	208.97	208.77	218.69	218.42	213.83	213.59	Upper C24r	54.95	Janus Database	Gradstein et al. (2012)	
86	T *Morozovella velascoensis*	Foram	B E3	228.28	228.28	237.78	237.77	233.03	233.03	Bracketing recovery gap	55.20	Norris et al. (1998c)	Gradstein et al. (2012)	
87	T *Morozovella acuta*	Foram	Within E2	249.12	247.28	255.38	255.38	252.25	251.33	No	55.39	Norris et al. (1998c)	Gradstein et al. (2012)	
88	B *Morozovella gracilis*	Foram	Within E2	228.28	228.28	237.78	237.77	233.03	233.03	Mid C24r	55.39	Norris et al. (1998c)	Gradstein et al. (2012)	
89	B *Morozovella marginodentata*	Foram	Within E2	228.28	228.28	237.78	237.77	233.03	233.03	Mid C24r	55.54	Norris et al. (1998c)	Gradstein et al. (2012)	
90	B *Pseudohastigerina wilcoxensis*	Foram	B E2	228.22	228.01	228.28	228.28	228.25	228.15	Mid C24r	55.81	Norris et al. (1998c)	Gradstein et al. (2012)	
92	B *Campylosphaera eodela*	Nanno	Within NP9	250.92	250.92	255.38	255.38	253.15	253.15	Lower C24r	56.66	Norris et al. (1998c)	Gradstein et al. (2012)	
93	T *Globanomalina pseudomenardii*	Foram	B P5	242.01	241.70	249.12	247.28	245.57	244.49	No	57.10	Norris et al. (1998c)	Gradstein et al. (2012)	
94	B *Morozovella subbotinae*	Foram	Within P4c	249.12	247.28	255.38	255.38	252.25	251.33	Basal C24r	57.10	Norris et al. (1998c)	Gradstein et al. (2012)	As secondary marker for base P5
96	B *Discoaster multiradiatus*	Nanno	B NP9	250.92	250.92	255.38	255.38	253.15	253.15	C25n	57.21	Norris et al. (1998c)	Gradstein et al. (2012)	No indication of abundance
99	T *Acarinina mckannai*	Foram	Within P4c	249.12	247.28	255.38	255.38	252.25	251.33	No	57.66	Norris et al. (1998c)	Gradstein et al. (2012)	
101	B *Acarinina coalingensis*	Foram	Within P4b	228.28	228.28	237.78	237.77	233.03	233.03	No	57.79	Norris et al. (1998c)	Gradstein et al. (2012)	
102	B *Morozovella aequa*	Foram	Within P4b	298.11	288.87	300.08	295.15	299.10	292.01	No	57.79	Norris et al. (1998c)	Gradstein et al. (2012)	
103	X *Bekoma campechensis/ Bekoma bidartensis*	Rad	B RP7	255.38	255.38	266.82	266.49	261.10	260.94	–	58.23	Norris et al. (1998c)	Norris et al. (2014a)	
105	T *Heliolithus kleinpellii*	Nanno	Within NP7	273.17	273.14	274.65	274.62	273.91	273.88	Basal C25r	58.80	Janus Database	Gradstein et al. (2012)	Approximating B NP8
107	B *Discoaster mohleri*	Nanno	B NP7	273.17	273.14	274.65	274.62	273.91	273.88	Basal C25r	58.97	Norris et al. (1998c)	Gradstein et al. (2012)	
110	B *Heliolithus kleinpellii*	Nanno	B NP6	278.57	278.49	284.61	284.36	281.59	281.43	Upper C26r	59.54	Janus Database	Gradstein et al. (2012)	

(*continued on next page*)

Table 2 (*continued*)

#	Event	Microfossil group	Zone	Min depth (mbsf)	Min depth (cmbsf)	Max depth (mbsf)	Max depth (cmbsf)	Average depth (mbsf)	Average depth (cmbsf)	Consistent with polarity?	Age (Ma, GTS2012)	Reference	GTS2012 calibration	Comments
111	B *Sphenolithus anarrhopus*	Nanno	Within NP5	274.65	274.62	276.11	276.05	275.38	275.33	No	59.68	Norris et al. (1998c)	Gradstein et al. (2012)	
112	B *Globanomalina pseudomenardii*	Foram	B P4a	278.57	278.49	285.95	285.68	282.26	282.09	No	60.73	Norris et al. (1998c)	Gradstein et al. (2012)	
114	B *Igorina albeari*	Foram	B P3b	298.11	295.29	300.08	300.08	299.10	297.68	No	61.33	Norris et al. (1998c)	Gradstein et al. (2012)	
115	B *Morozovella velascoensis*	Foram	Within P3a	298.11	295.29	300.08	300.08	299.10	297.68	No	61.33	Norris et al. (1998c)	Gradstein et al. (2012)	As secondary marker for base P3b
116	B *Bekoma campechensis*	Rad	B RP6	354.41	354.41	364.10	364.10	359.26	359.26	–	61.50	Norris et al. (1998c)	Norris et al. (2014a)	
117	B *Fasciculithus tympaniformis*	Nanno	B NP5	298.82	298.82	300.08	300.08	299.45	299.45	No	61.51	Norris et al. (1998c)	Gradstein et al. (2012)	Indicates C26r
118	B *Sphenolithus primus*	Nanno	Within NP4	314.61	314.52	319.72	319.72	317.17	317.12	No	61.98	Norris et al. (1998c)	Gradstein et al. (2012)	Indicates lowermost C26r
119	B *Chiasmolithus bidens*	Nanno	Within NP4	300.08	300.08	314.61	314.52	307.35	307.30	No	62.07	Norris et al. (1998c)	Gradstein et al. (2012)	
120	B *Buryella tetradica*	Rad	B RP5	375.32	375.20	380.36	380.36	377.84	377.78	–	62.20	Norris et al. (1998c)	Norris et al. (2014a)	
123	B *Morozovella angulata*	Foram	B P3a	343.46	343.46	354.41	354.41	348.94	348.94	No	62.29	Norris et al. (1998c)	Gradstein et al. (2012)	Indicates C26r/C27n transition
127	B *Ellipsolithus macellus*	Nanno	B NP4	354.41	354.41	364.10	364.10	359.26	359.26	C27r	63.25	Norris et al. (1998c)	Gradstein et al. (2012)	Indicates C27r
129	B *Praemurica inconstans*	Foram	B P1c	389.68	389.68	401.37	401.37	395.53	395.53	Upper C28n	63.90	Norris et al. (1998c)	Gradstein et al. (2012)	As secondary marker for base P1c
130	B *Globanomalina compressa*	Foram	B P1c	380.36	380.36	389.68	389.68	385.02	385.02	C28n	63.90	Norris et al. (1998c)	Gradstein et al. (2012)	
132	B *Chiasmolithus danicus*	Nanno	B NP3	389.68	389.68	401.37	401.37	395.53	395.53	C28r	64.81	Norris et al. (1998c)	Gradstein et al. (2012)	Indicates C28r
134	B Subbotina triloculinoides	Foram	B P1b	401.37	401.37	404.10	404.10	402.74	402.74	–	65.25	Norris et al. (1998c)	Gradstein et al. (2012)	
135	B *Cruciplacolithus tenuis*	Nanno	B NP2	401.37	401.37	404.10	404.10	402.74	402.74	–	65.47	Norris et al. (1998c)	Gradstein et al. (2012)	
137	T *Parvularugoglobigerina eugubina*	Foram	B P1a	404.10	404.10	405.92	405.92	405.01	405.01	–	65.72	Norris et al. (1998c)	Gradstein et al. (2012)	
138	B *Parvularugoglobigerina eugubina*	Foram	B Pα	405.92	405.92	412.96	412.96	409.44	409.44	–	66.00	Norris et al. (1998c)	Gradstein et al. (2012)	

Table 3
Hole 1051A biostratigraphic tiepoints from published records. Abbreviations: Foram – foraminiferal bioevents; Nanno – nannofossil bioevents; Rad – radiolarian bioevents; Min depth – minimum depth; Max depth – maximum depth; mbsf – meters below sea floor; cmbsf – compacted meters below sea floor. GTS2012 – timescale of Gradstein et al. (2012); B – taxon range base; T – taxon range top; X – evolutionary transition.

#	Event	Microfossil group	Zone	Min depth (mbsf)	Min depth (cmbsf)	Max depth (mbsf)	Max depth (cmbsf)	Average depth (mbsf)	Average depth (cmbsf)	Consistent with polarity?	Age (Ma, GTS2012)	Reference	GTS2012 calibration	Comments
3	B *Lithocyclia aristotelis* gr.	Rad	Within RP16	53.62	53.28	55.20	55.17	15.65	54.23	C18n	38.95	Sanfilippo and Blome (2001)	Norris et al. (2014a)	Chosen as approximation of B RP16
6	T *Orbulinoides beckmanni*	Foram	B E13	62.90	62.77	72.59	72.30	67.75	67.54	C18n.2n	40.03	Norris et al. (1998d)	Gradstein et al. (2012)	Refined for Hole B - Edgar et al. (2010)
8	T *Chiasmolithus solitus*	Nanno	B NP17	103.15	103.13	104.47	104.44	103.81	103.79	Mid C18r	40.40	Mita (2001)	Gradstein et al. (2012)	
9	B *Orbulinoides beckmanni*	Foram	B E12	81.09	81.09	91.02	91.02	86.06	86.06	Upper C18r	40.49	Norris et al. (1998d)	Gradstein et al. (2012)	Refined for Hole B - Edgar et al. (2010)
10	X *Podocyrtis mitra/ Podocyrtis chalara*	Rad	B RP15	107.19	107.13	112.20	112.17	109.70	109.65	C18r	40.65	Sanfilippo and Blome (2001)	Norris et al. (2014a)	Consistent with GTS2012, but not with Nigrini et al. (2006) and Kamikuri et al. (2012)
13	B *Turborotalia pomeroli*	Foram	Within E10	129.81	129.28	138.97	138.80	134.39	134.04	No	42.21	Norris et al. (1998d)	Gradstein et al. (2012)	
15	B *Globigerinatheka index*	Foram	Within E10	244.63	244.40	254.47	254.19	249.55	249.30	No	42.64	Norris et al. (1998d)	Gradstein et al. (2012)	
16	T *Nannotetrina fulgens*	Nanno	B NP16	229.30	229.19	230.43	230.29	229.87	229.74	No	42.87	Mita (2001)	Gradstein et al. (2012)	
17	B *Morozovelloides lehneri*	Foram	Within E10	244.63	244.40	254.47	254.19	249.55	249.30	No	43.15	Norris et al. (1998d)	Gradstein et al. (2012)	
18	T *Morozovella aragonensis*	Foram	B E10	216.00	215.79	225.45	225.39	220.73	220.59	Lower C20n	43.26	Norris et al. (1998d)	Gradstein et al. (2012)	
19	B *Reticulofenestra umbilica*	Nanno	Within NP16	219.46	219.44	221.19	221.16	220.33	220.30	Lower C20n	43.32	Mita (2001)	Gradstein et al. (2012)	
20	X *Podocyrtis sinuosa/ Podocyrtis mitra*	Rad	B RP14	188.91	188.87	198.39	198.39	193.65	193.63	C20n	43.38	Sanfilippo and Blome (2001)	Norris et al. (2014a)	
22	B *Globigerinatheka kugleri*	Foram	B E9	307.74	307.74	321.71	321.53	314.73	314.64	No	43.88	Norris et al. (1998d)	Gradstein et al. (2012)	
23	T *Chiasmolithus gigas*	Nanno	B NP15c	252.85	252.61	254.47	254.19	253.66	253.40	Upper C20r	44.12	Mita (2001)	Gradstein et al. (2012)	
24	T *Theocotyle venezuelensis*	Rad	Within RP13	263.98	263.79	265.69	265.68	264.84	264.74	C20r	44.46	Sanfilippo and Blome (2001)	Norris et al. (2014a)	
25	B *Chiasmolithus gigas*	Nanno	B NP15b	340.83	340.64	341.90	341.90	341.37	341.27	Lower C20r	45.49	Agnini et al. (2014)	Gradstein et al. (2012)	
26	B *Turborotalia possagnoensis*	Foram	Within E8	307.74	307.74	321.71	321.53	314.73	314.64	Lower C20r	45.49	Norris et al. (1998d)	Gradstein et al. (2012)	
28	B *Eusyringium lagena*	Rad	B RP12	342.61	342.61	347.06	347.06	344.84	344.84	No	46.21	Sanfilippo and Blome (2001)	Norris et al. (2014a)	
29	B *Rhopalocanium ornatum*	Rad	Within RP12	376.19	376.19	380.58	380.58	378.39	378.39	No	46.21	Sanfilippo and Blome (2001)	Norris et al. (2014a)	
30	B *Nannotetrina fulgens*	Nanno	B NP15a	347.06	347.06	350.67	350.67	348.87	348.87	No	46.29	Mita (2001)	Gradstein et al. (2012)	
32	X *Theocotyle cryptocephala/ Theocotyle conica*	Rad	Within RP11	359.81	359.81	361.99	361.98	360.90	360.90	–	47.39	Sanfilippo and Blome (2001)	Norris et al. (2014a)	
33	B *Blackites inflatus/ Rhabdosphaera inflata*	Nanno	B NP14b	377.18	377.18	379.77	379.77	378.48	378.48	See comment	47.84	Mita (2001)	Gradstein et al. (2012)	Probably not the actual base; range consistent with polarity pattern.
34	B *Dictyoprora mongolfieri*	Rad	B RP11	372.19	372.19	376.19	376.19	374.19	374.19	No	47.98	Sanfilippo and Blome (2001)	Norris et al. (2014a)	
35	T *Lithochytris archaea*	Rad	Within RP10	376.19	376.19	380.58	380.58	378.39	378.39	C21n/C21r transition	47.98	Sanfilippo and Blome (2001)	Norris et al. (2014a)	

(*continued on next page*)

Table 3 (*continued*)

#	Event	Microfossil group	Zone	Min depth (mbsf)	Min depth (cmbsf)	Max depth (mbsf)	Max depth (cmbsf)	Average depth (mbsf)	Average depth (cmbsf)	Consistent with polarity?	Age (Ma, GTS2012)	Reference	GTS2012 calibration	Comments
36	B *Podocyrtis sinuosa*	Rad	Within RP10	376.19	376.19	380.58	380.58	378.39	378.39	–	48.13	Sanfilippo and Blome (2001)	Norris et al. (2014a)	
37	B *Thyrsocyrtis robusta*	Rad	Within RP10	376.19	376.19	380.58	380.58	378.39	378.39	–	48.27	Sanfilippo and Blome (2001)	Norris et al. (2014a)	
39	B *Theocotyle venezuelensis*	Rad	Within RP10	376.19	376.19	380.58	380.58	378.39	378.39	–	48.42	Sanfilippo and Blome (2001)	Norris et al. (2014a)	
40	X *Lithochytris archaea*/ *Lithochytris vespertilio*	Rad	Within RP10	376.19	376.19	380.58	380.58	378.39	378.39	–	48.57	Sanfilippo and Blome (2001)	Norris et al. (2014a)	Indicates C21/C22 transition
42	B *Spongatractus pachystylus*	Rad	Within RP9	376.19	376.19	380.58	380.58	378.39	378.39	–	48.86	Sanfilippo and Blome (2001)	Norris et al. (2014a)	
43	B *Discoaster sublodoensis*	Nanno	B NP14a	380.60	380.60	390.71	390.68	380.60	380.60	See comment	49.11	Norris et al. (1998d)	Gradstein et al. (2012)	Probably not the actual base; range consistent with polarity pattern. Number of rays unspecified.
44	T *Lamptonium sanfilippoae*	Rad	Within RP9	380.58	380.58	391.80	391.74	386.19	386.16	–	49.16	Sanfilippo and Blome (2001)	Norris et al. (2014a)	
46	B *Thyrsocyrtis rhizodon*	Rad	Within RP9	401.41	401.34	405.87	405.63	403.64	403.48	–	49.46	Sanfilippo and Blome (2001)	Norris et al. (2014a)	
47	B *Podocyrtis diamesa*	Rad	Within RP9	376.19	376.19	380.58	380.58	378.39	378.39	–	49.75	Sanfilippo and Blome (2001)	Norris et al. (2014a)	
48	B *Dictyophimus craticula*	Rad	RP8/RP9 transition	376.19	376.19	380.58	380.58	378.39	378.39	–	50.05	Sanfilippo and Blome (2001)	Norris et al. (2014a)	
49	B *Lamptonium fabaeforme constrictum*	Rad	RP8/RP9 transition	376.19	376.19	380.58	380.58	378.39	378.39	–	50.05	Sanfilippo and Blome (2001)	Norris et al. (2014a)	
50	T *Phormocyrtis cubensis*	Rad	RP8/RP9 transition	380.58	380.58	391.80	391.74	386.19	386.16	–	50.05	Sanfilippo and Blome (2001)	Norris et al. (2014a)	
51	B *Lychnocanoma bellum*	Rad	RP8/RP9 transition	391.80	391.74	396.28	396.08	394.04	393.91	–	50.05	Sanfilippo and Blome (2001)	Norris et al. (2014a)	
52	B *Theocorys anaclasta*	Rad	B RP9	405.87	405.63	409.46	409.09	407.67	407.36	C22r	50.05	Sanfilippo and Blome (2001)	Norris et al. (2014a)	Tentative
53	B *Acarinina cuneicamerata*	Foram	B E7a					413.80	413.66	No	50.20	Luciani and Giusberti (2014)	Gradstein et al. (2012)	
54	T *Tribrachiatus orthostylus*	Nanno	B NP13	380.60	380.60	390.71	390.68	390.71	390.68	No	50.50	Mita (2001)	Gradstein et al. (2012)	
56	T *Morozovella subbotinae*	Foram	B E6					409.80	409.78	No	50.67	Luciani and Giusberti (2014)	Gradstein et al. (2012)	
58	T *Phormocyrts turgida*	Rad	Within RP8	409.46	409.09	410.96	410.91	410.21	410.00	–	50.87	Sanfilippo and Blome (2001)	Norris et al. (2014a)	
59	T *Bekoma bidartensis*	Rad	Within RP8	410.96	410.91	415.51	415.32	413.24	413.11	–	50.87	Sanfilippo and Blome (2001)	Norris et al. (2014a)	
60	T *Bekoma tetradica* s.s.	Rad	Within RP8	376.19	376.19	380.58	380.58	378.39	378.39	No	50.87	Sanfilippo and Blome (2001)	Norris et al. (2014a)	
61	B *Coccolithus crassus*	Nanno	Within NP12	418.97	418.68	428.58	428.31	423.78	423.50	No	51.64	Norris et al. (1998d)	Norris et al. (2014b)	Calibration from Site U1410
62	B *Theocotylissa ficus*	Rad	Within RP8	405.87	405.63	409.46	409.09	407.67	407.36	See comment	51.70	Sanfilippo and Blome (2001)	Norris et al. (2014a)	Inconsistent with polarity pattern from Nigrini et al. (2006)
64	B *Calocyclas hispida*	Rad	Within RP8	401.41	401.34	405.87	405.63	403.64	403.48	–	52.52	Sanfilippo and Blome (2001)	Norris et al. (2014a)	

(*continued on next page*)

Table 3 (*continued*)

#	Event	Microfossil group	Zone	Min depth (mbsf)	Min depth (cmbsf)	Max depth (mbsf)	Max depth (cmbsf)	Average depth (mbsf)	Average depth (cmbsf)	Consistent with polarity?	Age (Ma, GTS2012)	Reference	GTS2012 calibration	Comments
65	B *Morozovella aragonensis*	Foram	B E5					433.50	433.35	No	52.54	Luciani and Giusberti (2014)	Gradstein et al. (2012)	
67	T *Morozovella marginodentata*	Foram	Within E4	409.46	409.09	418.99	418.68	414.23	413.89	C24n.1n	52.85	Norris et al. (1998d)	Gradstein et al. (2012)	
69	T *Morozovella lensiformis*	Foram	Within E4	409.46	409.09	418.99	418.68	414.23	413.89	C24n.1n	53.14	Norris et al. (1998d)	Gradstein et al. (2012)	
72	X *Pterocodon(?) anteclinata/Buryella clinata*	Rad	B RP8	438.16	437.90	439.71	439.66	438.94	438.78	–	53.35	Sanfilippo and Blome (2001)	Norris et al. (2014a)	
73	B *Lamptonium sanfilippoae*	Rad	Within RP7	420.71	420.65	425.14	424.94	422.93	422.80	–	53.35	Sanfilippo and Blome (2001)	Norris et al. (2014a)	
75	B *Discoaster lodoensis*	Nanno	B NP12					433.40	433.26	C24n.3n	53.70	Cramer et al. (2003)	Gradstein et al. (2012)	
77	T *Tribrachiatus contortus*	Nanno	B NP11	456.72	456.54	457.30	457.28	457.01	456.91	Upper C24r	54.17	Cramer et al. (2003)	Gradstein et al. (2012)	
78	T *Morozovella aequa*	Foram	Within E4	438.50	438.48	438.60	438.58	438.55	438.53	No	54.20	Röhl et al. (2003)	Gradstein et al. (2012)	
79	B *Tribrachiatus orthostylus*	Nanno	Within NP10	457.11	457.10	457.30	457.28	457.21	457.19	Upper C24r	54.37	Mita (2001)	Gradstein et al. (2012)	
80	T *Tribrachiatus bramlettei*	Nanno	Within NP10	460.88	460.82	466.88	466.31	463.88	463.56	Upper C24r	54.42	Cramer et al. (2003)	Gradstein et al. (2012)	
81	B *Morozovella formosa*	Foram	B E4	476.56	476.46	486.39	486.07	481.48	481.27	Mid C24r	54.61	Norris et al. (1998d)	Gradstein et al. (2012)	
82	B *Morozovella lensiformis*	Foram	Within E3	462.37	462.19	465.37	464.93	463.87	463.56	Upper C24r	54.61	Röhl et al. (2003)	Gradstein et al. (2012)	
83	B *Tribrachiatus contortus*	Nanno	Within NP10	467.39	466.78	470.50	470.47	468.95	468.63	Upper C24r	54.76	Norris et al. (1998d)	Gradstein et al. (2012)	
85	T *Subottina velascoensis*	Foram		489.32	489.23	491.12	490.98	490.22	490.11	–	55.07	Röhl et al. (2003)	Gradstein et al. (2012)	
86	T *Morozovella velascoensis*	Foram	B E3	502.53	502.53	504.15	504.15	503.34	503.34	No	55.20	Norris et al. (1998d)	Gradstein et al. (2012)	
87	T *Morozovella acuta*	Foram	Within E2	476.56	476.46	486.39	486.07	481.48	481.27	Mid C24r	55.39	Norris et al. (1998d)	Gradstein et al. (2012)	
88	B *Morozovella gracilis*	Foram	Within E2	502.48	502.48	502.58	502.58	502.53	502.53	No	55.39	Röhl et al. (2003)	Gradstein et al. (2012)	
89	B *Morozovella marginodentata*	Foram	Within E2	495.94	495.67	502.53	497.87	499.24	496.77	No	55.54	Norris et al. (1998d)	Gradstein et al. (2012)	
91	B *Tribrachiatus bramlettei*	Nanno	B NP10	510.82	510.82	518.55	518.46	514.69	514.64	No	55.86	Mita (2001)	Gradstein et al. (2012)	
92	B *Campylosphaera eodela*	Nanno	Within NP9	524.72	524.48	529.70	529.54	510.65	527.01	No	56.66	Norris et al. (1998d)	Gradstein et al. (2012)	
93	T *Globanomalina pseudomenardii*	Foram	B P5	524.72	524.48	534.38	534.08	529.55	529.28	Basal C24r	57.10	Norris et al. (1998d)	Gradstein et al. (2012)	
94	B *Morozovella subbotinae*	Foram	Within P4c	534.38	534.08	543.91	543.69	539.15	538.88	No	57.10	Norris et al. (1998d)	Gradstein et al. (2012)	As secondary marker for base P5
96	B *Discoaster multiradiatus*	Nanno	B NP9	528.17	528.06	529.65	529.49	524.26	528.78	C25n	57.21	Cramer et al. (2003)	Gradstein et al. (2012)	No indication of common vs rare
97	B *Discoaster nobilis*	Nanno	Within NP8	543.91	543.69	544.40	544.40	524.26	544.05	No	57.50	Norris et al. (1998d)	Gradstein et al. (2012)	
100	B *Acarinina soldadoensis*	Foram	B P4c	524.72	524.48	534.38	534.08	529.55	529.28	C25n/C25r transition	57.79	Norris et al. (1998d)	Gradstein et al. (2012)	

(*continued on next page*)

Table 3 (*continued*)

#	Event	Microfossil group	Zone	Min depth (mbsf)	Min depth (cmbsf)	Max depth (mbsf)	Max depth (cmbsf)	Average depth (mbsf)	Average depth (cmbsf)	Consistent with polarity?	Age (Ma, GTS2012)	Reference	GTS2012 calibration	Comments
103	X *Bekoma campechensis/Bekoma bidartensis*	Rad	B RP7	536.00	535.95	540.50	540.35	538.25	538.15	–	58.23	Sanfilippo and Blome (2001)	Norris et al. (2014a)	
104	B *Heliolithus riedelii*	Nanno	B NP8	543.91	543.69	544.40	544.40	524.26	544.05	Lower C25r	58.70	Norris et al. (1998d)	Gradstein et al. (2012)	
105	T *Heliolithus kleinpellii*	Nanno	Within NP7	534.38	534.08	543.91	543.69	524.26	538.89	Lower C25r	58.80	Janus Database	Gradstein et al. (2012)	Approximating B NP8
107	B *Discoaster mohleri*	Nanno	B NP7	543.91	543.69	544.40	544.40	524.26	544.05	No	58.97	Norris et al. (1998d)	Gradstein et al. (2012)	
108	B *Stylotrochus nitidus*	Rad	B RP6c	542.66	542.46	543.91	543.69	543.29	543.08	–	59.00	Sanfilippo and Blome (2001)	Norris et al. (2014a)	
110	B *Heliolithus kleinpellii*	Nanno	B NP6	555.48	555.48	556.16	556.16	555.82	555.82	No	59.54	Norris et al. (1998d)	Gradstein et al. (2012)	
111	B *Sphenolithus anarrhopus*	Nanno	Within NP5	555.48	555.48	556.16	556.16	555.82	555.82	No	59.68	Norris et al. (1998d)	Gradstein et al. (2012)	
112	B *Globanomalina pseudomenardii*	Foram	B P4a	582.30	582.10	592.15	591.78	587.23	586.94	No	60.73	Norris et al. (1998d)	Gradstein et al. (2012)	
113	B *Chiasmolithus consuetus*	Nanno	Within NP5	566.58	566.52	568.06	567.98	567.32	567.25	No	61.03	Norris et al. (1998d)	Gradstein et al. (2012)	Indicates mid C26r
115	B *Morozovella velascoensis*	Foram	Within P3a	582.30	582.10	592.15	591.78	587.23	586.94	Polarity unclear	61.33	Norris et al. (1998d)	Gradstein et al. (2012)	As secondary marker for base P3b
117	B *Fasciculithus tympaniformis*	Nanno	B NP5	566.58	566.52	568.06	567.98	567.32	567.25	No	61.51	Norris et al. (1998d)	Gradstein et al. (2012)	Indicates C26r
118	B *Sphenolithus primus*	Nanno	Within NP4	582.30	582.10	592.15	591.78	587.23	586.94	–	61.98	Janus Database	Gradstein et al. (2012)	Indicates lowermost C26r
119	B *Chiasmolithus bidens*	Nanno	Within NP4	592.20	591.78	601.60	601.48	596.90	596.63	–	62.07	Norris et al. (1998d)	Gradstein et al. (2012)	
121	B *Morozovella conicotruncata*	Foram	Within P3a	601.64	601.48	611.30	611.09	606.47	606.29	Lower C26r	62.22	Norris et al. (1998d)	Gradstein et al. (2012)	Indicates lowermost C26r
123	B *Morozovella angulata*	Foram	B P3a	592.15	591.78	601.64	601.48	596.90	596.63	Broadly consistent with C26r/C27n transition	62.29	Norris et al. (1998d)	Gradstein et al. (2012)	Indicates C26r/C27n transition
124	B *Morozovella praeangulata*	Foram	Within P2	611.30	611.09	620.09	620.09	615.70	615.59	Polarity unclear	62.46	Norris et al. (1998d)	Gradstein et al. (2012)	Indicates upper C27r
126	B *Praemurica uncinata*	Foram	B P2	631.20	631.20	634.78	634.78	632.99	632.99	Polarity unclear	62.60	Norris et al. (1998d)	Gradstein et al. (2012)	
127	B *Ellipsolithus macellus*	Nanno	B NP4	611.30	611.09	620.09	620.09	615.70	615.59	C27r	63.25	Janus Database	Gradstein et al. (2012)	Indicates C27r
129	B *Praemurica inconstans*	Foram	B P1c	642.47	641.59	643.95	643.95	643.21	642.77	Polarity unclear	63.90	Norris et al. (1998d)	Gradstein et al. (2012)	As secondary marker for base P1c
132	B *Chiasmolithus danicus*	Nanno	B NP3	642.47	641.59	643.95	643.95	643.21	642.77	C28r	64.81	Janus Database	Gradstein et al. (2012)	Indicates C28r

Table 4
Holes 1050A,C magnetostratigraphic tiepoints with two interpretations (Options 1–2, and Option 3) considered in the present work. Abbreviations: cmbsf – compacted meters below sea floor; B – base.

Reversal #	Magnetozone	Options 1 and 2		Option 3		Age (Ma, GTS2012)
		Ogg and Bardot (2001) (cmbsf)	± (m)	This study (cmbsf)	± (m)	
12	B C19n	7.72	3.52	7.72	3.52	41.39
14	B C19r	25.28	1.14	25.28	1.14	42.30
21	B C20n	61.91	0.28	61.91	0.28	43.43
27	B C20r	138.78	1.51	138.78	1.51	45.72
33	B C21n	–	–	152.40	0.79	47.35
45	B C22n	154.07	0.36	154.07	0.36	49.34
55	B C22r	166.48	0.53	183.01	0.35	50.63
63	B C23n	175.39	0.36	–	–	51.83
66	B C23r	183.01	0.35	–	–	52.62
68	B C24n.1n	188.85	0.17	–	–	53.07
70	B C24n.1r	189.83	0.80	–	–	53.20
76	B C24n.3n	198.73	0.35	198.73	0.35	53.98
95	B C24r	253.40	0.45	253.40	0.45	57.10
98	B C25n	257.43	0.24	257.43	0.24	57.66
106	B C25r	275.30	0.24	275.30	0.24	58.96
109	B C26n	279.31	0.29	279.31	0.29	59.24
122	B C26r	332.54	0.68	332.54	0.68	62.22
125	B C27n	344.95	1.54	344.95	1.54	62.52
128	B C27r	370.62	0.03	370.62	0.03	63.49
131	B C28n	387.43	0.64	387.43	0.64	64.67
133	B C28r	392.09	2.65	392.09	2.65	64.96
136	B C29n	395.50	0.76	395.50	0.76	65.69

separately.

2.4. Stratigraphic considerations

All ages reported in this paper are relative to GTS2012. Since most nannofossil data for Leg 171B holes were published using either NP or CP zonations (Martini, 1971; Okada and Bukry, 1980, respectively), we were unable to apply the recent zonation by Agnini et al. (2014), as no data on most zonal markers were available. Foraminiferal zones are according to Wade et al. (2011), and radiolarian zonations follow Sanfilippo and Nigrini (1998), Nigrini et al. (2006), and Norris et al. (2014a). In considering the evolutionary events (hereafter bioevents) discussed below, we follow the convention adopted in GTS2012. Thus, only two designations are used for a taxon stratigraphic range: "B" (base) and "T" (top). Sporadically, we also use "B acme" and "T acme", when referring to stratigraphic intervals with marked fluctuations in a taxon's abundance.

In order to review the stratigraphy of Holes 1050A,C and 1051A, we took great care to compile the available magneto- and biostratigraphic data (Figs. 3–4; Tables 2–5). The data compilation includes magnetic reversals, and foraminiferal, calcareous nannofossil, and radiolarian bioevents. For consistency, these are arranged according to depth for each Hole, and numbered sequentially from 1 to 138. For clarity, however, biostratigraphic markers (Tables 2–3) are tabulated separately from the reversals (Tables 4–5). Due to the large number of data points, we include oversized versions of the age-depth plots in the online Supplementary Materials (Supplementary Figs. S1, S2).

As some of the magnetic reversals identified at sites 1050 and 1051 are subject to divergent interpretations (for instance, Ogg and Bardot, 2001, versus Luciani et al., 2016, 2017, for Hole 1051A), calcareous microfossil biostratigraphic datums were checked against their published polarity patterns from GTS2012. For radiolarians, we followed Norris et al. (2014a) in that polarity patterns from Nigrini et al. (2006) and Kamikuri et al. (2012) were used for those events that fall within Zones RP8 through RP16. Earlier radiolarian datums usually lack a direct calibration to magnetostratigraphy (see discussion in Gradstein et al., 2012, p. 877). Regardless, numerical ages for radiolarian bioevents from Norris et al. (2014a) were used. In the age-depth plots in Figs. 3 and 4, we underline those events that are consistent with their published polarity patterns, and in the graphic correlation procedure described below we include only those biostratigraphic tiepoints that are reported from both study sites, and proved to be polarity-consistent. We employ the graphic correlation method (e.g., Shaw, 1964; Edwards, 1995; MacLeod and Sadler, 1995) in order to compare the magnetochron assignments, and check these against an independent stratigraphic proxy, i.e., diatom bioevents. As a final step in refining the stratigraphic framework for the study sites, we test the correlation by quantifying the alignment of trends in high-resolution weight percent biogenic opal (hereafter wt% $_{bio}SiO_2$) records from Holes 1050A,C and Hole 1051A, from Witkowski et al. (under review).

3. Stratigraphy

3.1. Holes 1050A,C

Magnetostratigraphy at Site 1050 is excellent, with tightly constrained reversals (Röhl et al., 2001), and there are few, usually narrow, overprinted intervals. Norris et al. (1998c) and Ogg and Bardot (2001) identified magnetozones C19n through C26r in Hole 1050A and C26r through C29r in Hole 1050C. Two hiati were identified in Norris et al. (1998c), at 152.83 cmbsf (hereafter termed **upper hiatus**) and at 192.93 cmbsf (hereafter **lower hiatus**) (Fig. 3).

A striking feature in the lithology of Hole 1050A is a silicified hardground at ~152.83 cmbsf, ~1.25 m above the base of a normal polarity interval (Fig. 8 in Norris et al., 1998c). Calcareous nannofossil biostratigraphy indicates a hiatus associated with the hardground, which truncates Subzone NP14a (Norris et al., 1998c). Consequently, Ogg and Bardot (2001) interpreted the normal polarity interval above the hardground as magnetozone C21n, and the narrow normal polarity interval below the hardground as the basal part of magnetozone C22n. Nannofossil and radiolarian data support this interpretation. B *D. sublodoensis* (tiepoint #43 in Fig. 3) supports the assignment to C22n (Gradstein et al., 2012) and is here interpreted to mark the onset of the hiatus, despite no indication of the number of rays in Norris et al. (1998c). The number of rays is an important feature, as the base of nannofossil Zone NP14 in GTS2012 is drawn on the first occurrence of 5-rayed *D. sublodoensis*. The radiolarian marker for B RP10 (Norris et al., 2014a), which indicates C21r/C22n transition, is broadly consistent with the timing of the hiatus (tiepoint #41 in Fig. 3). Constraining the termination of the hiatus is more challenging, however. B *R. inflata* (tiepoint #33 in Fig. 3) is inconsistent with the normal polarity documented by Ogg and Bardot (2001). In order to match the observed polarity pattern, we extend the duration of the hiatus to B C21n. If this interpretation is correct, the hardground at ~152.83 cmbsf represents at least a ~1.76 myr break in sedimentation straddling the EMET from 49.11 to at least 47.35 Ma (see discussion in Norris et al., 1998d) (Fig. 3).

Norris et al. (1998c) detected another hiatus at ~193.92 cmbsf (Fig. 3), but provided an ambiguous account. The shipboard nannofossil biostratigraphy constrained the hiatus as spanning lower to middle Zone NP12. Citing the apparent polarity pattern, however, the biomagnetostratigraphy section of the site report (Norris et al., 1998c), states that "this sedimentary break is not as pronounced as was presumed from the shipboard paleontologic interpretation". The putative discontinuity falls within a normal polarity interval, originally interpreted as magnetozone C24n (Norris et al., 1998c; Ogg and Bardot, 2001). We challenge this interpretation, for reasons discussed below.

The hiatus occurs ~4.8 m above the top of an extended reversed polarity interval (Fig. 3). Nannofossil and foraminiferal tiepoints (#77 - T *T. contortus*, #83 - B *T. contortus*, #84 - B *D. diastypus*, #88 - B *M. gracilis*, #89 - B *M. marginodentata*, #90 - B *P. wilcoxensis*, #94 - B *M. subbotinae* in Fig. 3) strongly suggest this reversed polarity interval

Table 5
Hole 1051A magnetostratigraphic tiepoints with three interpretations (Options 1–3) considered in the present work. Abbreviations: cmbsf – compacted meters below sea floor; B – base.

Reversal	Magnetozone	Age (Ma, GTS2012)	Option 1			Option 2			Option 3		
			Depth (cmbsf)	± (m)	Reference	Depth (cmbsf)	± (m)	Reference	This study (cmbsf)	± (m)	Reference
1	B C17n	38.33	6.62	–	Edgar et al. (2010)	6.62	–	Edgar et al. (2010)	6.62	–	Edgar et al. (2010)
2	B C17r	38.62	15.49	–	Edgar et al. (2010)	15.49	–	Edgar et al. (2010)	15.49	–	Edgar et al. (2010)
4	B C18n.1n	39.63	54.67	1.90	Edgar et al. (2010)	54.67	1.90	Edgar et al. (2010)	54.67	1.90	Edgar et al. (2010)
5	B C18n.1r	39.70	59.05	0.01	Edgar et al. (2010)	59.05	0.01	Edgar et al. (2010)	59.05	0.01	Edgar et al. (2010)
7	B C18n.2n	40.15	79.09	0.55	Edgar et al. (2010)	79.09	0.55	Edgar et al. (2010)	79.09	0.55	Edgar et al. (2010)
11	B C18r	41.15	128.27	0.01	Edgar et al. (2010)	128.27	0.01	Edgar et al. (2010)	128.27	0.01	Edgar et al. (2010)
12	B C19n	41.39	133.17	0.01	Edgar et al. (2010)	133.17	0.01	Edgar et al. (2010)	133.17	0.01	Edgar et al. (2010)
14	B C19r	42.30	165.89	0.35	Ogg and Bardot (2001)	165.89	0.35	Ogg and Bardot (2001)	165.89	0.35	Ogg and Bardot (2001)
21	B C20n	43.43	240.27	1.27	Ogg and Bardot (2001)	240.27	1.27	Ogg and Bardot (2001)	240.27	1.27	Ogg and Bardot (2001)
27	B C20r	45.72	348.55	2.05	Ogg and Bardot (2001)	348.55	2.05	Ogg and Bardot (2001)	348.55	2.05	Ogg and Bardot (2001)
33	B C21n	47.35	377.84	2.07	Ogg and Bardot (2001)	377.84	2.07	Ogg and Bardot (2001)	377.84	2.07	Ogg and Bardot (2001)
45	B C22n	49.34	394.72	1.78	Ogg and Bardot (2001)	394.72	1.78	Ogg and Bardot (2001)	394.72	1.78	Ogg and Bardot (2001)
55	B C22r	50.63	410.45	2.13	Ogg and Bardot (2001)	410.45	2.13	Ogg and Bardot (2001)	410.45	2.13	Ogg and Bardot (2001)
63	B C23n	51.83	420.17	1.24	Ogg and Bardot (2001)	394.72	1.78	Luciani et al. (2017)	–	–	Reinterpreted here
66	B C23r	52.62	430.00	1.54	Ogg and Bardot (2001)	410.45	2.13	Luciani et al. (2017)	–	–	Reinterpreted here
71	B C24n.2n	53.27	–	–	–	–	–	–	427.48	0.34	Reinterpreted here
74	B C24n.2r	53.42	–	–	–	–	–	–	430.82	0.34	Reinterpreted here
76	B C24n.3n	53.98	449.76	0.19	Ogg and Bardot (2001)	449.76	0.19	Ogg and Bardot (2001)	449.76	0.19	Ogg and Bardot (2001)
95	B C24r	57.10	524.30	0.42	Ogg and Bardot (2001)	524.30	0.42	Ogg and Bardot (2001)	524.30	0.42	Ogg and Bardot (2001)
98	B C25n	57.66	529.70	0.34	Ogg and Bardot (2001)	529.70	0.34	Ogg and Bardot (2001)	529.70	0.34	Ogg and Bardot (2001)
106	B C25r	58.96	549.00	0.15	Ogg and Bardot (2001)	549.00	0.15	Ogg and Bardot (2001)	549.00	0.15	Ogg and Bardot (2001)
109	B C26n	59.24	564.82	1.39	Ogg and Bardot (2001)	564.82	1.39	Ogg and Bardot (2001)	564.82	1.39	Ogg and Bardot (2001)
122	B C26r	62.22	620.75	0.87	Ogg and Bardot (2001)	620.75	0.87	Ogg and Bardot (2001)	601.93	0.54	Reinterpreted here
125	B C27n	62.52	642.47	0.71	Ogg and Bardot (2001)	642.47	0.71	Ogg and Bardot (2001)	–	–	
128	B C27r	63.49	–	–	–	–	–		620.75	0.87	Reinterpreted here
131	B C28n	64.67	–	–	–	–	–		642.47	0.71	Reinterpreted here

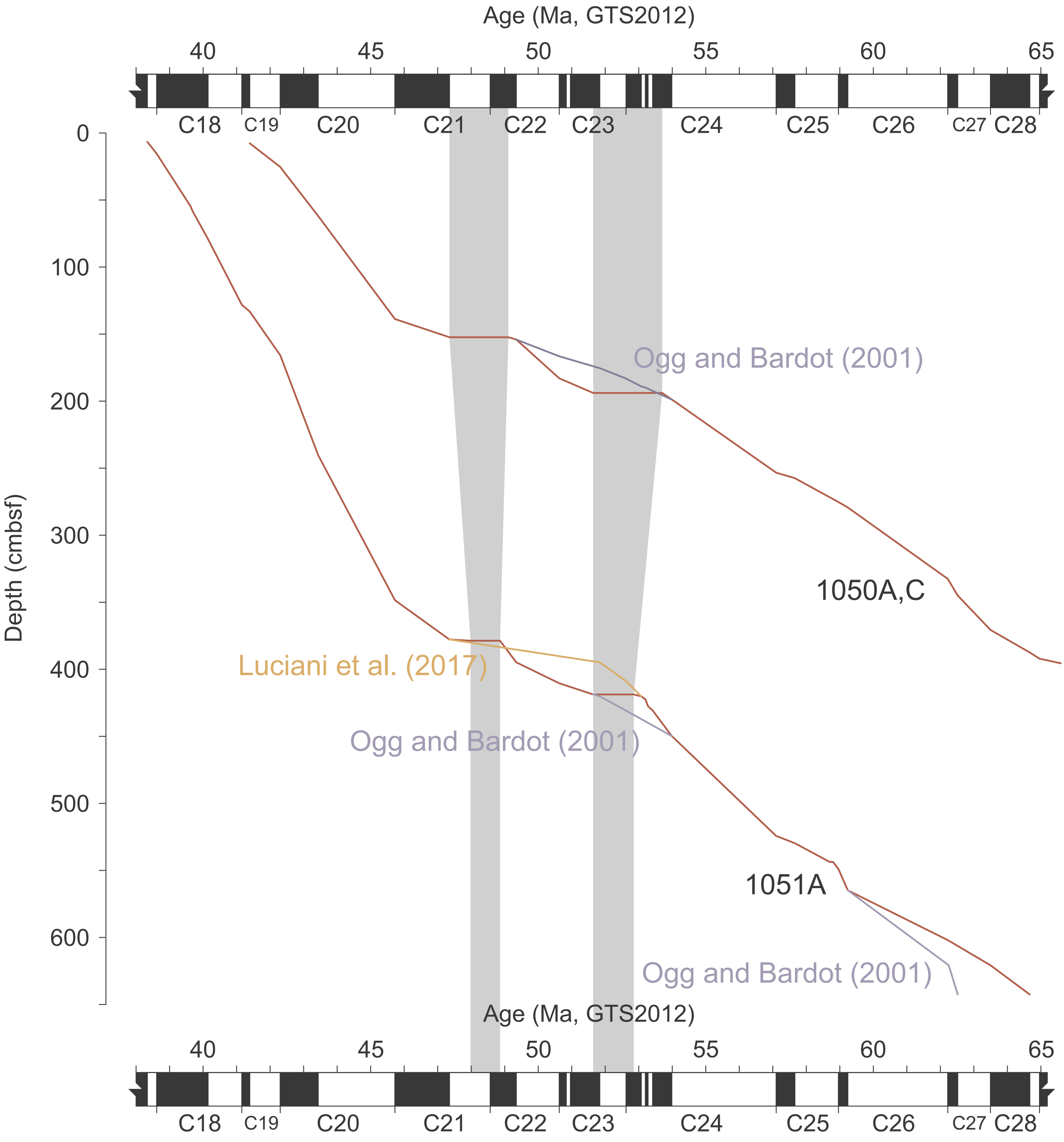

Fig. 5. Age-depth curve comparison for Holes 1050A,C and Hole 1051A, showing the broadly consistent timing of the major hiati juxtaposing magnetozones C21 on C22n, and C23n on C24n. Interpretations by Ogg and Bardot (2001) and Luciani et al. (2017) are shown for comparison.

represents magnetozone C24r. In this interpretation, the narrow normal polarity interval in the basal part of Core 1050A-22X (~208.8–207.3 cmbsf) represents a brief normal polarity subchron, or an overprint, consistent with the interpretation of Ogg and Bardot (2001). Calcareous nannofossil (#61 - B *C. crassus* and #75 - B *D. lodoensis* in Fig. 3) and foraminiferal events (#67 - T *M. marginodentata*, Fig. 3) that indicate the hiatus are consistent with its position within a normal polarity interval (Fig. 3). However, B *C. crassus* indicates lower subchron C23n.2n, whereas T *M. marginodentata* indicates subchron C24n.1n, and B *D. lodoensis* indicates C24n.3n. All this strongly suggests that the hiatus at ~193.92 cmbsf truncates the interval from the basal magnetozone C23n through the upper C24n.1n. If this interpretation is correct, the normal polarity intervals between ~181 and 166 cmbsf could represent overprints within magnetozone C22r. Resolving these issues is complicated due to the scarcity of biostratigraphic tiepoints, and the presence of several recovery gaps through this interval. In the Supplementary Fig. S1, we plot the Ogg and Bardot (2001) interpretation for comparison, which shows that the magnetostratigraphic age-depth curve proposed here displays a closer fit to the scatter of biostratigraphic data points (Fig. S1 in the online Supplementary materials).

We constrain the hiatus at ~193.92 cmbsf to span the interval from B *D. lodoensis* to B *C. crassus* (GTS2012 calibration from Norris et al., 2014b), i.e., equivalent to ~2 myrs from ~53.70 through 51.64 Ma. Foraminiferal data suggest that the onset of the hiatus could be interpreted at an earlier point in time (see tiepoints #78 - T *M. aequa*, #81 - B *M. formosa*, and #82 - B *M. lensiformis* in Fig. 3). These, however, are inconsistent with the observed polarity patterns. The termination of the hiatus is rather tightly constrained based on T *M. subbotinae* (#56 in Fig. 3), which is subjacent to a reversal that likely represents T C23n.

3.2. Hole 1051A

Except for several sampling gaps, Ogg and Bardot (2001) documented polarity patterns for the entire interval cored in Hole 1051A. This magnetostratigraphic framework was supplemented and further refined by Cramer et al. (2003) and Röhl et al. (2003) for the late Paleocene-early Eocene interval, and by Edgar et al. (2010) for the late middle Eocene interval. These refinements mostly regarded narrowing down the depth range of individual reversals (e.g., Röhl et al., 2003). In some cases, however, the chron assignments of Ogg and Bardot (2001) were changed (Edgar et al., 2010; Luciani et al., 2017). We also show a possible reinterpretation of the magnetostratigraphy for the basal part of Hole 1051A (consistent with the original view of Norris et al., 1998d), where polarity patterns are not straightforward due to numerous extensive overprinted and/or intermediate polarity intervals. All revisions to the magnetostratigraphy of Hole 1051A are plotted alongside the original solution of Ogg and Bardot (2001) for comparison in Fig. S2 in the online Supplementary materials.

Norris et al. (1998d) identified two discontinuities in Hole 1051A: one within nannofossil zone NP14 at 378.39 cmbsf (hereafter termed **upper hiatus**), and one within lower magnetozone C25r at 543.69 cmbsf (see also Röhl et al., 2003). This latter hiatus is not considered in detail in this work. Instead, we interpret another major hiatus at 418.68 cmbsf, not considered by Norris et al. (1998d), and hereafter refer to it as **lower hiatus**.

The upper hiatus occurs ~0.9 m above the top of a prominent silicified interval spanning 379.3 through 389.8 cmbsf (distinguished as lithological Unit II). This porcellanized foraminifer packstone unit (Figs. 7–8 in Norris et al., 1998d) was drilled through without coring, which hinders the interpretation of the stratigraphy in Hole 1051A. The hiatus is positioned approximately at a magnetic reversal in Hole 1051A. In Hole 1051B, however, it is reported to fall within the uppermost part of a reversed polarity interval, which Norris et al. (1998d) interpreted as the top part of magnetozone C21r. The hiatus was originally indicated by nannofossil markers occurring above and below the non-recovered interval (Norris et al., 1998d; Mita, 2001), and no reliable constraint on its duration was available. The strongest support for the upper hiatus in Hole 1051 comes from radiolarian datums (Sanfilippo and Blome, 2001) (Fig. 4). We constrain it using B *S. pachystylus* (tiepoint #42 in Fig. 4) and T *L. archea* (tiepoint #35 in Fig. 4), i.e., between ~48.86 and 47.98 Ma. The hiatus at 378.39 cmbsf in Hole 1051A is thus closely correlative with the upper hiatus in Hole 1050A (Fig. 5). This is consistent with Norris et al. (1998d), who observed that the EMET was truncated at all Leg 171B sites, but also that the record in Hole 1051A was more complete relative to other holes.

The shipboard interpretation assumed a complete record of magnetozones C22 through C24 (Norris et al., 1998d). Nannofossil and foraminiferal markers, however, strongly suggest a hiatus at 418.68 cmbsf, i.e., in the basal part of a normal polarity interval originally interpreted as C23n (Norris et al., 1998d; Ogg and Bardot, 2001). The hiatus is superjacent to a series of tightly spaced reversals (430.82 through 420.17 cmbsf; reversals #74, 71, 70 and 68 in Fig. 4). Foraminiferal and nannofossil markers (#69 - B *D. lodoensis* and #75 - T *M. lensiformis*, Fig. 4) suggest the lowest of these reversals represents B C24n.2r, and the highest of these - B C24n.1n. Further, nannofossil and foraminiferal markers recorded at the hiatus level indicate magnetozones C23r (#67 - T *M. marginodentata*, Fig. 4), and C23n.2n (#61 - B *C. crassus*, Fig. 4). The next higher reversal at 410.45 cmbsf can be recognized confidently as B C22r, as indicated by polarity-consistent radiolarian markers (Fig. 4). We therefore interpret the lower hiatus at 418.68 cmbsf in Hole 1051A to represent ~1.2 myr between B *D. lodoensis* and T *M. lensiformis*. If this interpretation is correct, the hiatus juxtaposes upper magnetozone C23n on lower C24n, consistent with our interpretation for Hole 1050A (Fig. 5). As in the case of Hole 1050A, our interpretation differs from Norris et al. (1998d), and Ogg and Bardot (2001) (see Fig. S2 for comparison). The revised magnetostratigraphic age-depth curve proposed here (Fig. 4), however, is more consistent with the scatter of all the compiled biostratigraphic tiepoints (Fig. S2).

Norris et al. (1998d) and Röhl et al. (2003) indicated a hiatus at 543.69 cmbsf within the lower part of magnetozone C25r (Fig. 4), where nannofossil evidence suggests the absence of zone NP7 (Norris et al., 1998d). Thus, the hiatus appears to span ~0.25 myrs, approximately equivalent to the missing zone duration. In contrast to the major hiati at 378.39 and 418.68 cmbsf, which have their equivalents in other Leg 171B holes (Fig. 5), Zone NP7 appears to be missing only at Site 1051, suggesting a local-scale erosional event or non-deposition.

The shipboard magnetostratigraphy for the basal part of Hole 1051A is unclear, with numerous uncertain polarity assignments (see Norris et al., 1998d versus Ogg and Bardot, 2001) (Fig. 4). In the Ogg and Bardot (2001) interpretation, Hole 1051A was terminated within magnetozone C27r. We propose an alternative interpretation for the basal part of Hole 1051A. Nannofossil and foraminiferal tiepoints (#129 - B *P. inconstans*, #132 - B *C. danicus*) suggest the normal polarity interval between ~620 and 630 cmbsf could represent magnetozone C28n. Drawing clear magnetozone boundaries is challenging due to the extensive intermediate polarity intervals (Fig. 4), and is further compounded by the presence of several recovery gaps, post-drilling core expansion, and a possible inverted core-catcher section in Core 1051A-70X (Table 3 in Ogg and Bardot, 2001). However, if the reversal recorded at ~620.75 cmbsf is identified as B C27r (mid-C27n in Ogg and Bardot, 2001), the resultant age-depth curve is considerably more consistent with the scatter of biostratigraphic tiepoints (Fig. 4) than the original interpretation of Ogg and Bardot (2001). The above also implies that nannofossil Zone NP3 is present in Hole 1051A in addition to the equivalent of Zone NP4 distinguished in Norris et al. (1998d).

The stratigraphic data from Holes 1050A,C and Hole 1051A reviewed above can be reduced to three scenarios (Tables 4–5), hereafter referred to as Options 1–3: (1) the original interpretation of Norris et al. (1998c, 1998d) and Ogg and Bardot (2001), with subsequent additions from Cramer et al. (2003), Röhl et al. (2003) and Edgar et al. (2010); (2) as in Option 1, but with a major reinterpretation proposed by Luciani et al. (2016, 2017), and (3) a revised interpretation assuming two extensive and broadly correlative hiati that juxtapose magnetozones C21n on C22n (upper hiatus) and C23n on C24n (lower hiatus) (Fig. 5).

In order to test which of these scenarios represents the best magnetostratigraphic solution for Sites 1050 and 1051, we employ the graphic correlation method of Shaw (1964) (e.g., Edwards, 1995; MacLeod and Sadler, 1995; Gradstein et al., 2012). In the graphic correlation procedure, we compare the depths of magnetic reversals that are recorded at both study sites, and compare these to biostratigraphic tiepoints that proved consistent with their published polarity patterns, and to an independent proxy that was not used for magnetozone identification, i.e., diatom bioevents documented in this study (Table 6). Thus, the relative distribution of diatom bioevents should be expected to support or disprove any of the scenarios considered here.

Table 6
Diatom bioevents documented in this study in Holes 1050A,C and 1051A.

#	Diatom bioevents	Holes 1050A,C				Hole 1051A			
		Min depth (cmbsf)	Max depth (cmbsf)	Average depth (cmbsf)	± (m)	Min depth (cmbsf)	Max depth (cmbsf)	Average depth (cmbsf)	± (m)
D1	T *Fenneria kanayae*	39.57	49.07	44.32	4.75	217.35	225.46	221.41	4.06
D2	B *Diplomenora cocconeiforma*	49.07	58.56	53.82	4.75	225.46	235.99	230.73	5.26
D3	B *Quadrocistella montana*	58.56	68.09	63.33	4.77	243.95	256.90	250.43	6.47
D4	T '*Hemiaulus* sp., asymmetric'	77.58	87.06	82.32	4.74	256.90	264.30	260.60	3.70
D5	B *Drepanotheca bivittata*	77.58	87.06	82.32	4.74	264.30	273.90	269.10	4.80
D6	B *Entogoniopsis foveatamorpha*	87.06	96.60	91.83	4.77	283.50	293.10	288.30	4.80
D7	T *Hemiaulus curvatulus* acme	115.80	125.40	120.60	4.80	312.30	322.00	317.15	4.85
D8	T *Craspedodiscus moelleri*	125.40	135.00	130.20	4.80	331.60	341.20	336.40	4.80
D9	B *Xanthiopyxis oblonga*	135.00	144.58	139.79	4.79	341.20	350.90	346.05	4.85
D10	B *Hemiaulus curvatulus*	135.00	144.58	139.79	4.79	341.20	350.90	346.05	4.85
D11	B *Hemiaulus mesolepta*	135.00	144.58	139.79	4.79	350.90	360.60	355.75	4.85
D12	B '*Hemiaulus* sp., asymmetric'	135.00	144.58	139.79	4.79	360.60	370.20	365.40	4.80
D13	B *Hemiaulus crenatus*, coarse	144.58	154.20	149.39	4.81	360.60	370.20	365.40	4.80
D14	B *Craspedodiscus moelleri* acme	144.58	154.20	149.39	4.81	360.60	370.20	365.40	4.80
D15	B *Fenneria kanayae*	144.58	154.20	149.39	4.81	370.20	379.80	375.00	4.80
D16	B *Fenneria brachiata*	144.58	154.20	149.39	4.81	370.20	379.80	375.00	4.80
D17	B *Rocella praenitida*	144.58	154.20	149.39	4.81	391.80	398.10	394.95	3.15
D18	T *Hemiaulus originalis*	144.58	154.20	149.39	4.81	391.80	398.10	394.95	3.15
D19	T *Rhizosolenia hebetata*	144.58	154.20	149.39	4.81	391.80	398.10	394.95	3.15
D20	T *Coscinodiscus mirabilis*	154.20	163.80	159.00	4.80	391.80	398.10	394.95	3.15
D21	B *Craspedodiscus moelleri*	163.80	173.18	168.49	4.69	398.05	409.59	403.82	5.77
D22	B *Coscinodiscus mirabilis*	190.39	199.98	195.19	4.79	428.80	438.40	433.60	4.80
D23	B *Radialiplicata clavigera*	190.39	199.98	195.19	4.79	438.40	448.00	443.20	4.80
D24	B *Quadrocistella rectanoguma*	190.39	199.98	195.19	4.79	438.40	448.00	443.20	4.80
D25	B *Distephanosira architecturalis*	–	–	–	–	438.40	448.00	443.20	4.80
D26	B *Hemiaulus originalis*	190.39	199.98	195.19	4.79	448.00	457.60	452.80	4.80
D27	T *Hemiaulus peripterus*	199.98	209.48	204.73	4.75	460.70	469.30	465.00	4.30
D28	T *Hemiaulus jordani*	209.48	220.64	215.06	5.58	469.30	477.50	473.40	4.10
D29	B *Pyrgupyxis gracilis*	220.64	227.37	224.01	3.37	477.50	488.50	483.00	5.50
D30	T *Hemiaulus jordani* acme	220.64	238.62	229.63	8.99	488.48	497.25	492.87	4.38
D31	B *Rhizosolenia hebetata*	227.37	238.62	233.00	5.63	488.48	497.25	492.87	4.38
D32	T *Medlinia fenestrata*	238.62	242.23	240.43	1.80	506.30	516.85	511.58	5.27
D33	T *Trochosira* cf. *T. spinosa*	242.23	248.20	245.22	2.99	516.85	524.83	520.84	3.99
D34	B *Hemiaulus jordani*	248.20	257.78	252.99	4.79	524.83	534.30	529.57	4.73
D35	T *Eunotogramma variabile*	257.78	267.50	262.64	4.86	524.83	534.30	529.57	4.73
D36	T *Pterotheca kittoniana*	257.78	267.50	262.64	4.86	524.83	534.30	529.57	4.73
D37	B *Cylindrospira simsiae*	257.78	267.50	262.64	4.86	534.30	543.90	539.10	4.80
D38	B *Fenneria nascens*	257.78	267.50	262.64	4.86	534.30	543.90	539.10	4.80
D39	T *Trinacria pileolus*	257.78	267.50	262.64	4.86	534.30	543.90	539.10	4.80
D40	B *Gombosia stomata*	267.50	276.29	271.90	4.40	534.30	543.90	539.10	4.80
D41	B *Hemiaulus incurvus*	267.50	276.29	271.90	4.40	543.90	553.50	548.70	4.80
D42	B *Hemiaulus inaequilaterus*	276.29	286.23	281.26	4.97	543.90	553.50	548.70	4.80
D43	B *Trochosira* cf. *T. spinosa* acme	276.29	286.23	281.26	4.97	556.60	563.10	559.85	3.25
D44	B *X. structuralis*	296.26	305.89	301.08	4.82	572.70	582.30	577.50	4.80
D45	T *P. evermanni*	296.26	305.89	301.08	4.82	572.70	582.30	577.50	4.80
D46	B *H. peripterus*	305.89	314.90	310.40	4.51	582.30	592.00	587.15	4.85
D47	B *T. praetenuis*	305.89	314.90	310.40	4.51	582.30	592.00	587.15	4.85
D48	T *Liradiscus* sp. 1 acme	314.90	328.07	321.49	6.58	592.00	601.70	596.85	4.85
D49	B *Proboscia ciesielskii*	336.13	339.20	337.67	1.54	601.70	611.28	606.49	4.79
S1	B *Macrora barbadensis*	87.06	96.60	91.83	4.77	273.90	283.50	278.70	4.80
E1	B *Ebriopsis crenulata*	144.58	154.20	149.39	4.81	360.60	370.20	365.40	4.80

3.3. *Diatom bioevents*

Below, we briefly discuss 49 diatom bioevents identified in this study (D1–D49; Table 6). Two additional siliceous microfossils considered here are the synurophyte scale *Macrora barbadensis* and the ebridian *Ebriopsis crenulata*. Despite the presence of these microfossils, our focus in the following discussion is on diatom bioevents.

D1: T *Fenneria kanayae* (Fenner) J. Witkowski

Discussion: *F. kanayae* (Pl. I, Fig. 28) is reported from onshore and deep-sea sites around the world (Witkowski, 2018). In both study sites, T *F. kanayae* is found within lower to middle C20n, with an age ranging from 42.89 to 43.15 Ma, which is younger than the age proposed by Witkowski (2018; 43.60 Ma based on the composite record from Site 1051). The placement within C20n documented here for T *F. kanayae* is broadly consistent with the calibration from the tropical Atlantic Site 1260 proposed by Witkowski (2018). It also suggests that even if T *F. kanayae* is diachronous between low- and mid-latitude sites, the difference in timing is smaller than originally considered by Witkowski (2018). For further discussion on *F. kanayae*, see D15.

D2: B *Diplomenora cocconeiforma* Blazé

Discussion: In LM, the diatom we identify as *D. cocconeiforma* (Pl. I, Fig. 20) is indistinguishable from the extant species. We are not aware of any records of fossil *Diplomenora* elsewhere than the BN area (Witkowski et al., 2014). Also, the extant *Diplomenora* is an epipsammic diatom (Round et al., 1990), which suggests that its occurrences in BN cores are valves transported from the neritic zone, as proposed by Witkowski et al. (2014) and further discussed in Witkowski et al. (under review). Future studies may therefore indicate that B *D. cocconeiforma* is not suitable for stratigraphic correlation. Regardless of this, at both study sites, B *D. cocconeiforma* falls within the basal part of a normal polarity interval (Figs. 6–8) interpreted as magnetozone C20n in all Options considered here.

D3: B *Quadrocistella montana* Suto

Discussion: *Quadrocistella* is a resting spore morphogenus that to date was reported from the Norwegian Sea, Western North Atlantic, and the North Pacific (Suto, 2006; Witkowski et al., 2014). The datums presented here (see also D24) show a considerably older age than in the study by Suto (2006; B *Quadrocistella* within early Oligocene). It remains to be verified whether *Quadrocistella* spp. documented here are conspecific with the Norwegian Sea and Pacific occurrences. At both study sites, B *Q. montana* (Pl. I, Fig. 21) falls within the uppermost part of magnetozone C20r (Figs. 6–8).

D4: T '*Hemiaulus* sp., asymmetric' Bukry

Discussion: This species is pending formal description. To date, it is

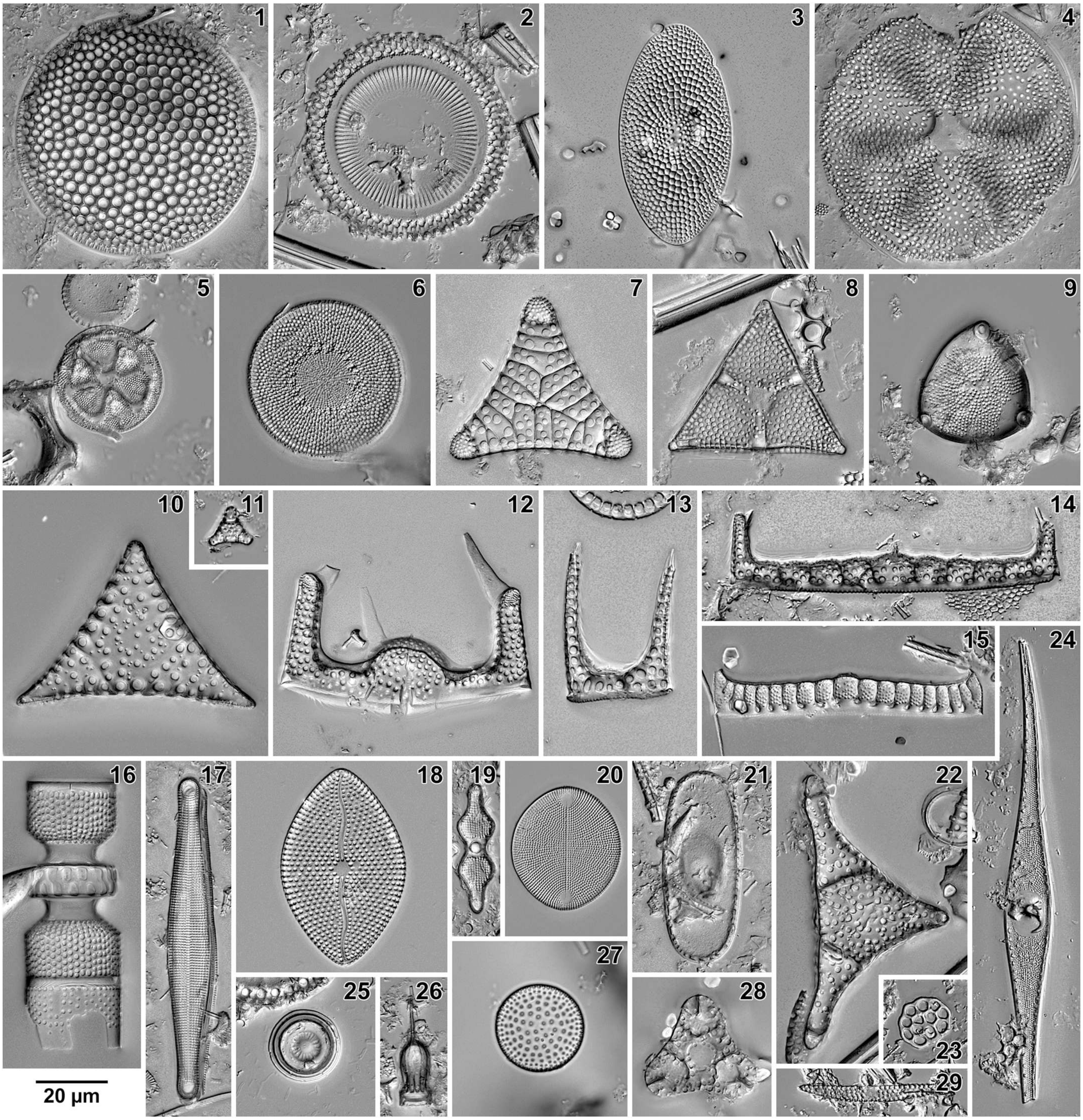

(caption on next page)

Plate I. Light micrographs of late early Eocene to middle Eocene diatoms from the Blake Nose, Western North Atlantic.
Fig. 1. *Coscinodiscus* sp. Sample ODP 171B-1053A-6H-1, 50–51 cm.
Fig. 2. *Paralia* sp. Sample ODP 171B-1051A-6H-1, 35–36 cm.
Fig. 3. *Craspedodiscus ellipticus* (Greville) Gombos. Sample ODP 171B-1050B-13X-3, 10–11 cm.
Fig. 4. *Actinoptychus hillabyanus* Brun. Sample ODP 171B-1053A-6H-1, 50–51 cm.
Fig. 5. *Actinoptychus intermedius* Schmidt. Sample ODP 171B-1051A-19X-4, 6–7 cm.
Fig. 6. *Distephanosira architecturalis* (Brun) Gleser, large morphotype. Sample ODP 171B-1050A-8H-1, 100–101 cm.
Fig. 7. *Entogoniopsis venosa* (Brightwell) Witkowski, Sims, Williams and Strelnikova. Sample ODP 171B-1050A-2H-2, 34–35 cm.
Fig. 8. *Entogoniopsis foveatamorpha* Witkowski, n.sp., holotype. Sample ODP 171B-1050A-14X-1, 100–101 cm.
Fig. 9. *Abas wittii* (Grunow) Ross and Sims. Sample ODP 171B-1051A-8H-3, 6–7 cm.
Fig. 10. *Euodiella* sp. Sample ODP 171B-1050A-3H-6, 33–34 cm.
Fig. 11. *Fenneria brachiata* (Brightwell) Witkowski. Sample ODP 171B-1051A-10H-1, 6–7 cm.
Fig. 12. *Hemiaulus immanis* (Boyer) Hendey and Sims. Sample ODP 171B-1050A-8H-1, 100–101 cm.
Fig. 13. *Hemiaulus mesolepta* (Grunow) Witkowski. Sample ODP 171B-1050A-3H-6, 33–34 cm.
Fig. 14. *Hemiaulus crenatus* Greville, coarsely areolated morphotype. Sample ODP 171B-1051A-13H-4, 6–7 cm.
Fig. 15. *Hemiaulus crenatus* Greville, finely areolated morphotype. Sample ODP 171B-1050B-13X-3, 10–11 cm.
Fig. 16. *Strangulonema barbadense* Greville. Sample ODP 171B-1050A-3H-6, 33–34 cm.
Fig. 17. *Rhaphoneis atlantica* Andrews. Sample ODP 171B-1051A-10H-1, 6–7 cm.
Fig. 18. *Mastogloia* sp. Sample ODP 171B-1050A-3H-6, 33–34 cm.
Fig. 19. *Plagiogramma* sp. Sample ODP 171B-1051A-18X-1, 6–7 cm.
Fig. 20. *Diplomenora cocconeiforma* Blazé. Sample ODP 171B-1050A-3H-6, 33–34 cm.
Fig. 21. *Quadrocistella montana* Suto. Sample ODP 171B-1050A-14X-1, 100–101 cm.
Fig. 22. '*Hemiaulus* sp., asymmetric' Bukry. Sample ODP 171B-1050B-13X-3, 10–11 cm.
Fig. 23. *Macrora barbadensis* (Deflandre) Bukry. Sample ODP 171B-1051A-10H-1, 6–7 cm.
Fig. 24. *Rutilaria areolata* Sheshukova-Poretzkaya. Sample ODP 171B-1050A-8H-1, 100–101 cm.
Fig. 25. *Pseudopodosira bella* Posnova and Gleser. Sample ODP 171B-1050A-8H-1, 100–101 cm.
Fig. 26. *Pterotheca aculeifera* Grunow. Sample ODP 171B-1050A-7H-1, 100–101 cm.
Fig. 27. *Rocella praenitida* (Fenner) Fenner. Sample ODP 171B-1051B-11H-5, 7–8 cm.
Fig. 28. *Fenneria kanayae* (Fenner) Witkowski. Sample ODP 171B-1050B-13X-3, 10–11 cm.
Fig. 29. Unidentified Cymatosiraceae. Sample ODP 171B-1051A-11H-2, 36–37 cm.

only known from the western North Atlantic (see Bukry, 1978). The consistent placement of T '*Hemiaulus* sp., asymmetric' (Pl. I., Fig. 22) within upper magnetozone C20r (Figs. 6–8), however, makes it a useful biostratigraphic marker, at least for the western North Atlantic. For further comments see D12.

D5: B *Drepanotheca bivittata* (Grunow and Pantocsek) Schrader

Discussion: This species has a global distribution (e.g., Schrader, 1969) and therefore should be considered a potential biostratigraphic marker. At both study sites, B *D. bivittata* falls within upper magnetozone C20r (Figs. 6–8).

D6: B *Entogoniopsis foveatamorpha* J. Witkowski, n. sp.

Discussion: *E. foveatamorpha* (Pl. I, Fig. 8) is proposed here and named for its morphological similarity to *E. foveata* (Greville) Witkowski, Sims, Strelnikova and Williams in Witkowski et al. (2015). At both study sites, B *E. foveatamorpha* occurs within the middle part of magnetozone C20r (Figs. 6–8).

D7: T acme *Hemiaulus curvatulus* Strelnikova

Discussion: *H. curvatulus* (Pl. II, Fig. 5) is a distinctive taxon that occurs in numerous mid- to high-latitude sites on the Russian Platform (e.g., Aleksandrova et al., 2012; Khokhlova and Oreshkina, 1999; Oreshkina and Oberhänsli, 2003). Its stratigraphic range, however, is poorly constrained, ranging from upper Cretaceous to the lower Eocene (Strelnikova, 1971, 1974; Aleksandrova et al., 2012). This is likely due to our poor understanding of the fossil hemiauloid diatoms. For instance, due to a variable valve curvature and assymetry, and disproportion in the relative size of the polar elevations (see Pl. III, Fig. 15 versus Pl. II, Fig. 5), *H. curvatulus* may be difficult to distinguish from *H. inaequilaterus* Gombos (1977) (see comments on *H. inaequilaterus* in Fenner, 1991, p. 137). A broad taxonomic study of early Paleogene hemiauloids is required to better delineate these important taxa. For further comments, see D10. At both study sites, T acme *H. curvatulus* falls within the lower part of magnetozone C20r (Figs. 6–8).

D8: T *Craspedodiscus moelleri* Schmidt

Discussion: *Craspedodiscus* is a distinctive genus of circular to elliptical diatoms with undulate valves, and is commonly reported from tropical deep-sea sites (Fenner, 1984) and mid- to high-latitude Eurasian Platform sites (Oreshkina and Aleksandrova, 2007, 2017). At both study sites, T *C. moelleri* (Pl. II, Fig. 1) falls within the basal part of magnetozone C20r (Figs. 6–8), immediately above B *Chiasmolithus gigas* (nannofossil tiepoint #25 defining B Subzone NP15b). For further comments, see D14 and D20.

D9: B *Xanthiopyxis oblonga* Ehrenberg

Discussion: *Xanthiopyxis* is a globally distributed resting spore morphogenus (Suto, 2004b). The stratigraphic range of *X. oblonga* documented here is broadly consistent with the observations of Suto (2004b). At both our study sites, B *X. oblonga* falls approximately at the C20r/C21n boundary (Figs. 6–8).

D10: B *Hemiaulus curvatulus* Strelnikova

Discussion: For further comments, see D7. At both study sites, B *H. curvatulus* falls approximately at the C20r/C21n boundary (Figs. 6–8).

D11: B *Hemiaulus mesolepta* (Grunow) J. Witkowski, stat. nov.

Discussion: *H. mesolepta* is readily distinguished from other Paleogene hemiauloid diatoms by its prominent central depression (Pl. I, Fig. 13). A compilation of geographic occurrences of this taxon in Witkowski et al. (2014) indicates that it could be used in stratigraphic correlation on a global scale. At both study sites, B *H. mesolepta* falls within the upper part of magnetozone C21n. Its exact distance from chron base, however, cannot be estimated due to the presence of the upper hiatus in both Holes 1050A and 1051A (Figs. 6–8).

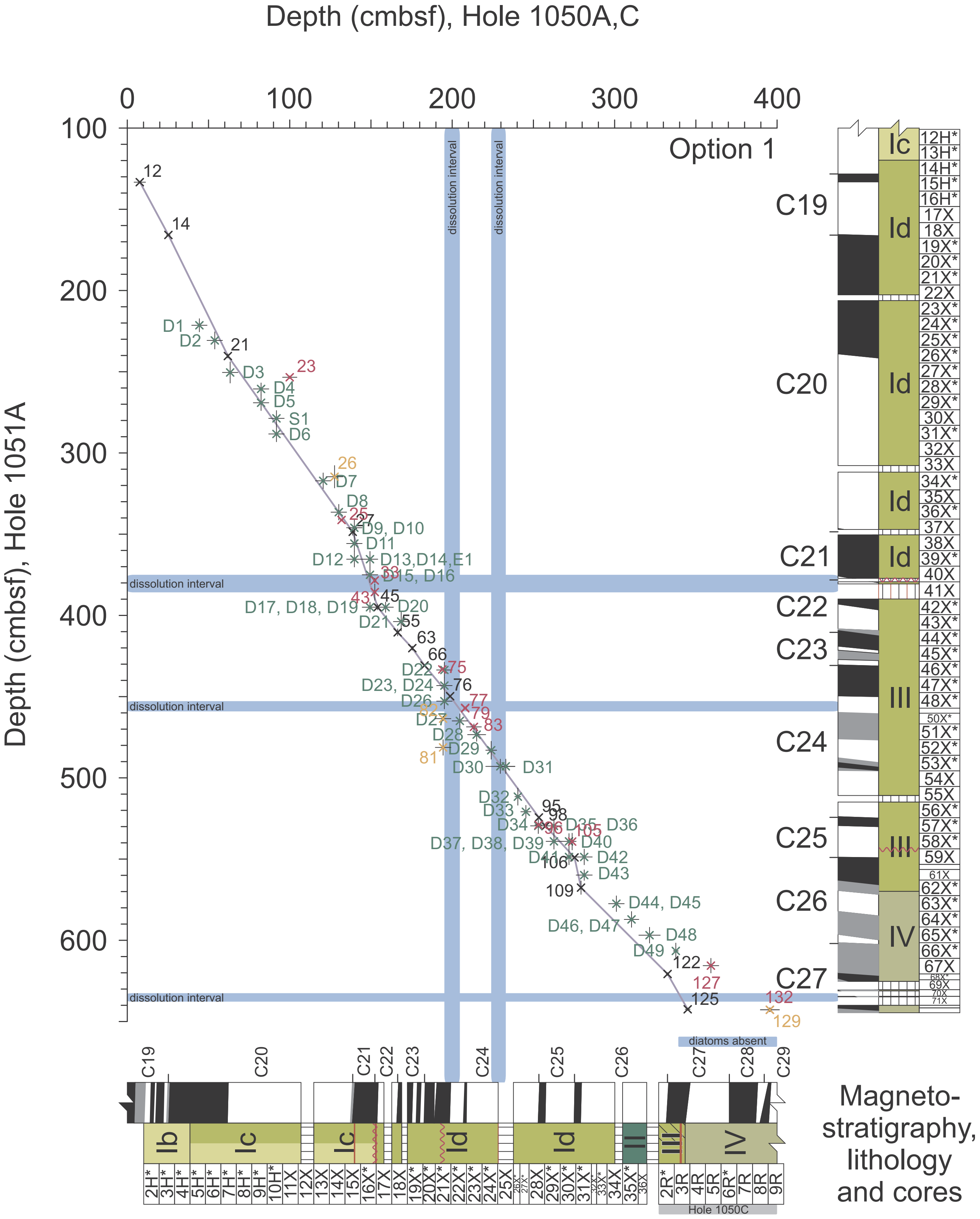

Fig. 6. Graphic correlation between Holes 1050A,C and Hole 1051A based on Option 1. Lithology and magneto- and biostratigraphic tiepoint color-coding follows Figs. 3 and 4. For clarity, only polarity-consistent biostratigraphic tiepoints are plotted (see Tables 2 and 4). Diatom dissolution intervals are highlighted in bright blue. For a list of diatom bioevents see Table 6. Cores indicated with an asterisk (*) have > 100% recovery due to post-drilling expansion. An oversized version of this plot is available as Fig. S3 in the online Supplementary materials. (For interpretation of the references to color in this figure legend, the reader is referred to the web version of this article.)

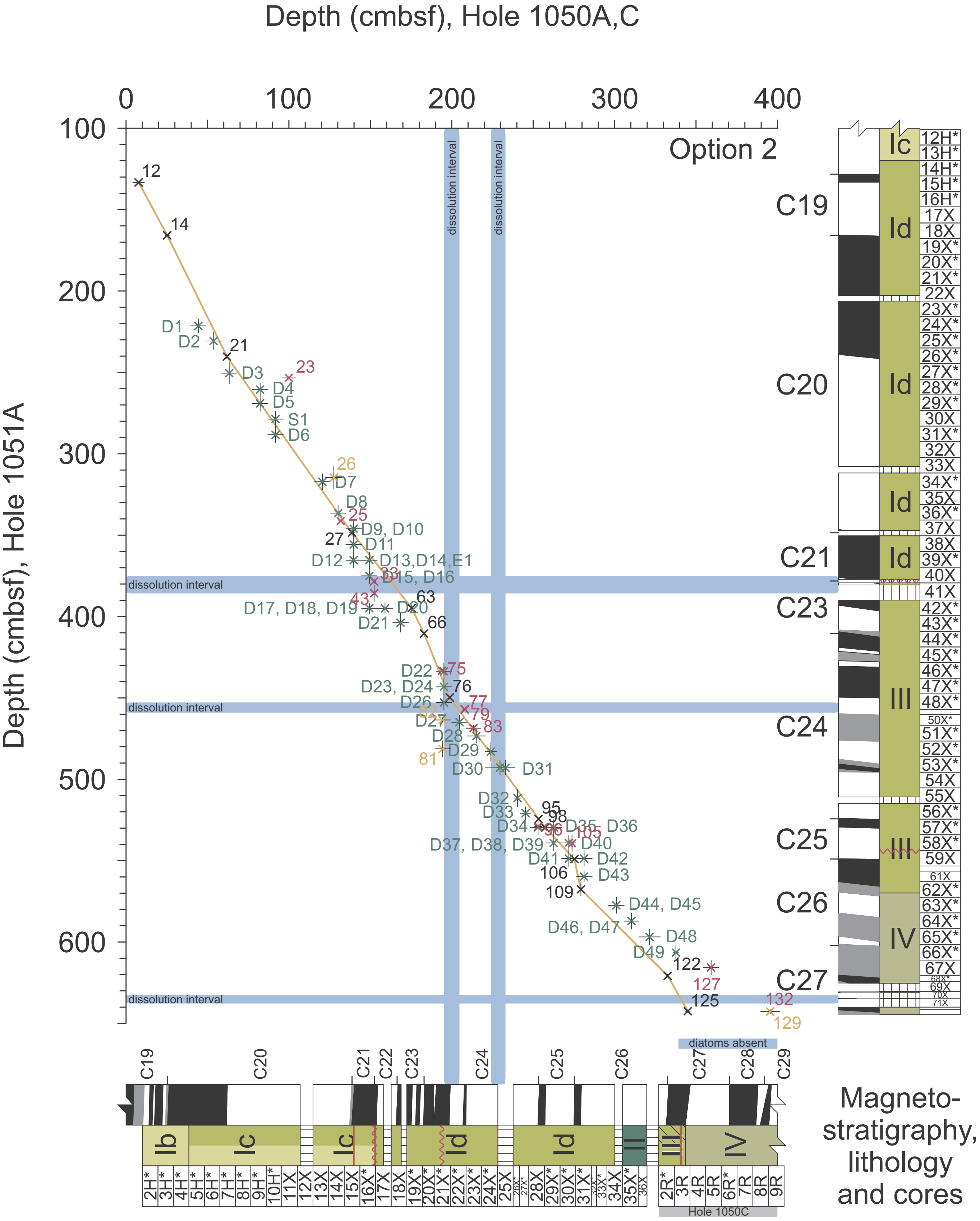

Fig. 7. Graphic correlation between Holes 1050A,C and Hole 1051A based on Option 2. Lithology and magneto- and biostratigraphic tiepoint color-coding follows Figs. 3 and 4. For clarity, only polarity-consistent biostratigraphic tiepoints are plotted (see Tables 2 and 4). Diatom dissolution intervals are highlighted in bright blue. For a list of diatom bioevents see Table 6. Cores indicated with an asterisk (*) have > 100% recovery due to post-drilling expansion. An oversized version of this plot is available as Fig. S4 in the online Supplementary Materials. (For interpretation of the references to color in this figure legend, the reader is referred to the web version of this article.)

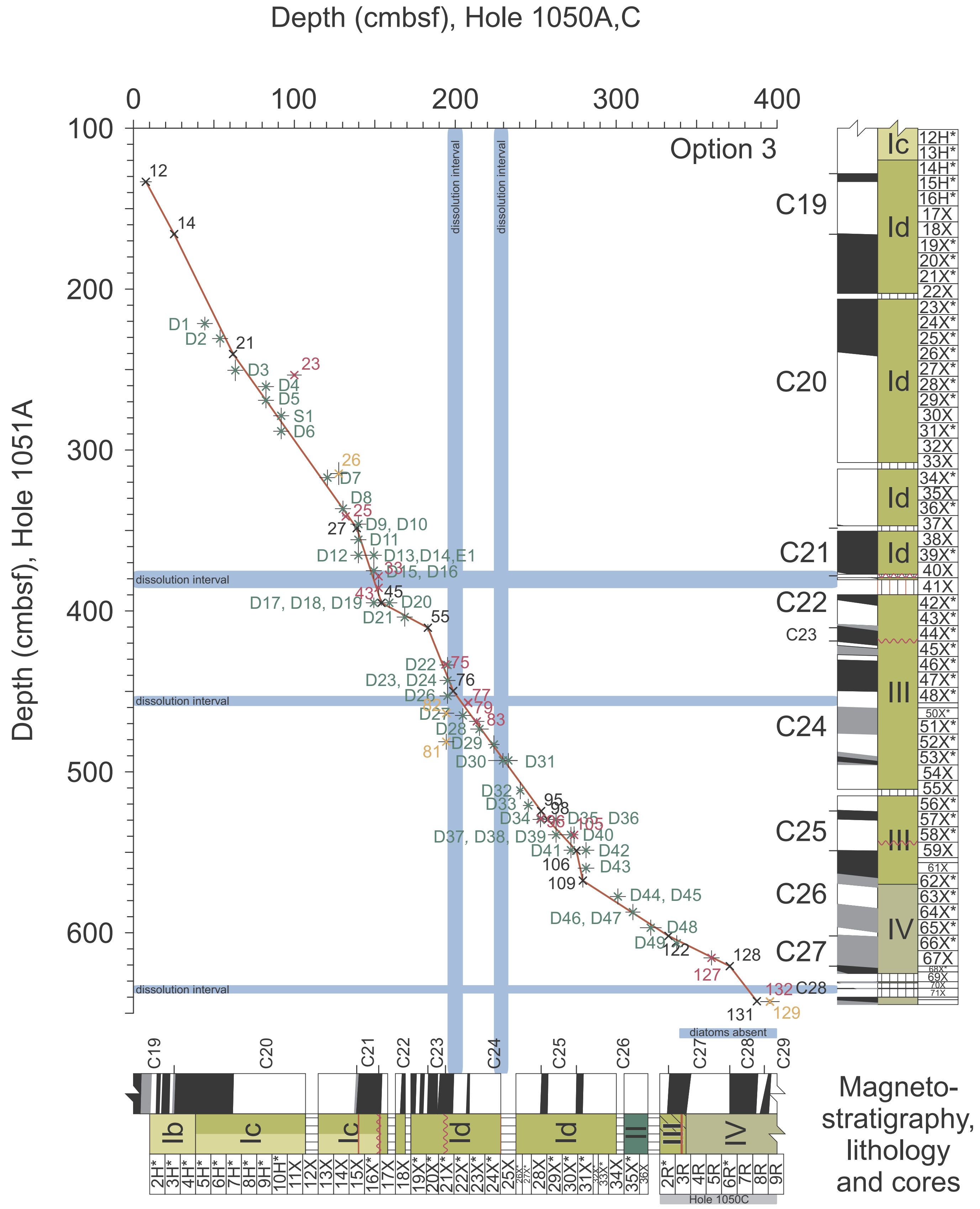

Fig. 8. Graphic correlation between Holes 1050A,C and Hole 1051A based on Option 3. Lithology and magneto- and biostratigraphic tiepoint color-coding follows Figs. 3 and 4. For clarity, only polarity-consistent biostratigraphic tiepoints are plotted (see Tables 2 and 4). Diatom dissolution intervals are highlighted in bright blue. For a list of diatom bioevents see Table 6. Cores indicated with an asterisk (*) have > 100% recovery due to post-drilling expansion. An oversized version of this plot is available as Fig. S5 in the online Supplementary Materials. (For interpretation of the references to color in this figure legend, the reader is referred to the web version of this article.)

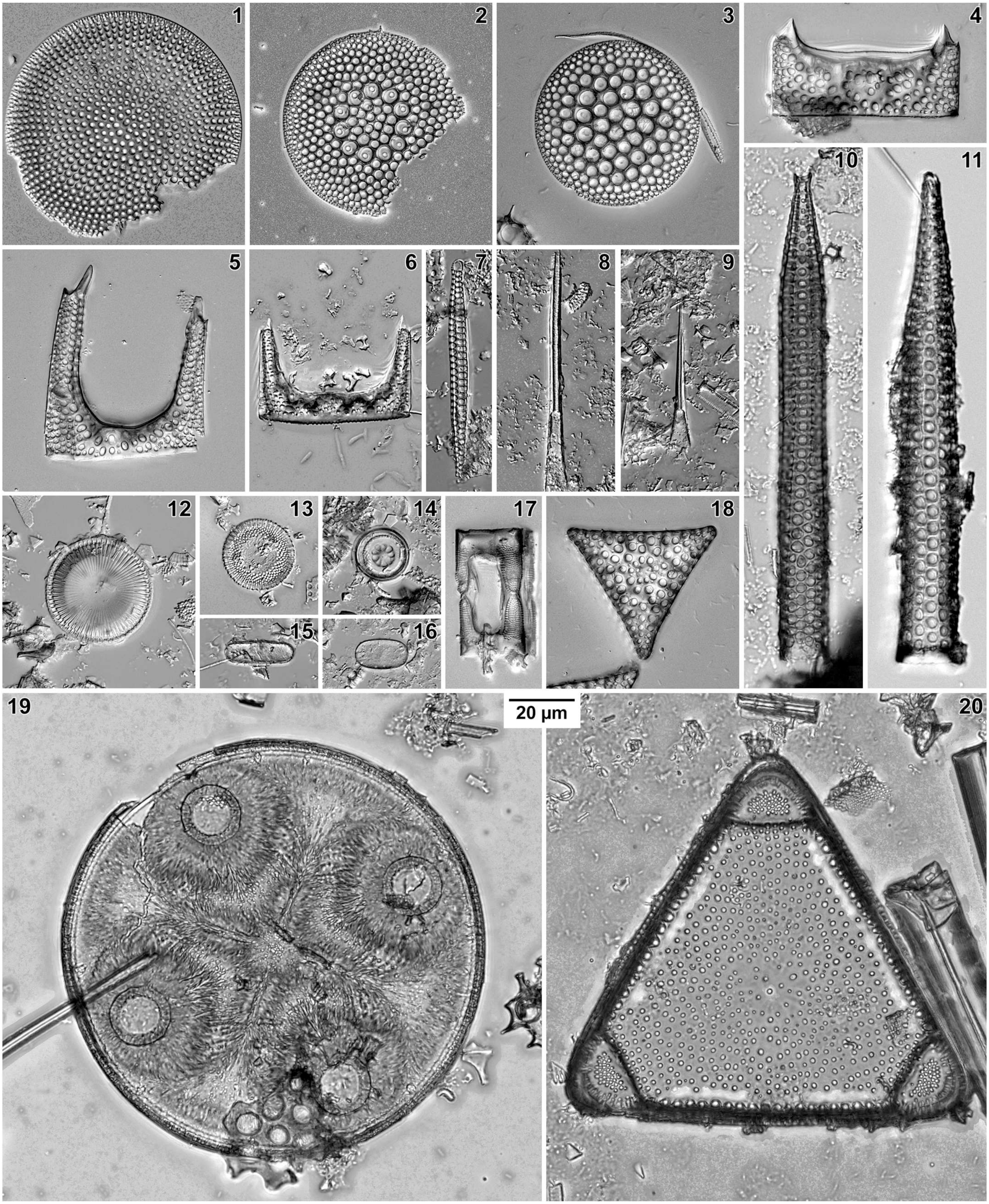

(caption on next page)

Plate II. Light micrographs of early Eocene diatoms from the Blake Nose, Western North Atlantic.
Fig. 1. *Craspedodiscus moelleri* Schmidt. Sample ODP 171B-1050A-8H-1, 100–101 cm.
Fig. 2. *Brightwellia hyperborea* Grunow. Sample ODP 171B-1051A-36X-1, 50–51 cm.
Fig. 3. *Coscinodiscus mirabilis* Jousé. Sample ODP 171B-1051A-50X-3, 50–51 cm.
Fig. 4. *Hemiaulus jordani* Witkowski n.sp. Sample ODP 171B-1051B-56X-1, 50–51 cm.
Fig. 5. *Hemiaulus curvatulus* Strelnikova. Sample ODP 171B-1051A-36X-1, 50–51 cm.
Fig. 6. *Hemiaulus originalis* Krotov. Sample ODP 171B-1050A-21X-1, 80–81 cm.
Fig. 7. *Grunowiella gemmata* (Grunow) Van Heurck. Sample ODP 171B-1050A-19X-1, 80–81 cm.
Figs. 8–9. *Rhizosolenia hebetata* Brightwell. Fig. 8. Sample ODP 171B-1050C-2R-3, 100–101 cm. Fig. 9. Sample ODP 171B-1050A-28X-1, 90–91 cm.
Figs. 10–11. *Pyrgupyxis gracilis* (Tempère and Forti) Hendey. Fig. 9. Sample ODP 171B-1051A-47X-1, 50–51 cm. Fig. 10. Sample ODP 171B-1051A-36X-1, 50–51 cm.
Fig. 12. *Radialiplicata clavigera* (Grunow) Gleser. Sample ODP 171B-1051A-43X-1, 4–6 cm.
Fig. 13. *Distephanosira architecturalis* (Brun) Gleser, small morphotype. Sample ODP 171B-1051A-42X-3, 50–51 cm.
Fig. 14. *Pseudopodosira bella* Posnova and Gleser. Sample ODP 171B-1051A-42X-1, 50–51 cm.
Figs. 15–16. *Quadrocistella rectagonuma* Suto. Fig. 15. Sample ODP 171B-1051A-10H-1, 6–7 cm. Fig. 16. Sample ODP 171B-1050A-9H-1, 100–101 cm.
Fig. 17. *Dextradonator jeremianus* Ross and Sims. Linked sibling valves in girdle view. Sample ODP 171B-1051A-36X-1, 50–51 cm.
Fig. 18. *Fenneria nascens* Bryłka and Witkowski n.sp., holotype. Sample ODP 171B-1051A-50X-3, 50–51 cm.
Fig. 19. *Auliscus johnsonianus* Greville. Sample ODP 171B-1051A-45X-4, 50–51 cm.
Fig. 20. *Triceratium exornatum* Greville. Sample ODP 171B-1051B-7H-6, 125–126 cm.

D12: B ‘*Hemiaulus* sp., asymmetric’ Bukry

Discussion: For more comments, see D4. In both study sites, B ‘*Hemiaulus* sp., asymmetric’ occurs within middle to upper part of the normal polarity interval superjacent to the upper hiatus, which represents magnetozone C21n. Its exact distance from chron base, however, cannot be estimated (Figs. 6–8).

D13: B *Hemiaulus crenatus* Greville - coarsely areolated morphotype

Discussion: *H. crenatus* is readily distinguished from other Eocene hemiauloids in that its valves are unusually long and divided by transverse costae into numerous ‘chambers’. We observed two morphotypes: one with fine areolation (Pl. I, Fig. 15), similar to the type illustration in Greville (1865), and a more abundant, coarsely areolated one (Pl. I, Fig. 14), which we propose as a stratigraphic marker. At both study sites, B *H. crenatus* (coarsely areolated morphotype) falls within the middle part of the normal polarity interval superjacent to the upper hiatus, which most likely represents magnetozone C21n (Figs. 6–8). Its exact distance from chron base, however, cannot be estimated.

D14: B acme *Craspedodiscus moelleri* Schmidt

Discussion: For more comments on *C. moelleri* see D8 and D21. We observe a considerable rise in abundance of *C. moelleri* at both study sites. B acme *C. moelleri* falls within the middle part of the normal polarity interval superjacent to the upper hiatus, which most likely represents magnetozone C21n (Figs. 6–8). Its exact distance from chron base, however, cannot be estimated.

D15: B *Fenneria kanayae* (Fenner) J. Witkowski

Discussion: At both study sites, B *F. kanayae* is observed within magnetozone C21n, immediately above the upper hiatus (Figs. 6–8). As in the case of events D11-D15, however, the exact distance from chron base cannot be estimated. Although the study by Witkowski (2018) was based on a different age model, and on the shipboard composite depth scale for Site 1051, the age established here for B *F. kanayae* (~47.19 Ma in Hole 1051A) is consistent with that proposed by Witkowski (2018). B *F. kanayae* is diachronous, with an age of ~45.96 Ma documented at the tropical Atlantic Site 1260 (Renaudie et al., 2010; Witkowski, 2018). For further comments, see D1.

D16: B *Fenneria brachiata* (Brightwell) J. Witkowski

Discussion: *F. brachiata* (Pl. I, Fig. 11) is a diminutive but globally distributed diatom. In low- and mid-latitude sites, its first occurrence is consistently coeval with *F. kanayae* (Barron et al., 2015), and thus also diachronous between low and mid-latitude sites (Witkowski, 2018). For further information, see discussion on D15.

D17: B *Rocella praenitida* (Fenner) Fenner

Discussion: A compilation of *R. praenitida* (Pl. I, Fig. 27) occurrences in Witkowski et al. (2014) shows that it is widely distributed and thus potentially enables a global stratigraphic correlation. In Hole 1050A, the error depth for B *R. praenitida* straddles the upper hiatus, but generally this event occurs within a normal polarity interval. In Hole 1051A B *R. praenitida* is observed in the lowermost portion of a normal polarity interval subjacent to the upper hiatus (Figs. 6–8). This is interpreted as magnetozone C22n according to Options 1 and 3, and magnetozone C23n according to Option 2 (Fig. 9).

D18: T *Hemiaulus originalis* Krotov

Discussion: This distinctive hemiauloid species (Pl. II, Fig. 6) was not reported from deep-sea sites to date. It is, however, one of the numerous taxa that occur at both BN and the mid-latitude Eurasian Platform sites (Krotov and Schibkova, 1959), suggesting a close correlation between these areas may be possible. For further comments, see D26. For comments on the polarity pattern, see D17 and D19.

D19: T *Rhizosolenia hebetata* Brightwell

Discussion: The valves of this species are extremely fragile and therefore *R. hebetata* (Pl. II, Figs. 8–9) is virtually never preserved intact. It is, however, reported from a number of deep-sea and onshore sites worldwide (e.g., Homann, 1991). For further comments, see D31. For discussion of polarity pattern, see D17–D18.

D20: T *Coscinodiscus mirabilis* Jousé

Discussion: Like *H. originalis*, *C. moelleri* and other taxa discussed here, *C. mirabilis* (Pl. II, Fig. 3) was first proposed from Eurasian Platform sites (Jousé, 1955) and - to our knowledge - not reported from deep-sea sites to date. A distinctive feature of the diatom we identify as *C. mirabilis* is the gradual decrease in areolae diameter toward the valve margin. This feature is also observed in *Coscinodiscus decrescens* Grunow, reported by Witkowski et al. (2014) from the MECO interval at Site 1051. In the present study, we observe no stratigraphic overlap between the large *C. mirabilis* and the considerably smaller *C. decrescens*. We do acknowledge, however, that a broad taxonomic study of coscinodiscoid diatoms is required. For further comments see D22. At both study sites, T *C. mirabilis* is found below the upper hiatus, within a reversed polarity interval. In Hole 1050A, this interval represents magnetozone C22r (Fig. 9). In Hole 1051A it may be interpreted as magnetozone C22r (Options 1 and 3) or C23r (Option 2) (Fig. 9).

D21: B *Craspedodiscus moelleri* Schmidt

Discussion: For more comments, see D8 and D14. In Hole 1050A, B *C. moelleri* occurs within a normal polarity interval that may be interpreted as magnetozone C23n (Options 1 and 2) or as an overprint within C22r (Option 3) (Fig. 9). In Hole 1051A, this event is noted within a reversed polarity interval that may be interpreted as lower magnetozone C23r (Option 2) or lower magnetozone C22r (Options 1 and 3) (Fig. 9).

D22: B *Coscinodiscus mirabilis* Jousé

Discussion: For more comments, see D20. At both study sites, B *C. mirabilis* is observed within magnetozone C24n.3n, at a similar level to nannofossil tiepoint #75 (B *D. lodoensis*, marker for B NP12) (Figs. 6–8).

D23: B *Radialiplicata clavigera* (Grunow) Gleser

Discussion: *Radialiplicata* Gleser is yet another taxon commonly reported from Eurasian Platform sites that also occurs at BN. At both study sites, B *R. clavigera* (Pl. II, Fig. 12) is found within magnetozone C24n.3n. In Hole 1050A, D25 is immediately subjacent to the lower hiatus and therefore no further constraint on distance from chron base is available. In Hole 1051A, however, D25 is placed in the lower part of

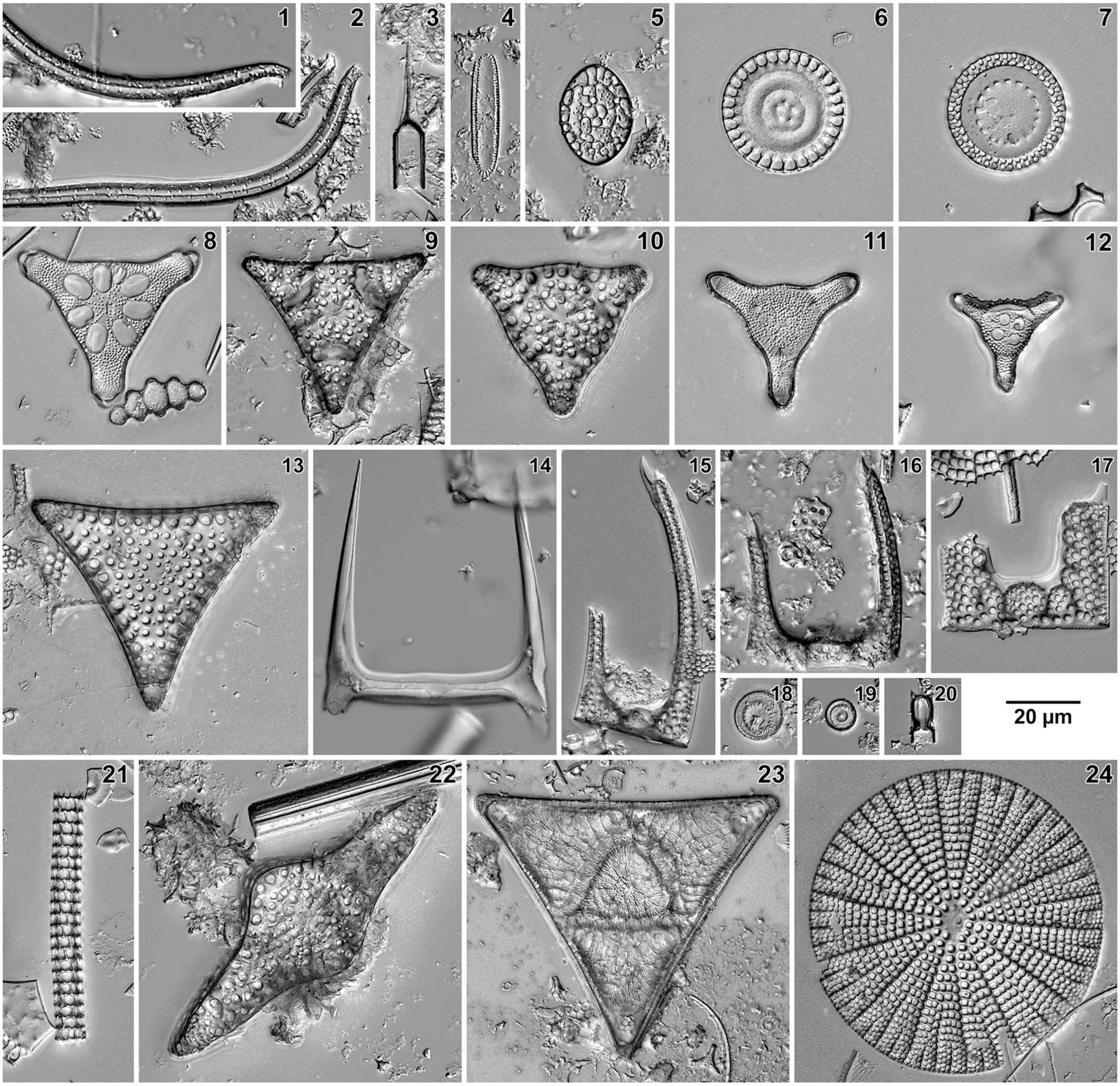

(caption on next page)

Plate III. Light micrographs of Paleocene and early Eocene diatoms from the Blake Nose, Western North Atlantic.
Figs. 1–2. *Proboscia ciesielskii* (Fenner) Witkowski, comb. nov. Sample ODP 171B-1051A-66X-1, 20–21 cm.
Fig. 3. *Pterotheca evermanni* Hanna. Sample ODP 171B-1050A-30X-1, 100–101 cm.
Fig. 4. *Xanthiopyxis structuralis* Fenner. Sample ODP 171B-1051A-60X-1, 20–21 cm.
Fig. 5. *Liradiscus* sp. 1. Sample ODP 171B-1050A-21X-1, 80–81 cm.
Fig. 6. *Anuloplicata concentrica* (Schmidt) Gleser. Sample ODP 171B-1050A-29X-1, 91–92 cm.
Fig. 7. *Paralia* sp. Sample ODP 171B-1050A-29X-1, 91–92 cm.
Fig. 8. *Gombosia stomata* Nikolaev and Harwood, with *Eunotogramma variabile* Grunow in the lower right corner. Sample ODP 171B-1050A-29X-1, 91–92 cm.
Fig. 9. *Medlinia fenestrata* (Witt) Sims. Sample ODP 171B-1050A-16X-1, 100–101 cm.
Fig. 10. *Medlinia simbirskiana* (Witt) Sims. Sample ODP 171B-1050A-29X-1, 91–92 cm.
Fig. 11. *Trinacria praetenuis* (Greville) Grunow. Sample ODP 171B-1050A-29X-1, 91–92 cm.
Fig. 12. *Gombosia brightwellioides* Nikolaev and Harwood. Sample ODP 171B-1050A-29X-1, 91–92 cm.
Fig. 13. *Trinacria pileolus* Ehrenberg. Sample ODP 171B-1050C-2R-5, 100–101 cm.
Fig. 14. *Hemiaulus peripterus* Fenner. Sample ODP 171B-1050A-27X-1, 70–71 cm.
Figs. 15–16. *Hemiaulus inaequilaterus* Gombos. Fig. 15. Sample ODP 171B-1050A-31X-1, 20–21 cm. Fig. 16. Sample ODP 171B-1051A-38X-1, 50–51 cm
Fig. 17. *Hemiaulus incurvus* Schibkova. Sample ODP 171B-1050A-29X-1, 91–92 cm.
Fig. 18. *Trochosira* cf. *T. spinosa* Kitton. Sample ODP 171B-1051A-59X-1, 20–21 cm.
Fig. 19. *Pseudopodosira bella* Posnova and Gleser. Sample ODP 171B-1050C-2R-5, 100–101 cm.
Fig. 20. *Pterotheca kittoniana* (Grunow in Van Heurck) Forti. Sample ODP 171B-1050C-2R-1, 100–101 cm.
Fig. 21. *Cylindrospira simsiae* Mitlehner. Sample ODP 171B-1050A-29X-1, 91–92 cm.
Fig. 22. *Anaulus weyprechtii* Grunow. Sample ODP 171B-1050A-32X-1, 100–101 cm.
Fig. 23. *Triceratium attenuatum* Greville. Sample ODP 171B-1050C-2R-5, 100–101 cm.
Fig. 24. *Arachnoidiscus clarus* Brown. Sample ODP 171B-1050C-2R-5, 100–101 cm.

C24n.3n (Figs. 6–8).

D24: B *Quadrocistella rectagonuma* Suto

Discussion: for more comments on the genus *Quadrocistella*, see D3. *Quadrocistella rectagonuma* (Pl. II, Figs. 15–16) is distinguished from other species encountered in BN cores by the lack of valve face undulations. At both study sites, B *Q. rectanoguma* is observed within magnetozone C24n.3n.

D25: B *Distephanosira architecturalis* (Brun) Gleser

Discussion: B *D. architecturalis* (Pl. II, Fig. 13) is observed immediately above the lower hiatus in Hole 1050A, and below the lower hiatus in Hole 1051A. This suggests that the actual base of this taxon range is truncated by the lower hiatus in Hole 1050A. However, we still include this event in the present study, as *Distephanosira* represents one of the most distinctive and widespread early Paleogene diatoms (see discussion in Witkowski et al., 2014). In contrast to previous studies, however, we note a considerable morphological variation within this genus: it is likely that *Distephanosira* includes several species (e.g., Pl. I, Fig. 6 vs Pl. II, Fig. 13) rather than the only taxon documented to date - *D. architecturalis* (Tables S4-S5 in the online Supplementary Materials). Further taxonomic studies are required to constrain the evolution and biostratigraphic utility of *Distephanosira* spp.

D26: B *Hemiaulus originalis* Krotov

Discussion: For further comments, see D18. In Hole 1050A, B *H. originalis* occurs within the basal part of magnetozone C24n.3n. In Hole 1051A, this event is observed within the uppermost part of magnetozone C24r (Figs. 6–8).

D27: T *Hemiaulus peripterus* Fenner

Discussion: *H. peripterus* is one of the most distinctive diatoms of

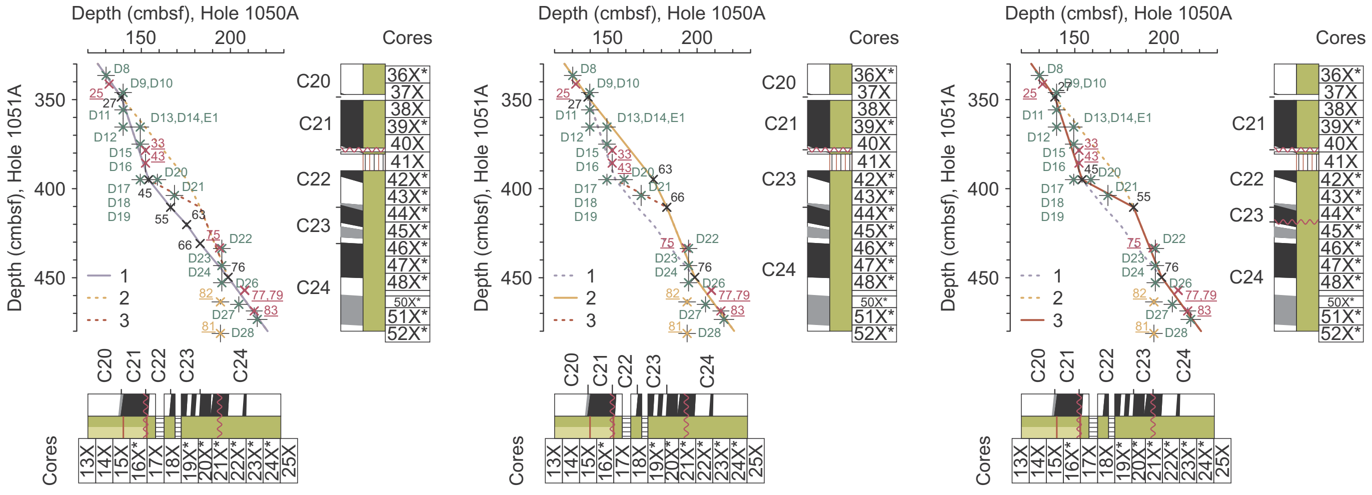

(A) Option 1 (B) Option 2 (C) Option 3

Fig. 9. Synopsis of Holes 1050A,C versus Hole 1051A graphic correlation on Options 1 (A), Option 2 (B) and Option 3 (C) over the intervals spanning the upper and lower hiatus. Note the differences in the alignment of the three lines of correlation (LOCs) against the polarity-consistent nannofossil and foraminiferal tiepoints and diatom bioevents. In each plot, the solid line represents the current option, and the dashed lines represent the remaining two options. Cores indicated with an asterisk (*) have > 100% recovery due to post-drilling expansion. Oversized version of this plot is available as Fig. S6 in the online Supplementary materials.

the early Paleogene (Pl. III, Fig. 14). It is also globally distributed in both deep-sea and onshore sites (e.g., Gombos Jr., 1977; Homann, 1991; Fenner, 1984; Fenner, 1994; Radionova and Khokhlova, 1994; Fourtanier, 1991; Fourtanier and Oscarson, 1994; Hollis et al., 2017). T *H. peripterus* occurs within a reversed polarity interval in Hole 1050A, and within an intermediate polarity interval in Hole 1051A (Figs. 6–8). For further comments on *H. peripterus* see D46.

D28: T *Hemiaulus jordani* J. Witkowski n. sp.

Discussion: Although it is a new species proposed here, *H. jordani* (Pl. II, Fig. 4) occurs only over a narrow stratigraphic interval. At present, its geographic distribution is unknown. Our preliminary observations, however, indicate that it may also be present in the mid- to high-latitude Eurasian Platform sites (e.g., Gleser and Sheshukova-Poretzkaja, 1967). We propose the base (D34) and top of this taxon range, as well as fluctuations in abundance (D30), as markers to constrain the hole-to-hole correlation. T *H. jordani* occurs within upper middle part of a thick reversed polarity interval interpreted as C24r at both study sites (Figs. 6–8).

D29: B *Pyrgupyxis gracilis* (Tempère and Forti) Hendey

Discussion: *Pyrgupyxis* Hendey, often referred to as *Pyxilla* Greville, is one of the most distinctive and widespread marine diatoms of the Paleogene period (e.g., Krotov and Schibkova, 1959; Gombos Jr., 1977, 1987; Fourtanier, 1991); in this study, we observe B *P. gracilis* (Pl. II, Figs. 10–11) to occur within an expanded reversed polarity interval in Holes 1050A and 1051A. The age of B *P. gracilis* established here is ~55.4 Ma, i.e., ~1.4 Ma older than the calibration of Barron et al. (2015), suggesting a considerable diachroneity between the Indian and western North Atlantic oceans.

D30: T acme *Hemiaulus jordani* J. Witkowski n. sp.

Discussion: For more comments, see D28 and D34. We note that T acme *H. jordani*, which falls within the middle part of a thick reversed polarity interval interpreted as magnetozone C24r (Figs. 6–8), is especially useful for correlation between the two sites.

D31: B *Rhizosolenia hebetata* Brigthwell

Discussion: At both study sites, B *R. hebetata* occurs in the middle part of a thick reversed polarity interval interpreted as magnetozone C24r (Figs. 6–8). For more comments, see D19.

D32: T *Medlinia fenestrata* (Witt) Sims

Discussion: *Medlinia* is a genus of heavily silicified, mostly tripolar diatoms (Sims, 1998). In this study, *Medlinia* spp. were often observed even within diatom dissolution horizons. Such heavy silicification and resistance to dissolution facilitates reworking, and therefore the stratigraphic range of some species (e.g., *M. abyssorum*) is likely extended artificially. T *M. fenestrata* (Pl. III, Fig. 9) is observed consistently within the middle part of magnetozone C24r at both study sites (Figs. 6–8). Given the broad distribution of *M. fenestrata* in Eurasian Platform onshore sites, it potentially represents a useful stratigraphic marker.

D33: T *Trochosira* cf. *T. spinosa* Kitton

Discussion: *Trochosira* is widespread in Cretaceous and early Paleogene deep-sea and onshore sites (e.g., Sims, 1988), and thus T *Trochosira* cf. *T. spinosa* (Pl. III, Fig. 18) potentially represents a useful stratigraphic marker. Due to its small size, however, *Trochosira* is often overlooked in studies based on sieved residues. It is a poorly understood genus in need of further taxonomic study.

D34: B *Hemiaulus jordani* J. Witkowski

Discussion: For further comments, see D28 and D30. Whereas T acme *H. jordani* is clearly marked in the range charts, we found constraining the base of the acme problematic. The likely reason for this is that the record in Hole 1051A is considerably expanded relative to that from Holes 1050A,C. We therefore propose B *H. jordani* rather than B acme *H. jordani* as a biostratigraphic marker. At both study sites, B *H. jordani* is positioned close to B *D. multiradiatus* (nannofossil tiepoint #96, Figs. 6–8).

D35: T *Eunotogramma variabile* Grunow

Discussion: *E. variabile* (Pl. III, Fig. 8) is another taxon that is often reported from onshore early Paleogene sites (e.g., Khokhlova and Oreshkina, 1999). Oreshkina and Aleksandrova (2017) reported *E. variabile* as present in “Beds with *Grunowiella gemmata*”, approximately correlative to the transition between magnetozones C26 and C25. This is broadly consistent with the range of *E. variabile* documented here (Figs. 6–8), and is yet another indication that diatoms are suitable for correlation between North Atlantic and Eurasian Platform mid-latitude sites.

D36: T *Pterotheca kittoniana* (Grunow) Forti

Discussion: *Pterotheca kittoniana* (Pl. III, Fig. 20) is a distinctive and globally distributed resting spore taxon ranging from the Late Cretaceous to the early Paleocene, often found as intact frustules connected in doublets (e.g., Jousé, 1951). Thus, *P. kittoniana* potentially represents another useful stratigraphic marker for the early Paleogene siliceous microfossil-bearing successions. In Hole 1050A, T *P. kittoniana* falls within the upper part of magnetozone C25r. In Hole 1051A, we observe this event at approximately C25n/C25r transition (Figs. 6–8). Because of the minor hiatus lower within C25r, distance from chron base cannot be estimated for Hole 1051A.

D37: B *Cylindrospira simsiae* Mitlehner

Discussion: *Cylindrospira* is an unusual diatom with cylindrical frustules that are strongly elongated along the pervalvar axis, and thus it can easily be confused with radiolarian tests. *C. simsiae* (Pl. III, Fig. 21) was originally reported from the Fur Fm diatomite (Mitlehner, 1995), straddling the Paleocene-Eocene boundary. It is also known, however, to occur in the mid- to high-latitude Eurasian Platform sites (Khokhlova and Oreshkina, 1999; Oreshkina and Oberhänsli, 2003; Oreshkina and Aleksandrova, 2007, 2017). In the Eurasian Platform sites, however, the stratigraphic range of *C. simsiae* appears considerably longer than observed here. Further work is required to better constrain the stratigraphic range of *C. simsiae* in deep-sea sites; it is also important to verify whether *Cylindrospira* occurring in deep-sea and onshore sites are conspecific. We observe B *C. simsiae* within mid- to upper magnetozone C25r (Figs. 6–8). Because of the minor hiatus lower within C25r, distance from chron base cannot be estimated for Hole 1051A.

D38: B *Fenneria nascens* Bryłka and J. Witkowski, n. sp.

Discussion: This species (Pl. II, Fig. 18) appears similar to valves reported as *Trinacria deciusi* Hanna from Southern Ocean cores by Fenner (1991), and superficially similar valves have been reported from Eurasian Platform sites by Strelnikova and Nikitina (2018). Should these prove conspecific, B *Fenneria nascens* is likely to become a biostratigraphic marker suitable for regional- or even global-scale correlation. For discussion of polarity patterns, see D37.

D39: T *Trinacria pileolus* Ehrenberg

Discussion: As in the case of *H. incurvus*, *E. variabile* and other taxa, *T. pileolus* is commonly reported from onshore sites on the Eurasian Platform (e.g., Strelnikova and Nikitina, 2018). To facilitate a possible correlation between the BN cores and the Eurasian Platform sites, we use T *T. pileolus* as a tiepoint to constrain the hole to hole correlation. For discussion of polarity patterns, see D37.

D40: B *Gombosia stomata* Nikolaev and Harwood

Discussion: To date, *G. stomata* (Pl. III, Fig. 8) was only reported from the BN cores (Nikolaev and Harwood, 2002). Because of its distinctive valve morphology, we found *G. stomata* an excellent marker for hole to hole correlation. At present, however, its stratigraphic utility outside the BN region is unknown. At both study sites, it occurs immediately above T *H. kleinpelii* (nannofossil tiepoint #105; Figs. 6–8) in the lower- to mid- magnetozone C25r. Because of the hiatus eliminating nannofossil Zone NP7 within C25r, distance from chron base cannot be estimated for Hole 1051A.

D41: B *Hemiaulus incurvus* Schibkova

Discussion: *Hemiaulus incurvus* (Pl. III, Fig. 17) is a distinctive diatom reported from Paleocene sediments of the Eurasian Platform (e.g., Krotov and Schibkova, 1959; Oreshkina and Oberhänsli, 2003), and from Indian Ocean (Mukhina, 1976; Fourtanier, 1991) and Southern Ocean sites (Gombos Jr., 1977, 1984; Hollis et al., 2017; Renaudie et al., 2018). B *H. incurvus* is also used as a zonal marker for the base of *Hemiaulus incurvus* Zone of Fourtanier (1991) (Fig. 2G, I). In the Indian Ocean Hole 752A, however, B *H. incurvus* occurs ~1.8 to 1.6 myrs earlier, at ~60.5 Ma (Barron et al., 2015), which suggests this event may be diachronous. In this study, we observe B *H. incurvus* in the basal part of magnetozone C25r (Hole 1050A), or at the C25r/C26n transition (Hole 1051A). Because of the hiatus eliminating nannofossil Zone NP7 within C25r, distance from chron base cannot be estimated for Hole 1051A (Figs. 6–8).

D42: B *Hemiaulus inaequilaterus* Gombos

Discussion: This species (Pl. III, Fig. 15) was first identified in the Falkland Plateau region by Gombos (1977), but was since reported from many deep-sea (Gombos, 1984; Fenner, 1991) and onshore sites (e.g., Oreshkina and Oberhänsli, 2003). Fenner (1991) commented on the broad range of morphological variation observed in *H. inaequilaterus* that potentially hinders its application in biostratigraphy. We do observe that *H. inaequilaterus* may sometimes be difficult to distinguish from *H. curvatulus* Strelnikova (Pl. II, Fig. 5; see comments in the Taxonomic List in the online Supplementary Materials). The ranges of both taxa will need to be further constrained in future studies. B *H. inaequilaterus* is observed close to the C26n/C26r transition in Hole 1050A, and at the C25r/C26n transition in Hole 1051A (Figs. 6–8).

D43: B acme *Trochosira* cf. *T. spinosa* Kitton

Discussion: *Trochosira* cf. *T. spinosa* (Pl. III, Fig. 18) forms a distinct acme in the basal part of Hole 1050A (uppermost magnetozone C26r) and in the lower part of Hole 1051A (lower magnetozone C26n) (Figs. 6–8). For more comments, see D33.

D44: B *Xanthiopyxis structuralis* Fenner

Discussion: *X. structuralis* (Pl. III, Fig. 4) was originally proposed from middle Eocene South Atlantic cores by Fenner (1977), and subsequently reported from the Paleocene intervals of South Atlantic and Indian Ocean cores (Fenner, 1991). Its occurrence in the western North Atlantic strongly suggests that this species is broadly distributed in the lower Paleogene and therefore it should be examined closely in future studies. In this study, it is observed consistently within upper magnetozone C26r (Figs. 6–8).

D45: T *Pterotheca evermanni* Hanna

Discussion: Renaudie et al. (2018) reported numerous Cretaceous diatom taxa surviving into the Paleocene on a global scale. We corroborate this observation, but note that for some taxa (e.g., *Cortinocornus rossicus* (Pantocsek) Gleser) it is challenging to distinguish between reworking and survivorship. The occurrences of *P. evermanni* (Pl. III, Fig. 3) are continuous in both study holes and therefore T *P. evermanni* is preferred to other survivor taxa as a tiepoint to constrain the hole-to-hole correlation. *Pterotheca evermanni* is a broadly distributed resting spore and has high potential as a biostratigraphic marker on a global scale. In this study, T *P. evermanni* is observed consistently within upper magnetozone C26r (Figs. 6–8).

D46: B *Hemiaulus peripterus* Fenner

Discussion: For further comments, see D27. B *Hemiaulus peripterus* refers to a morphotype that has linear valves. Strongly curved specimens are common in the basal part of Hole 1051A. The presumably correlative interval of Hole 1050C, however, lacks diatom preservation, and therefore we refrain from using the curved morphotype for hole-to-hole correlation. B *H. peripterus* occurs within a reversed polarity interval in Hole 1050A, and within an intermediate polarity interval in Hole 1051A (Figs. 6–8). Both these levels are interpreted as within mid-C26r.

D47: B *Trinacria praetenuis* (Greville) Grunow

Discussion: *Trinacria praetenuis* (Pl. III, Fig. 11) appears to be a short-lived taxon. Little comparative data is available on its geographic and stratigraphic distribution and thus future studies may prove it to be unsuitable for stratigraphic correlation. In this study, B *T. praetenuis* is consistently observed within mid- magnetozone C26r (Figs. 6–8).

D48: T acme *Liradiscus* sp. 1

Discussion: This undescribed species of the resting spore morphogenus *Liradiscus* Greville (see Suto, 2004a, 2007) is common in the basal parts of both study holes (Pl. III, Fig. 5). The base of this taxon range most likely occurs below the base of the biosiliceous interval in Hole 1050C. For this reason, we use T acme *Liradiscus* sp. 1, an event that can be identified confidently in both study holes within lower magnetozone C26r.

D49: B *Proboscia ciesielskii* (Fenner) J. Witkowski, comb. nov.

Discussion: This species (Pl. III, Figs. 1–2) was originally proposed by Fenner (1991) from Paleocene South Atlantic cores, and considered a fragment of a polar elevation of a hemiauloid diatom. Its occurrence in Holes 698A, 524A, 700B and 702B is temporally consistent with the present study sites, suggesting B *Proboscia ciesielskii* could be successfully used for age control on a basin scale. Although this event can be only tentatively identified in the basal part of the biosiliceous interval in Hole 1050C, it occurs precisely on the LOC for Option 3, i.e., within magnetozone C27.

Additional evolutionary events identified in the present study:

S1: B *Macrora barbadensis* (Deflandre) Bukry

Discussion: *M. barbadensis* (Pl. I, Fig. 23) most likely represents a synurophyte scale. It is commonly found in unsieved samples prepared for siliceous microfossil examination (e.g., Gleser and Jousé, 1974; Bukry, 1977; Witkowski et al., 2014) and thus represents a useful biostratigraphic marker that could potentially be used for correlation on a global scale. At both study sites this event occurs in the upper part of magnetozone C20r (Figs. 6–8).

E1: B *Ebriopsis crenulata* Hovasse

Discussion: *E. crenulata* is an ebridian (see Pl. II, Fig. 6 in Witkowski et al., 2014), but like *Macrora barbadensis*, it is frequently found in unsieved residues used for diatom assemblage examination. In both study sites, B *E. crenulata* occurs within the middle part of the normal polarity interval superjacent to the upper hiatus, which most likely represents magnetozone C21n (Figs. 6–8). Its exact distance from chron base, however, cannot be estimated.

3.4. Diatom-based correlation between Sites 1050 and 1051

In order to select the most plausible LOC, we tested all three age control Options against nannofossil and foraminiferal bioevents that occur in polarity intervals consistent with GTS2012, and against diatom bioevents discussed above and listed in Table 6. In Leg 171B sites, diatom bioevents have an important advantage over calcareous microfossils in that they were not used for magnetozone labelling during the shipboard and post-cruise studies. Thus, diatom events can be considered an independent proxy, and should be expected to give an unbiased perspective on the stratigraphy of Holes 1050A,C and 1051A.

In both study holes, diatom bioevents are sparse in the middle Eocene from the C20r/C20n transition upward (Figs. 6–8). This, however, is consistent with the observations by Barron et al. (2015), who indicate a broad low in the number of first occurrences among siliceous phytoplankton between upper magnetozone C20 and mid-C18. Downhole from the top of magnetozone C20r, however, we record 49 diatom bioevents, testifying to higher speciation and extinction rates through the Paleocene and early Eocene. With regard to polarity-consistent biostratigraphic tiepoints, 14 such bioevents (including 10 nannofossil and 4 foraminiferal datums) were found to occur at both study sites. Whereas some of these (e.g., foraminiferal tiepoints #81 - B *M. formosa* and #82 - B *M. lensiformis*) plot away from all three LOCs, others (especially nannofossil tiepoints #33 - B *R. inflata*, 43 - B *D. sublodoensis* and 75 - B *D. lodoensis*) appear to have a high significance for testing age control Options 1–3 (Fig. 9). Few GPTS calibrations are available for Paleogene diatoms (see Fourtanier, 1991; Barron et al., 2015; Witkowski, 2018). All these studies focus on establishing numerical ages rather than polarity patterns for diatom bioevents. Further, Barron et al. (2015) consider only low-latitude Eocene diatom zonal markers (including those proposed in Fourtanier, 1991), most of which are absent in the BN cores (see discussion in Witkowski, 2018). For these reasons, we do not include diatom bioevents other than those documented herein.

Diatom events are in good agreement with all three LOCs in the interval spanning magnetozones C19r through C20r/C21n transition, i.e., 0–~140 cmbsf in Hole 1050A, and 100–~350 cmbsf in Hole 1051A (Figs. 6–8). Nannofossil and foraminiferal tiepoints recorded in these intervals (#23 - T *Ch. gigas* and #26 - B *T. possagnoensis*) plot away from all three of the LOCs considered here (Figs. 6–8).

Options 1, 2 and 3 show substantial differences over the interval ~140–200 cmbsf in Hole 1050A and ~350–450 cmbsf in Hole 1051A, and are therefore discussed separately in more detail. Diatom bioevents D21 (B *Craspedodiscus moelleri*) and D22 (B *Coscinodiscus mirabilis*) plot away from Option 1 (Figs. 6, 9A), which assumes no break in sedimentation between magnetozones C22r through C24r. Option 1 is in agreement with polarity-consistent nannofossil tiepoints #33 and 43 (B *R. inflata* and B *D. sublodoensis*, respectively), but not consistent with #75 (B *D. lodoensis*) (Fig. 9A). Further, in the graphic correlation there are virtually no biostratigraphic data to support Ogg and Bardot's (2001) interpretation of the reversals #55 (B C22r), #63 (B C23n) and #66 (B C23r) (Fig. 9A).

Diatom bioevents D12 (B '*Hemiaulus* sp., asymmetric'), D15 (B *Fenneria kanayae*), D16 (B *Fenneria brachiata*), D17 (B *Rocella praenitida*), D18 (T *Hemiaulus originalis*), D19 (T *Rhizosolenia hebetata*), and D20 (T *Coscinodiscus mirabilis*) plot away from the LOC for Option 2 (Figs. 7, 9B), which assumes that at Site 1051 the entire magnetozone C22 is truncated by the upper hiatus (Luciani et al., 2017). Option 2 is also inconsistent with nannofossil tiepoints #33 and 43 (B *R. inflata* and B *D. sublodoensis*, respectively). As in the case of Option 1 above, the placement of the reversals #63 (B C23n) and #66 (B C23r) is not supported by any biostratigraphic tiepoints in the graphic correlation (Fig. 9B).

Diatom bioevents and polarity-consistent nannofossil tiepoints are in good agreement with Option 3 (Figs. 8, 9C), which assumes the presence of two major hiati at both sites, i.e., an upper hiatus that juxtaposes magnetozone C21n on C22n, and a lower hiatus that juxtaposes magnetozone C23n on C24n. Whereas two hiati were recognized in Hole 1050A (Norris et al., 1998c) from the start, the lower hiatus was not considered to date for Hole 1051A (e.g., Sanfilippo and Blome, 2001).

LOCs for Options 1 and 2 do not differ in the basal parts of the study sites, i.e., below B C24n. Diatom events, however, do not support Options 1 and 2 below B C26n, i.e., 279.31 cmbsf in Hole 1050A and below 564.82 cmbsf in Hole A (Figs. 6–7). Instead, diatom events are consistent with Option 3. Unfortunately, siliceous microfossils are not preserved in the basal portion of Hole 1050C, and therefore the graphic correlation method cannot be applied to diatom bioevents recorded in the bottom part of Hole 1051A. However, nannofossil tiepoints #127 (B *E. macellus*) and #132 (B *C. danicus*) as well as foraminiferal tiepoint #129 (B *P. inconstans*) (Fig. 8) are in good agreement with the slope of the Option 3 LOC indicated by diatom datums from higher levels at both study sites.

Overall, the three possible lines of correlation (LOCs) outlined above as Options 1–3 are consistent for the upper parts of both holes, but differ substantially for both the middle and bottom intervals. The distribution of diatom bioevents and polarity-consistent nannofossil and foraminiferal datums lends strong support to the LOC for Option 3 (Figs. 8, 9C), assuming the presence of two major hiati at both study sites. This also indicates that Hole 1051A terminated in sediments laid down during Magnetochron C28.

3.5. Testing the correlation

In order to gain quantitative insight on the improvements to the stratigraphy of Holes 1050A,C and 1051A proposed here, we used the high-resolution spectrophotometric wt% $_{\text{bio}}\text{SiO}_2$ records from Witkowski et al. (under review). $_{\text{Bio}}\text{SiO}_2$ concentrations are considered a proxy for surface water productivity (e.g., Piela et al., 2012). Given the close proximity of Sites 1050 and 1051, our assumption is that surface-water productivity should display similar trends at both sites. The $_{\text{bio}}\text{SiO}_2$ records were smoothed using a 15-point moving average, and subsampled at 0.25 myr increments. The alignment between the study sites was tested by a linear regression performed for age control Options 1, 2 and 3.

The strength of the correlation varies considerably between the options considered here. Option 1 (Fig. 10A) shows the largest scatter of regression points, and the correlation is weak at $r^2 = 0.6941$. Further, a considerable mismatch can be seen between the smoothed trends in $_{\text{bio}}\text{SiO}_2$ records, especially in the oldest part of the record, between ~60 and 65 Ma. When rescaled to Option 2, the $_{\text{bio}}\text{SiO}_2$ records retain the mismatch through the interval between ~60 and 65 Ma. However, the records also lack good alignment between ~50 and 55 Ma (Fig. 10B). The correlation ($r^2 = 0.7190$) is stronger than for Option 1, but a considerable scatter can still be seen in the regression plot (Fig. 10B).

We observe the strongest correlation ($r^2 = 0.9569$) for Option 3 (Fig. 10C). Visually, the trends in smoothed $_{\text{bio}}\text{SiO}_2$ records are well-aligned and remarkably consistent. We therefore conclude that the

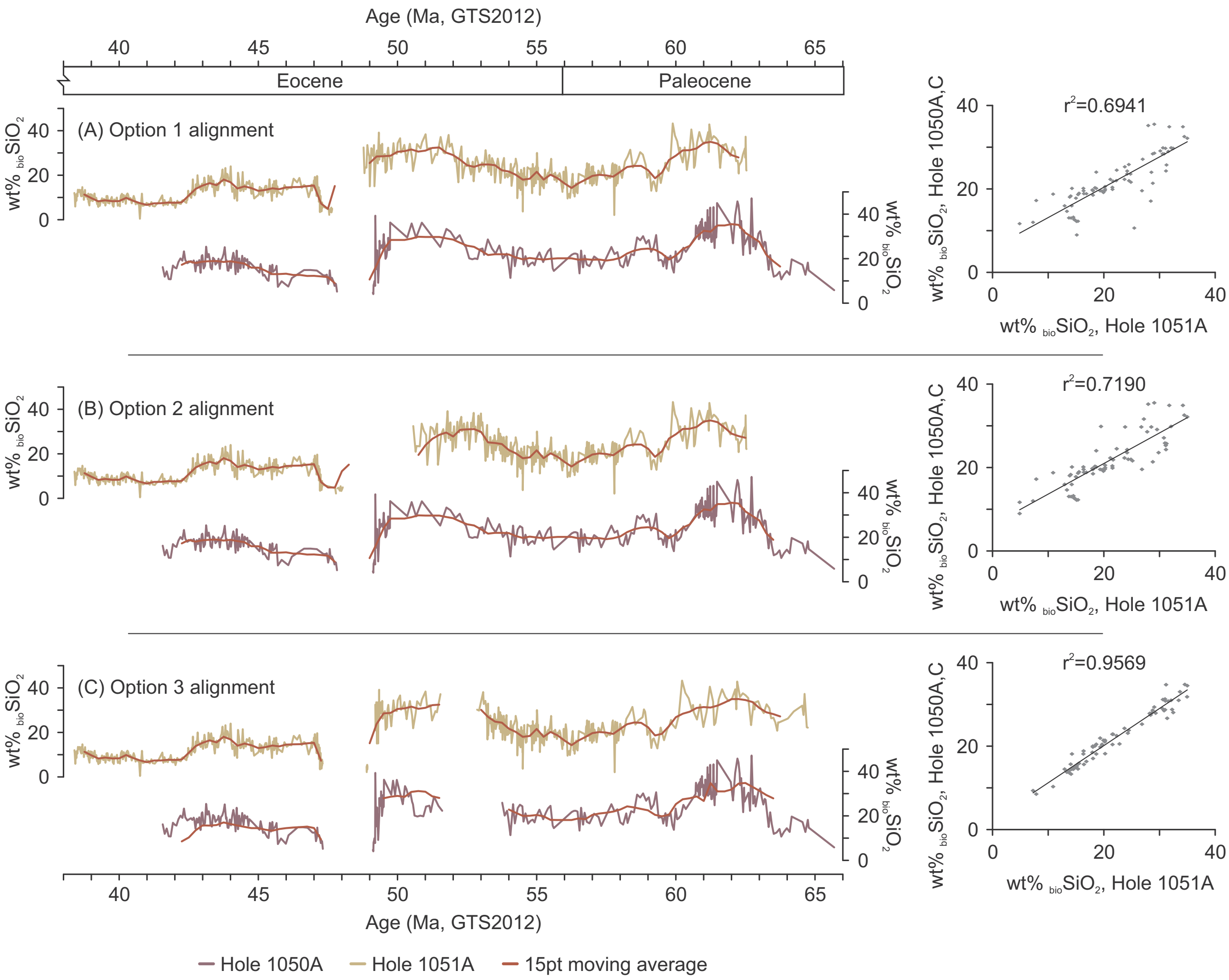

Fig. 10. Comparison of relative alignment of smoothed high-resolution weight percent biogenic opal (wt% $_{\text{bio}}SiO_2$) records from Holes 1050A,C and Hole 1051A on Option 1 (A), Option 2 (B), and Option 3 (C), along with linear regression plots showing the strength of statistical correlation. Biogenic opal records from Witkowski et al. (under review).

Table 7
Age model, Holes 1050A,C.

#	Event	Average depth (cmbsf)	Age (Ma, GTS2012)	Reference	GTS2012 calibration
12	B C19n	7.72	41.39	Ogg and Bardot (2001)	Gradstein et al. (2012)
14	B C19r	25.28	42.30	Ogg and Bardot (2001)	Gradstein et al. (2012)
21	B C20n	61.91	43.43	Ogg and Bardot (2001)	Gradstein et al. (2012)
27	B C20r	138.78	45.72	Ogg and Bardot (2001)	Gradstein et al. (2012)
33	B C21n	152.40	47.35	Adjusted to match the observed polarity pattern	Gradstein et al. (2012)
43	B *D. sublodoensis*	152.40	49.11	Norris et al. (1998c)	Gradstein et al. (2012)
45	B C22n	154.07	49.34	Ogg and Bardot (2001)	Gradstein et al. (2012)
55	T C23n	183.01	50.63	Ogg and Bardot (2001)	Gradstein et al. (2012)
61	B *C. crassus*	193.92	51.64	Norris et al. (1998c)	Norris et al. (2014b)
75	B *D. lodoensis*	193.92	53.70	Norris et al. (1998c)	Gradstein et al. (2012)
76	B C24n	198.73	53.98	Ogg and Bardot (2001)	Gradstein et al. (2012)
95	B C24r	253.40	57.10	Ogg and Bardot (2001)	Gradstein et al. (2012)
98	B C25n	257.43	57.66	Ogg and Bardot (2001)	Gradstein et al. (2012)
106	B C25r	275.30	58.96	Ogg and Bardot (2001)	Gradstein et al. (2012)
109	B C26n	279.31	59.24	Ogg and Bardot (2001)	Gradstein et al. (2012)
122	B C26r	332.54	62.22	Röhl et al. (2001)	Gradstein et al. (2012)
125	B C27n	344.95	62.52	Ogg and Bardot (2001)	Gradstein et al. (2012)
128	B C27r	370.62	63.49	Röhl et al. (2001)	Gradstein et al. (2012)
131	B C28n	387.43	64.67	Ogg and Bardot (2001)	Gradstein et al. (2012)
133	B C28r	392.09	64.96	Ogg and Bardot (2001)	Gradstein et al. (2012)
136	B C29n	395.50	65.69	Ogg and Bardot (2001)	Gradstein et al. (2012)

Table 8
Age model, Hole 1051A.

#	Event	Average depth (cmbsf)	Age (Ma, GTS2012)	Reference	GTS2012 calibration
1	B C17n	6.62	38.33	Edgar et al. (2010) based on shipboard magnetostratigraphy	Gradstein et al. (2012)
2	B C17r	15.49	38.62	Edgar et al. (2010) based on shipboard magnetostratigraphy	Gradstein et al. (2012)
4	B C18n.1n	54.67	39.63	Edgar et al. (2010)	Gradstein et al. (2012)
5	B C18n.1r	59.05	39.70	Edgar et al. (2010)	Gradstein et al. (2012)
7	B C18n.2n	79.09	40.15	Edgar et al. (2010)	Gradstein et al. (2012)
11	B C18r	128.27	41.15	Edgar et al. (2010)	Gradstein et al. (2012)
12	B C19n	133.17	41.39	Edgar et al. (2010)	Gradstein et al. (2012)
14	B C19r	165.89	42.30	Ogg and Bardot (2001)	Gradstein et al. (2012)
21	B C20n	240.27	43.43	Ogg and Bardot (2001)	Gradstein et al. (2012)
27	B C20r	348.55	45.72	Ogg and Bardot (2001)	Gradstein et al. (2012)
31	B C21n	377.84	47.35	Ogg and Bardot (2001)	Gradstein et al. (2012)
35	T *L. archaea*	378.39	47.98	Sanfilippo and Blome (2001)	Norris et al. (2014a)
42	B *S. pachystylus*	378.39	48.86	Sanfilippo and Blome (2001)	Norris et al. (2014a)
45	B C22n	394.72	49.34	Ogg and Bardot (2001)	Gradstein et al. (2012)
55	B C22r	410.45	50.63	Ogg and Bardot (2001)	Gradstein et al. (2012)
61	B *C. crassus*	418.68	51.64	Norris et al. (1998d)	Norris et al. (2014b)
67	T *M. marginodentata*	418.68	52.85	Norris et al. (1998d)	Gradstein et al. (2012)
68	B C24n.1n	420.17	53.07	Interpreted here	Gradstein et al. (2012)
70	B C24n.1r	422.40	53.20	Interpreted here	Gradstein et al. (2012)
71	B C24n.2n	427.48	53.27	Cramer et al. (2003)	Gradstein et al. (2012)
74	B C24n.2r	430.82	53.42	Cramer et al. (2003)	Gradstein et al. (2012)
76	B C24n.3n	449.76	53.98	Röhl et al. (2003)	Gradstein et al. (2012)
94	B C24r	524.30	57.10	Ogg and Bardot (2001)	Gradstein et al. (2012)
98	B C25n	529.70	57.66	Cramer et al. (2003)	Gradstein et al. (2012)
102	B *H. riedelii*	543.69	58.70	Norris et al. (1998d)	Gradstein et al. (2012)
105	T *H. kleinpellii*	543.69	58.80	Norris et al. (1998d)	Gradstein et al. (2012)
106	B C25r	549.00	58.96	Ogg and Bardot (2001)	Gradstein et al. (2012)
109	B C26n	564.82	59.24	Ogg and Bardot (2001)	Gradstein et al. (2012)
122	B C26r	601.93	62.22	Ogg and Bardot (2001)	Gradstein et al. (2012)
128	B C27r	620.75	63.49	Ogg and Bardot (2001)	Gradstein et al. (2012)
131	B C28n	642.47	64.67	Ogg and Bardot (2001)	Gradstein et al. (2012)

Option 3 age control is strongly supported by two independent measures, i.e., the distribution of diatom bioevents, as demonstrated in the graphic correlation above, and by the alignment of geochemical records from Holes 1050A,C and 1051A. In fact, the $_{bio}SiO_2$ records from Witkowski et al. (under review) could be used to perform a supplemented graphic correlation (Edwards, 1989) not only between Holes 1050A,C and Hole 1051A, but perhaps even among all Leg 171B sites.

Given the strongest statistical support for Option 3 (Fig. 10C), we propose revised and mutually consistent magnetostratigraphic age models for Holes 1050A,C (Table 7) and Hole 1051A (Table 8). In both age models, the hiati are constrained using biostratigraphic datums.

3.6. Calibration of diatom datums to the Geomagnetic Polarity Time Scale

With the revised age models for Holes 1050A,C and 1051A proposed here (Tables 7-8, respectively), it is possible to calibrate the age of the diatom events identified in the present study to the Geomagnetic Polarity Time Scale (GPTS) of Gradstein et al. (2012) (Table 9). In calculating the ages of the individual datums, we use linear interpolation and assume constant sedimentation rates between age model tiepoints. In chron assignments (Table 9), we give distance from chron base expressed as percent of average chron thickness at the respective Hole, consistent with the notation used in GTS2012 (for a discussion on alternative notations see Röhl et al., 2003, p. 570). This was not possible for the magnetozones truncated by the hiati. In Table 9, ages are proposed separately for Holes 1050A,C and Hole 1051A. Below, we briefly discuss the consistency of the resultant ages.

Overall, the ages established for the diatom datums are remarkably consistent between the study sites (Fig. 11). The regression plot indicates a clear linear relationship between ages from Holes 1050A,C and 1051A ($r^2 = 0.99$). Eight siliceous microfossil events (D13-D19 and E1, Table 9) from Hole 1050A, however, stand out in that they are tightly constrained with respect to depth (± 4.81 m), but their range of temporal uncertainty is surprisingly broad (± 2.36 myr). All these events occur between 144.58 and 154.20 cmbsf (Table 6), and thus straddle the upper hiatus (152.40 cmbsf). The broad range of temporal uncertainty is also compounded by the extremely low sediment accumulation rates in the interval immediately above the hiatus (~0.84 cm/kyr). Only two diatom bioevents (D15, D16 - Table 6) from Hole 1051A show comparably broad ranges of uncertainty with respect to time (± 1.71 myr). As in Hole 1050A, the depth range for these two events also straddles the upper hiatus. The temporal uncertainty range for D30 (T acme of *Hemiaulus jordani*; ± 0.51 myr) in Hole 1050A is also broader than for most other diatom events. The reason for this is that the depth range for this event extends across a diatom dissolution interval (Fig. 8).

The calibration of datums D13 through D19 should be treated as tentative, as there can be no certainty that magnetozone C21n is preserved in total in Hole 1050A. As explained in the Stratigraphy section above, we assume the presence of B C21n at ~152.4 cmbsf in order to match the observed polarity pattern. The termination of the upper hiatus in Hole 1050A, however, may fall at any level within C21n. This would explain the discrepancies in diatom bioevent distance from chron base between the study sites, as well as the differences in age calibrations (Table 9).

A number of diatom bioevents are identified within magnetozones that are truncated by the two major hiati considered here. Datums D22 through D24 and D26 in Hole 1050A occur within magnetozone C24n.3n. The distance from chron base cannot be estimated for these datums because they are immediately subjacent to the lower hiatus. The same can be related to datums D37 through D40 in Hole 1051A, which occur within magnetozone C25r. Although the duration of the hiatus is estimated at only ~250 kyrs, it prevents a tight contraint on the distance from chron base for datums D37-D40. Finally, datum D49

Table 9
Diatom datum calibration to the Geomagnetic Polarity Time Scale of Gradstein et al. (2012).

#	Diatom bioevents	Holes 1050A,C					Hole 1051A					Mean age (Ma)
		Average depth (cmbsf)	± (m)	Distance from chron base (Option 3)	Age (Ma; Option 3)	± (myrs)	Average depth (cmbsf)	±	Distance from chron base (Option 3)	Age (Ma; Option 3)	± (myrs)	
D1	T *Fenneria kanayae*	44.32	4.75	C20n.5	42.89	0.15	221.41	4.06	C20n.3	43.15	0.06	43.02
D2	B *Diplomenora cocconeiforma*	53.82	4.75	C20n.2	43.18	0.15	230.73	5.26	C20n.1	43.29	0.08	43.23
D3	B *Quadrocistella montana*	63.33	4.77	C20n/C20r transition	43.47	0.14	250.43	6.47	C20r.9	43.65	0.14	43.56
D4	T '*Hemiaulus* sp., asymmetric'	82.32	4.74	C20r.7	44.04	0.14	260.60	3.70	C20r.8	43.86	0.08	43.95
D5	B *Drepanotheca bivittata*	82.32	4.74	C20r.7	44.04	0.14	269.10	4.80	C20r.7	44.04	0.10	44.04
D6	B *Entogoniopsis foveatamorpha*	91.83	4.77	C20r.6	44.32	0.14	288.30	4.80	C20r.6	44.45	0.10	44.39
D7	T *Hemiaulus curvatulus* acme	120.60	4.80	C20r.2	45.18	0.14	317.15	4.85	C20r.3	45.06	0.10	45.12
D8	T *Craspedodiscus moelleri*	130.20	4.80	C20r.1	45.47	0.14	336.40	4.80	C20r.1	45.47	0.10	45.47
D9	B *Xanthiopyxis oblonga*	139.79	4.79	C20r/C21n transition	45.85	0.57	346.05	4.85	C20r/C21n transition	45.67	0.18	45.76
D10	B *Hemiaulus curvatulus*	139.79	4.79	C20r/C21n transition	45.85	0.57	346.05	4.85	C20r/C21n transition	45.67	0.18	45.76
D11	B *Hemiaulus mesolepta*	139.79	4.79	C20r/C21n transition	45.85	0.57	355.75	4.85	C21n.8	46.12	0.27	45.98
D12	B '*Hemiaulus* sp., asymmetric'	139.79	4.79	C20r/C21n transition	45.85	0.57	365.40	4.80	C21n.4	46.66	0.27	46.25
D13	B *Hemiaulus crenatus*, coarse	149.39	4.81	C21n.2	46.99	2.36	365.40	4.80	C21n.4	46.66	0.27	46.82
D14	B *Craspedodiscus moelleri* acme	149.39	4.81	C21n.2	46.99	2.36	365.40	4.80	C21n.4	46.66	0.27	46.82
D15	B *Fenneria kanayae*	149.39	4.81	C21n.2	46.99	2.36	375.00	4.80	C21n.1	47.19	1.71	47.09
D16	B *Fenneria brachiata*	149.39	4.81	C21n.2	46.99	2.36	375.00	4.80	C21n.1	47.19	1.71	47.09
D17	B *Rocella praenitida*	149.39	4.81	C21n.2	46.99	2.36	394.95	3.15	C22n/C22r transition	49.36	0.26	48.18
D18	T *Hemiaulus originalis*	149.39	4.81	C21n.2	46.99	2.36	394.95	3.15	C22n/C22r transition	49.36	0.26	48.18
D19	T *Rhizosolenia hebetata*	149.39	4.81	C21n.2	46.99	2.36	394.95	3.15	C22n/C22r transition	49.36	0.26	48.18
D20	T *Coscinodiscus mirabilis*	159.00	4.80	C22r.8	49.56	0.21	394.95	3.15	C22n/C22r transition	49.36	0.26	49.46
D21	B *Craspedodiscus moelleri*	168.49	4.69	C22r.5	49.98	0.21	403.82	5.77	C22r.4	50.09	0.47	50.04
D22	B *Coscinodiscus mirabilis*	195.19	4.79	Within C24n.3n	53.77	0.28	433.60	4.80	C24n.3n.8	53.50	0.14	53.64
D23	B *Radialiplicata clavigera*	195.19	4.79	Within C24n.3n	53.77	0.28	443.20	4.80	C24n.3n.3	53.79	0.14	53.78
D24	B *Quadrocistella rectanoguma*	195.19	4.79	Within C24n.3n	53.77	0.28	443.20	4.80	C24n.3n.3	53.79	0.14	53.78
D25	B *Distephanosira architecturalis*	–	–	–	–	–	443.20	4.80	C24n.3n.3	53.79	0.14	–
D26	B *Hemiaulus originalis*	195.19	4.79	Within C24n.3n	53.77	0.28	452.80	4.80	C24r.95	54.11	0.20	53.94
D27	T *Hemiaulus peripterus*	204.73	4.75	C24r.9	54.33	0.27	465.00	4.30	C24r.8	54.62	0.18	54.47
D28	T *Hemiaulus jordani*	215.06	5.58	C24r.7	54.91	0.32	473.40	4.10	C24r.7	54.97	0.17	54.94
D29	B *Pyrgupyxis gracilis*	224.01	3.37	C24r.55	55.42	0.19	483.00	5.50	C24r.55	55.37	0.23	55.40
D30	T *Hemiaulus jordani* acme	229.63	8.99	C24r.4	55.75	0.51	492.90	4.40	C24r.4	55.79	0.18	55.77
D31	B *Rhizosolenia hebetata*	233.00	5.63	C24r.4	55.94	0.32	492.87	4.38	C24r.4	55.79	0.18	55.86
D32	T *Medlinia fenestrata*	240.43	1.80	C24r.2	56.36	0.10	511.58	5.27	C24r.2	56.57	0.22	56.47
D33	T *Trochosira* cf. *T. spinosa*	245.22	2.99	C24r.15	56.63	0.17	520.84	3.99	C24r.05	56.96	0.20	56.80
D34	B *Hemiaulus jordani*	252.99	4.79	C24r/C25n transition	57.08	0.60	529.55	4.75	C25n/C25r transition	57.64	0.36	57.36
D35	T *Eunotogramma variabile*	262.64	4.86	C25r.7	58.04	0.35	529.57	4.73	C25n/C25r transition	57.64	0.36	57.84
D36	T *Pterotheca kittoniana*	262.64	4.86	C25r.7	58.04	0.35	529.57	4.73	C25n/C25r transition	57.64	0.36	57.84
D37	B *Cylindrospira simsiae*	262.64	4.86	C25r.7	58.04	0.35	539.10	4.80	mid C25r	58.36	0.45	58.20
D38	B *Fenneria nascens*	262.64	4.86	C25r.7	58.04	0.35	539.10	4.80	Mid C25r	58.36	0.45	58.20
D39	T *Trinacria pileolus*	262.64	4.86	C25r.7	58.04	0.35	539.10	4.80	Mid C25r	58.36	0.45	58.20
D40	B *Gombosia stomata*	271.90	4.40	C25r.2	58.71	0.32	539.10	4.80	Mid C25r	58.36	0.45	58.53
D41	B *Hemiaulus incurvus*	271.90	4.40	C25r.2	58.71	0.32	548.70	4.80	C25r/C26n transition	58.95	0.09	58.83
D42	B *Hemiaulus inaequilaterus*	281.26	4.97	C26r.95	59.35	0.28	548.70	4.80	C25r/C26n transition	58.95	0.09	59.15
D43	B *Trochosira* cf. *T. spinosa* acme	281.26	4.97	C26r.95	59.35	0.28	559.85	3.25	C26n.4	59.15	0.06	59.25
D44	B *X. structuralis*	301.08	4.82	C26r.6	60.46	0.27	577.50	4.80	C26r.7	60.26	0.39	60.36
D45	T *P. evermanni*	301.08	4.82	C26r.6	60.46	0.27	577.50	4.80	C26r.7	60.26	0.39	60.36
D46	B *H. peripterus*	310.40	4.51	C26r.4	60.98	0.25	587.15	4.85	C26r.4	61.03	0.39	61.01
D47	B *T. praetenuis*	310.40	4.51	C26r.4	60.98	0.25	587.15	4.85	C26r.4	61.03	0.39	61.01
D48	T *Liradiscus* sp. 1 acme	321.49	6.58	C26r.2	61.60	0.37	596.85	4.85	C26r.15	61.81	0.39	61.71

(*continued on next page*)

Table 9 (*continued*)

#	Diatom bioevents	Holes 1050A,C					Hole 1051A					Mean age (Ma)
		Average depth (cmbsf)	± (m)	Distance from chron base (Option 3)	Age (Ma; Option 3)	± (myrs)	Average depth (cmbsf)	±	Distance from chron base (Option 3)	Age (Ma; Option 3)	± (myrs)	
D49	B *Proboscia ciesielskii*	337.67	1.54	C27n.6	62.34	0.04	606.49	4.79	Within C27	62.53	0.32	62.44
S1	B *Macrora barbadensis*	91.83	4.77	C20r.6	44.32	0.14	278.70	4.80	C20r.6	44.25	0.10	44.28
E1	B *Ebriopsis crenulata*	149.39	4.81	C21n.2	46.99	2.36	365.40	4.80	C21n.4	46.66	0.27	46.82

in Hole 1051A can only be classified as "within C27", as the polarity patterns are ambiguous in the basal part of this Hole.

Excluding the potentially problematic datums identified close to the upper hiatus and discussed separately above (D13 through D19), the average diatom datum uncertainty range for Holes 1050A,C is 0.29 myrs, and for Hole 1051A is 0.24 myrs (Table 9). Once these datums are considered in a paleobiogeographic context (see Witkowski, 2018), and any possible diachroneity is evaluated, the Paleogene diatom bioevents identified herein will have the full potential for providing high-fidelity age control suitable for high-resolution paleoceanographic studies.

4. Discussion

4.1. Two major hiati in Hole 1051A?

The key finding of the present work is that Sites 1050 and 1051 lack continuous records not only of the EMET (~47.85 Ma) (Norris et al., 1998c, 1998d), but also of magnetozones C23 and C24 (specifically from ~54 to ~51.5 Ma) (Fig. 5). Sites 1050 and 1051 are located in close proximity, on a slope characterized by a similar angle and topography (Norris et al., 1998a). Geological and geochemical evidence shows that through the Paleogene, both sites were bathed by similar water masses (Norris et al., 2001; Fontorbe et al., 2016). It therefore seems a reasonable assumption that both hiati should be present at both sites. Yet, in previous studies, the lower hiatus was detected only in Hole 1050A. Several factors seem to have been involved.

First, in Hole 1051A, the proposed lower hiatus occurs at a core break between Cores 1051A-44X and 1051A-45X (Figs. 8, 9C). Second, the hiatus lacks an apparent lithological expression such as the prominent silicified hardground associated with the upper hiatus in Core 1050A-16X (see Fig. 8 in Norris et al., 1998c for a correlative hardground from Hole 1050B). In addition, no clear indication of a hiatus is found in the correlative interval of Hole 1051B. There are, however, other lithological clues that do support a prolonged period of erosion or non-deposition at both study sites. Core 1051A-44X, immediately superjacent to the lower hiatus, is composed of siliceous nannofossil chalk, and Core 1051A-45X, below the hiatus, comprises porcellanite with clay and nannofossils (Norris et al., 1998d). Given that SiO_2-undersaturated ocean waters facilitate dissolution of siliceous microfossils at the sediment-water interface (e.g., DeMaster, 2014), the porcellanization in Core 1051A-45X may be an indication of a break in deposition caused by the flow of corrosive bottom waters. In Hole 1050A, the lower hiatus at ~193.92 cmbsf within Core 1050A-21X also lacks an apparent lithological expression, and no change in sediment lithology is documented in the visual core descriptions (Norris et al., 1998c). Immediately below the hiatus, however, there is a prominent siliceous microfossil dissolution interval (Figs. 6–8). Thus, both study sites display evidence for prolonged exposure of siliceous microfossils to SiO_2-undersaturated waters at the sediment-water interface.

The third reason why the proposed lower hiatus was not detected in previous studies may be purely pragmatic. Most micropaleontological studies on Site 1051 published to date focus on specific microfossil groups. Yet, unlike the strong radiolarian support for the upper hiatus (Sanfilippo and Blome, 2001), no individual microfossil group gives a clear indication of the presence of the lower hiatus in Hole 1051A. The identification of the hiatus was facilitated by integration of data from multiple microfossil groups examined by previous workers (e.g., Norris et al., 1998d; Mita, 2001; Sanfilippo and Blome, 2001; Cramer et al., 2003; Luciani and Giusberti, 2014; Luciani et al., 2016, 2017).

Reconstructing geologic events through the EMET is a major challenge due to the paucity of uninterrupted sedimentary records spanning this interval (Bornemann et al., 2016; Cappelli et al., 2019). Aubry (1995) documented stratigraphic gaps in the upper lower Eocene through lower middle Eocene interval at over 50 Atlantic sites. Despite their variable duration, many of the discontinuities considered by Aubry (1995) fall within nannofossil zone NP14 spanning the EMET. A

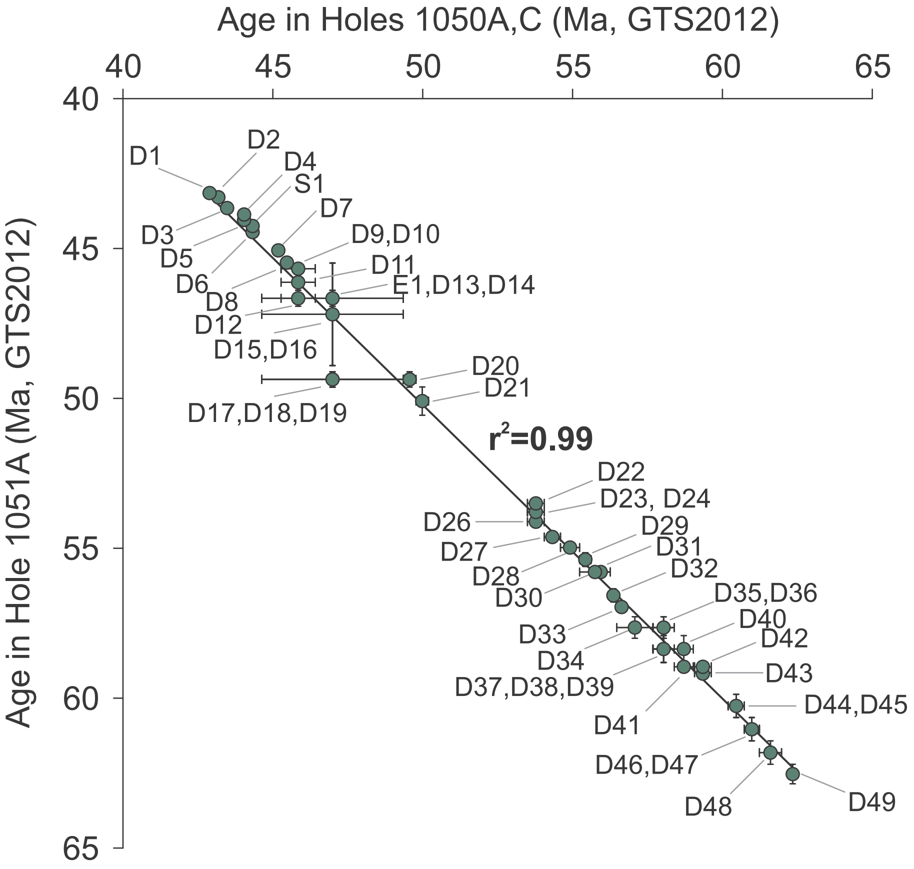

Fig. 11. Comparison of the ages of diatom datums from Holes 1050A,C and 1051A, calibrated to the Geomagnetic Polarity Time Scale of Gradstein et al. (2012), based on Option 3. For a list of diatom datums see Table 9.

comparable age of ~47 Ma is also postulated for acoustic Horizon H3 identified in the IODP Exp 342 sites off New Foundland (Boyle et al., 2017), and interpreted to mark the onset of vigorous deep-water circulation in the North Atlantic. Numerous sites examined by Aubry (1995), especially in the western North Atlantic, also include hiati within magnetozones C23 and C24. Thus, the stratigraphic patterns observed at Sites 1050 and 1051 are broadly consistent with the regional trends.

4.2. Implications for paleoceanography

The recognition of the lower hiatus at Site 1051 has important implications for establishing the age of a number of carbon cycle perturbations documented in Hole 1051A (Cramer et al., 2003; Nicolo et al., 2007; Luciani et al., 2017) (Fig. 12), as well as for reconstructing silicic acid concentration and uptake shifts in the western North Atlantic (Fig. 13).

Luciani et al. (2017) documented at least nine negative excursions in bulk $\delta^{13}C$ records from Hole 1051A. Based on Option 2 age control, these were identified as, bottom to top: H1 (=ETM2), H2, I1, I2, J, K/X (=ETM3), L1, L2, and M events (Fig. 12), potentially providing a detailed record of the onset and early part of the EECO (see definitions in Luciani et al., 2016 and Westerhold et al., 2017). When rescaled to age control Option 3, however, it appears the bulk $\delta^{13}C$ record from Hole 1051A is missing a ~1.5 myr portion of the early phase of the EECO. Further, the excursions identified by Luciani et al. (2017) as K through M may in fact represent the minor and less-well understood events of the latter part of the EECO. Based on their age interpolated from Option 3, and following the hyperthermal nomenclature from Westerhold et al. (2017), we tentatively identify these as: N (=K/X of Luciani et al., 2017), R (=L1 in Luciani et al., 2017), T (=L2 in Luciani et al., 2017), and C22nH3 event (=M in Luciani et al., 2017) (Fig. 12). This part of the stable isotope record from Luciani et al. (2017) has a lower stratigraphic resolution than the part encompassing events H1 through J, and therefore the above revised assignments should be treated as approximate. Finally, Fig. 12A–B shows how the trends in bulk $\delta^{13}C$ records from Luciani et al. (2017) are misaligned with the trends displayed by the benthic $\delta^{13}C$ record from ODP Site 1209 (Westerhold et al., 2018) when plotted on age control Options 1 and 2. When rescaled to Option 3, however, the overall trends in bulk $\delta^{13}C$ records are in good agreement with the record from Site 1209 (Fig. 12C).

A recent reconstruction of silicon isotope records from the BN cores (Fontorbe et al., 2016) relies mostly on data from Holes 1050A and 1051A (Fig. 13A). No details of the age model were provided by Fontorbe et al. (2016), but presumably the age control conforms to Option 1 considered here. We show that when the $\delta^{30}Si$ records are rescaled to Option 3, the relative positions of the datapoints from both Holes change, and the resultant picture of the radiolarian and sponge-spicule silicon isotope records is different from the original (Fig. 13A vs B). Rescaled records become shorter, and the major features shift toward younger ages in the older part of the record (~60 through 50 Ma), and toward older ages in the younger part of the record (~50 through 40 Ma). Notably, the prominent peak in radiolarian $\delta^{30}Si$ through the EECO visible in the records plotted on the original age model becomes considerably broader when rescaled. Further, the rescaled radiolarian and sponge $\delta^{30}Si$ records display essentially the same trends through time, which is likely to be reflected in the surface-to-deep $\delta^{30}Si$ gradient, i.e., an important proxy in silicic acid concentration and uptake reconstructions (see Egan et al., 2013). Finally, when both hiati at both Holes are taken into consideration (mean duration from Sites 1050 and

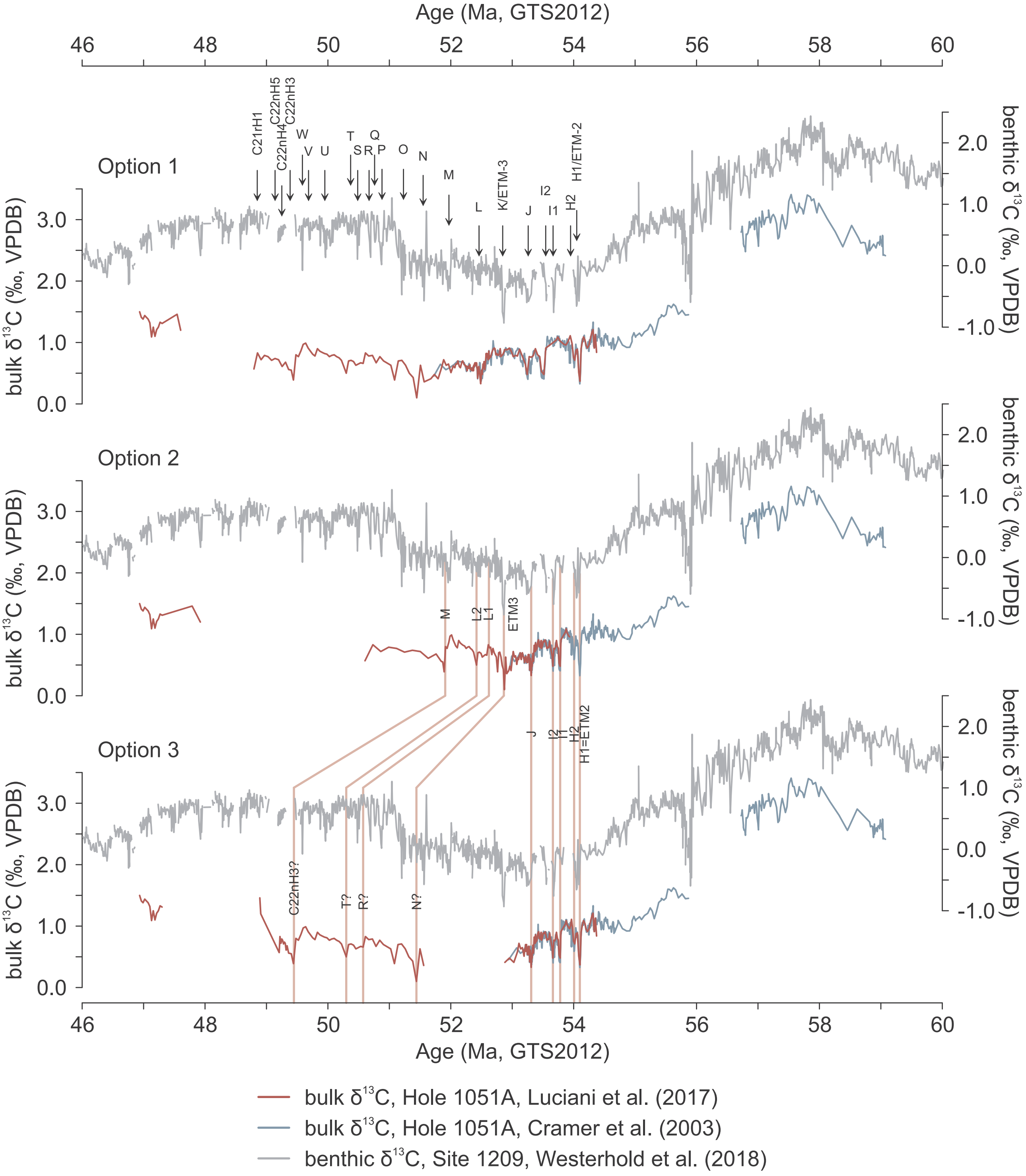

Fig. 12. Comparison of Hole 1051A late Paleocene through early Eocene bulk $\delta^{13}C$ records from Cramer et al. (2003) and Luciani et al. (2017) plotted on Option 1 (A), Option 2 (B) and Option 3 (C). $\delta^{13}C$ event labelling in panel (B) from Luciani et al. (2017). Benthic $\delta^{13}C$ record from ODP Site 1209 (Westerhold et al., 2018) along with global early Eocene hyperthermal events (Westerhold et al., 2017) is provided in each panel in order to highlight the consistency of trends in Hole 1051A bulk $\delta^{13}C$ records relative to a continuous record.

1051 plotted in Fig. 13B), the peak in both radiolarian and sponge $\delta^{30}Si$ records is separated from both the older and the younger parts of the record, thus making it difficult for general interpretations of $\delta^{30}Si$ variability through the early part of the EECO.

Given the discontinuous record of the EECO and EMET at BN sites, an overall conclusion from the above short review is that further insight into the early Eocene paleoceanography is needed for the western North Atlantic. Establishing a continuous stratigraphic record through the early Cenozoic is especially important for reconstructing the ${}_{bio}SiO_2$ accumulation history: the western North Atlantic has been the key locus of biosiliceous sedimentation through the early Cenozoic (Barron et al., 2015; Witkowski et al., under review). Western North Atlantic sites are therefore the most likely to shed light on the links between global carbon and silicon cycling, especially in the context of the ongoing

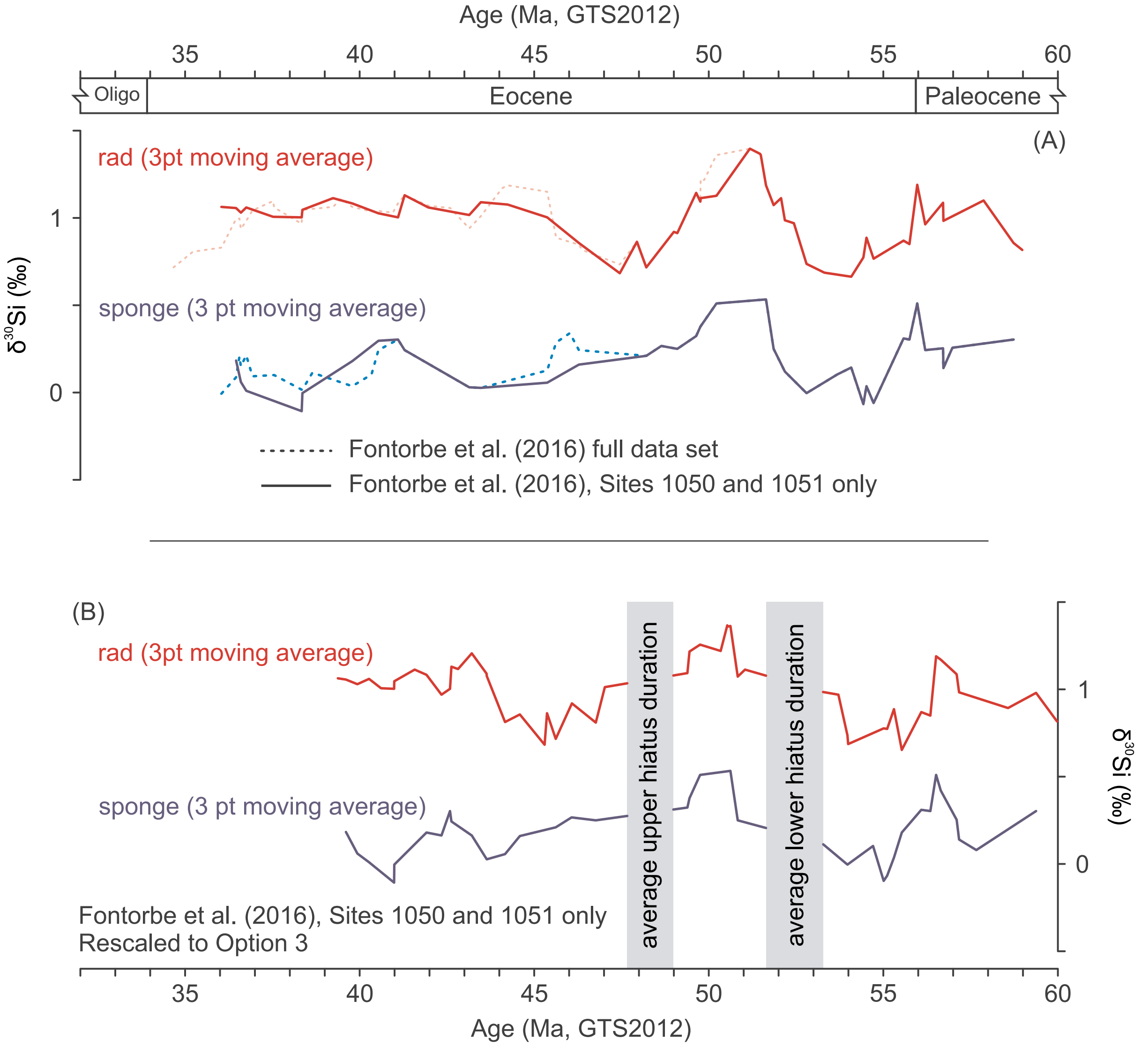

Fig. 13. Smoothed δ^{30}Si records from Holes 1050A,C and Hole 1051A (Fontorbe et al., 2016) plotted on the original age model (A) and using Option 3 age control (B). Note that data from Holes 1050A,C and Hole 1051A comprise the majority of the dataset used in Fontorbe et al. (2016) - see dashed lines for comparison in panel (A). In panel B, the duration of both hiati is an average calculated from the onset and termination ages taken from both study sites. Oligo = Oligocene.

discussion on the mode of operation of the silicate weathering thermostat (e.g., Penman, 2016; Caves et al., 2016; van der Ploeg et al., 2018; Penman et al., 2019). Future studies exploring these relationships will need to focus on supplementing the gaps in the BN records.

4.3. *Paleogene diatom biostratigraphy – refinements and recommendations for future studies*

Event-based biostratigraphic approach has proven highly successful in refining the Southern Ocean Neogene diatom biochronology (Cody et al., 2008, 2012; Florindo et al., 2013). The present work is largely exploratory in identifying the possible diatom datums that could be useful for correlation in the western North Atlantic. At least 29 diatom events highlighted here were considered in Barron et al. (2015). Ages for some of the events (e.g., T *P. evermanni*) are vastly different, showing that further work is necessary to refine them. Finally, events like B *H. mesolepta* have remarkably consistent ages (compare Barron et al., 2015, and Table 9 herein), suggesting they are suitable for use as zonal markers likely on a global scale.

Of the 49 diatom events considered in this study, only three (B *H. incurvus*, B *P. gracilis*, B *F. kanayae*) are part of the existing low-latitude zonation (see Table 1 in Barron et al., 2015). As discussed by Witkowski (2018), low-latitude diatom zonal markers from the Fenner (1984) zonation (Fig. 2E) are extremely rare or absent in the BN cores. However, correlating between the BN sites and tropical sites could potentially be facilitated by a reinvestigation of the numerous diatom-bearing holes cored in the early DSDP era. There are also numerous Paleogene deep-sea sites for which no diatom reports were ever published for reasons discussed in the introduction. One such largely neglected area of study is the mid-latitude eastern North Atlantic Ocean (e.g., sites drilled on DSDP Legs 48 and 80–81; see Baldauf, 1984; Ling, 1985). Tying these sites into the framework proposed here is likely to fill the gaps in our current understanding of the paleobiogeographic distribution of the diatom taxa found in the western North Atlantic. Expanding our knowledge of the Paleogene diatom assemblages into the eastern North Atlantic could also provide a stronger link to the Eurasian Platform sites.

Although only one event considered here (B *P. gracilis*) is used as a zonal marker in the Eurasian Platform zonation (Table 1 in Barron et al., 2015), surprisingly many of the taxa reported here are found in the mid- to high-latitude Eurasian Platform sections investigated by numerous Russian workers (e.g., Jousé, 1951; Krotov and Schibkova, 1959; Strelnikova, 1992; Khokhlova and Oreshkina, 1999; Oreshkina and Oberhänsli, 2003; Oreshkina and Aleksandrova, 2007, 2017; Aleksandrova et al., 2012; see also Barron et al., 2015, for a tentative correlation to the Eocene tropical deep-sea diatom zonation) (Fig. 2I–J). Given the lack of calcareous nannofossils in many of the diatom-bearing successions on the Eurasian Platform, direct correlation to the deep-sea sites is often impossible (Aleksandrova et al., 2012). In recent years, however, a correlation between the Eurasian Platform and deep-sea sites was successfully developed using dinocyst biostratigraphy. Dinocyst bioevents are also increasingly well-constrained for the mid-latitude North Atlantic (Eldrett et al., 2004; Egger et al., 2016). Further progress in diatom biostratigraphy and palynology may therefore result in establishing a more robust correlation between the western North Atlantic deep-sea sites and Eurasian Platform sections than previously available.

Another highly relevant issue is the high rate of survivorship of Cretaceous diatom taxa reported globally by Renaudie et al. (2018). Despite the paucity of sites that preserve latest Cretaceous and/or earliest Cenozoic siliceous phytoplankton (e.g., Harwood, 1988; Hollis et al., 1995), the K/Pg extinction is considered to have made relatively little impact on diatoms, likely because of their ability to form resting spores to aid survival through periods of unfavorable environmental conditions (Kitchell et al., 1986; Sims et al., 2006). Indeed, the statistical analysis by Renaudie et al. (2018) indicates a prolonged, gradual extinction of diatom taxa that originated in the Cretaceous. Few Cretaceous survivor taxa were observed in the present study (most notably *C. rossicus* and *P. evermanni*), but their global distribution (see Harwood, 1988; Witkowski et al., 2011) required distinguishing between reworked occurrences and genuine extinctions. Our main criteria were: 1) continuous versus spotty occurrences; and 2) preservation. The occurrences of *C. rossicus* are discontinuous at both study sites, and valves tend to be fragmented. Conversely, *P. evermanni* displays good preservation and occurs continuously in the basal parts of Sites 1050 and 1051. T *P. evermanni* (D45; Tables 6, 9), proved highly consistent between the study holes, and should be investigated further at other sites, as a potentially global biostratigraphic marker for the middle Paleocene.

As discussed in Witkowski et al. (under review), the BN cores offer the longest currently known single-locality record of diatom evolution through the Paleogene. An outstanding issue that cannot be resolved in this study, however, is the missing record of diatom evolution through the time periods spanning the two major hiati in Holes 1050A,C and 1051A. The comprehensive compilation by Barron et al. (2015) suggests that Holes 94, 343, 390A and Site U1403 could bridge the gap across the upper hiatus in Leg 171B cores (~47.5–49 Ma). The lower hiatus corresponds to ~52–53.5 Ma, which means that data from Holes 94, 390A and 553A could provide insight on the missing record from the sites examined here. Verifying this is an important direction for future studies to follow.

There are two general recommendations that we consider highly relevant to enable further progress in Paleogene diatom studies. First, it is essential that diatom assemblages be examined in non-sieved residues (Witkowski et al., 2015; Renaudie et al., 2018), using high magnification, and preferably DIC optics. Sieving eliminates small, often age-diagnostic taxa, and has led to decade-long misunderstandings in dating some of the key diatom-bearing deposits (see the range of uncertainties in age determinations e.g., in Ross and Sims, 1985, and Ross, 1995; see also discussion on sieving in Witkowski et al., 2015). Despite the widespread belief that Cretaceous and Paleogene diatom assemblages are characterized by common large and heavily silicified forms (Finkel et al., 2005; Scherer et al., 2007), numerous taxa documented in this study (e.g., *P. kittoniana*, *Trochosira* cf. *T. spinosa*) are relatively abundant but small and thus easily overlooked. *Trochosira* cf. *T. spinosa* is a notable example that diatom assemblage work requires high-power optics. This fragile form is easily broken, and the valve face relief is difficult to distinguish from circular debris due to the faint marginal ring of wedge-shaped bosses (Pl. III, Fig. 18).

Second, it is essential that fossil diatom studies follow the latest developments in diatom taxonomy, especially with regard to new taxa separated from poorly understood, and often extremely long-ranging genera (see Sims et al., under review, for a discussion on new taxa separated from the genus *Triceratium* Ehrenberg). For instance, this study is the first to distinguish at least five morphogroups within the genus *Distephanosira* Gleser, which to date was considered a monotypic taxon, with the single species *D. architecturalis* (Brun) Gleser (see Pl. I, Fig. 6 versus Pl. II, Fig. 13, and range charts in Tables S3–S4 in the online Supplementary materials). Witkowski et al. (2014) compiled deep-sea occurrences of *Distephanosira* and indicated an early Eocene to late Oligocene range of these published records. Assuming that this range is based on the occurrences of multiple species identified as *D. architecturalis*, it is probably grossly overestimated. As presented here, numerous diatom taxa occurring in the BN cores have short stratigraphic ranges and high potential for biostratigraphic correlation.

As more data on diatom evolution and distribution through space and time are generated, it will be possible to apply more sophisticated stratigraphic techniques, like supplemented graphic correlation (Edwards, 1989), or constrained optimization (CONOP), to the expanding Paleogene diatom datum dataset. Until this is accomplished, further work is needed on both recent and legacy sites. In this, we echo Renaudie et al. (2018), who call for performing diatom assemblage studies not as a byproduct of other research projects, but for the sake of documenting taxonomy, revealing trends in diversity, considering causal factors in evolutionary transitions (e.g., Crampton et al., 2016), and for providing highly refined geological event resolution via biostratigraphic correlations like those developed herein.

5. Conclusions

The main outcomes of this work are summarized below:

1. Previous studies (Norris et al., 1998b, 1998c; Ogg and Bardot, 2001; Cramer et al., 2003; Luciani and Giusberti, 2014; Luciani et al., 2016, 2017) identified two major hiati in Hole 1050A, and only one major discontinuity in Hole 1051A, which is broadly correlative to the upper hiatus in Hole 1050A. The estimates of the duration of the upper hiatus in Hole 1051A, however, vary, leading to ~2 myr uncertainties in age control. The minor hiatus truncating calcareous nannofossil Zone NP7 in Hole 1051A is not considered in more detail in the present study.
2. Using a compilation of published foraminiferal, nannofossil and radiolarian bioevents we establish that the upper hiatus in Holes 1050A and 1051A juxtaposes magnetozone C21n on C22n, consistent with previous studies. However, we reinterpret the duration of the lower hiatus in Hole 1050A, and propose that it juxtaposes magnetozone C23n on C24n. Further, we present strong evidence for the presence of a correlative lower hiatus in Hole 1051A.
3. By means of graphic correlation, we compare the depths of magnetic reversals to the placement of 49 diatom bioevents identified in Holes 1050A,C and 1051A. We find the strongest support for the line of correlation that assumes the presence of two correlative hiati at both study sites.
4. The diatom datums are calibrated to GTS2012; the interpolated ages are remarkably consistent between the study sites, with an average range of temporal uncertainty < ± 0.3 myr for most datums.
5. We use high-resolution weight percent biogenic opal records from Holes 1050A,C and 1051A (from Witkowski et al., under review) to gain a quantitative insight on the correlation between the study sites. Using the age models developed here, the relative alignment of biogenic opal records between Holes 1050A,C and 1051A is improved considerably in comparison to previous age models.
6. The new age models developed here have profound consequences for interpreting paleoceanographic and paleoclimatic records

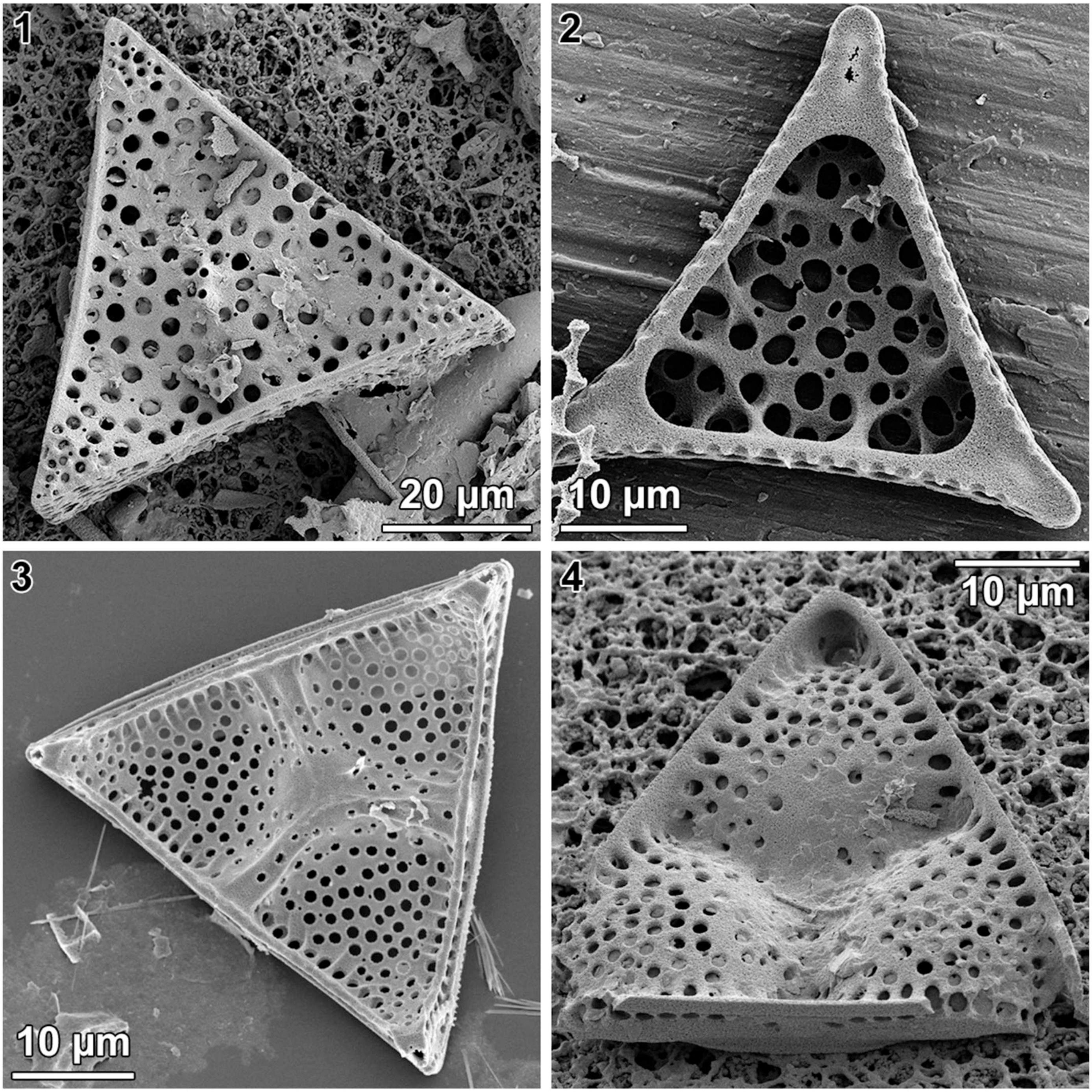

Plate IV. Scanning electron micrographs of new taxa proposed herein.
Figs. 1–2. *Fenneria nascens* Bryłka and Witkowski, n.sp. Sample ODP 171B-1051A-42X-1, 50–51 cm. Fig. 1. External view. Fig. 2. Internal view.
Figs. 3–4. *Entogoniopsis foveatamorpha* Witkowski, n.sp. Fig. 3. External view. Sample ODP 171B-1050A-14X-1, 100–101 cm. Fig. 4. Internal view. Sample ODP 1051B-8H-5, 5–6 cm.

generated from the BN cores. We show that the negative δ^{13}C excursions identified in bulk records from Hole 1051A are not associated with events K/X(=ETM3), L1, L2 and M, as proposed by Luciani et al. (2017), but more likely represent events N, R, T, and C22nH3 (terminology from Westerhold et al., 2017), respectively.

7. δ^{30}Si records from BN cores (Fontorbe et al., 2016) are mostly based on Holes 1050A,C and 1051A. Rescaling the original data to the age models proposed here results in a considerable change to the shapes of the δ^{30}Si curves derived from radiolarian tests and sponge spicules. Specifically, the rescaled δ^{30}Si records become ~3 myrs shorter, and the long-term trends between the radiolarian and sponge records become remarkably consistent. This is likely to impact the future NW Atlantic Ocean paleoproductivity reconstructions relying on the surface-to-deep δ^{30}Si gradient.
8. Finally, and most importantly, we demonstrate the high potential of early Paleogene diatom bioevents for establishing high-fidelity age control for deep-sea sites.

Declaration of competing interest

The authors declare that they have no known competing financial interests or personal relationships that could have appeared to influence the work reported in this paper.

Acknowledgements

This study was supported from the Polish National Science Center grant no. 2014/13/B/ST10/02988 to JW. Walter Hale, Holger Kuhlmann, and the IODP Bremen Core Repository staff are thanked for efficient handling of multiple sample requests. Isabella Raffi, Ursula Röhl and Diederik Liebrand are thanked for providing the necessary literature. Marta Bąk is thanked for her useful comments on radiolarian biostratigraphy. We are grateful to Steven Bohaty and Kevin McCartney for their continued support for our work. Constructive comments from two anonymous reviewers are gratefully acknowledged.

Appendix A. Taxonomic appendix

New taxa:

***Entogoniopsis foveatamorpha* J. Witkowski, n. sp.** (Pl. I, Fig. 8; Pl. IV, Figs. 3–4)

Holotype: University of Szczecin Herbarium, SZCZ 24565, 38–63 μm, Slide A (Pl. I, Fig. 8)

Description: Valves tripolar, usually with straight sides, and pointed to narrowly rounded poles. Valve face undulate, with a central trifolium, and low polar elevations bearing small hyaline linking spines, and small distal pseudocelli. Depressed valve face sectors perforated with poroid areolae arranged in parallel rows. The trifolium center and those portions of the trifolium that are adjacent to the valve face margins, are hyaline. The remaining part of the trifolium is sparsely areolated. A single rimoportula is located eccentrically on the trifolium. Entire valve face surrounded by a marginal ridge that is nearly level with the summits of the polar elevations. Mantle shallow, steep, perforated by large poroid areolae, except for the portion adjacent to the trifolium. On the valve exterior, marginal costae, oriented perpendicular to the marginal ridge, protrude a short distance inwardly. On the interior, the spaces between the mantle areolae are thickened to form internal costae.

Type material: Sample ODP 171B-1050A-14X-1, 100–101 cm (sub-bottom depth: 125.40 cmbsf).

Type level: middle Eocene, within magnetozone C20r.

Stratigraphic range: from 87.06 cmbsf to the top of Hole 1050A, equivalent to upper magnetozone C20r through C19n; in Hole 1051A from 264.3 cmbsf to 148.36 cmbsf, equivalent to upper magnetozone C20r through upper C19r.

Derivation of name: this species is named for its superficial similarity to *Entogoniopsis foveata* (Greville) Witkowski, Sims, Strelnikova and Williams in Witkowski et al. (2015).

***Fenneria nascens* Bryłka and J. Witkowski, n. sp.** (Pl. II, Fig. 18; Pl. IV, Figs. 1–2)

Holotype: University of Szczecin Herbarium, SZCZ 26942 (Pl. II, Fig. 18)

Description: Frustules subrectangular in girdle view. Valves tripolar, with straight to gently concave sides, and usually pointed poles. Valve face gently undulate, with slightly raised poles and valve face center. Entire valve face perforated by poroid areolae of variable diameter. Areolation density variable, with numerous small poroids scattered in between the areolae. At the poles, the perforations are markedly smaller, but with no discernible pseudocellus. Small granules present at the summits of the polar elevations. In the center of the valve face, there are two rimoportulae that open to the exterior as short tubes. Internal openings in the form of simple slits. The valve face is surrounded by a marginal ridge that is generally level with the summits of the polar elevations. Mantle shallow, steep, with prominent serrations along the free edge. On the underside, distinct hyaline pseudosepta are visible at the poles. Also on the valve interior, there is a network of short internal costae extending along each valve margin.

Type material: Sample ODP 171B-1051A-50X-3, 50–51 cm (sub-bottom depth: 463.40 cmbsf).

Type level: lower Eocene, within magnetozone C24r.

Stratigraphic range: in Hole 1050A: 257.78 through 154.2 cmbsf, equivalent to uppermost magnetozone C25r through uppermost C22r; in Hole 1051A: 534.3 cmbsf through 391.84 cmbsf, equivalent to upper magnetozone C25r through lower C22n.

Derivation of name: nascens (Latin for “being born”), in allusion to the early history of the genus *Fenneria* that this species represents.

New status:

Hemiaulus mesolepta (Grunow) J. Witkowski, stat. nov. (Pl. I, Fig. 13)
Basionym: *Hemiaulus polycistinorum* var. *mesolepta* Grunow (1884)

New combination:

***Proboscia ciesielskii* (Fenner) J. Witkowski, comb. nov.** (Pl. III, Figs. 1–2)
Basionym: *Hemiaulus? ciesielskii* Fenner (1991), p. 137, pl. 1., figs. 5–6

Appendix B. Supplementary data

Supplementary data to this article can be found online at https://doi.org/10.1016/j.margeo.2020.106168.

References

Agnini, C., Fornaciari, E., Raffi, I., Catanzariti, R., Pälike, H., Backman, J., Rio, D., 2014. Biozonation and biochronology of Paleogene calcareous nannofossils from low and middle latitudes. Newsl. Stratigr. 47, 131–181.

Aleksandrova, G.N., Oreshkina, T.V., Iakovleva, A.I., Radionova, E.P., 2012. Late Paleocene-early Eocene diatoms and dinocysts from biosiliceous facies of the Middle Trans-Urals Region. Stratigr. Geol. Correl. 20, 380–404.

Aubry, M.-P., 1995. From chronology to stratigraphy: interpreting the lower and middle Eocene stratigraphic record in the Atlantic Ocean. In: Berggren, W.A., Kent, D.V., Aubry, M.-P., Hardenbol, J. (Eds.), Geochronology, Time Scales, and Global Stratigraphic Correlation. SEPM Special Publication 54pp. 213–274.

Bains, S., Corfield, R.M., Norris, R.D., 1999. Mechanisms of climate warming at the end of

the Paleocene. Science 285, 724–727.
Bains, S., Norris, R.D., Corfield, R.M., Faul, K.L., 2000. Termination of global warmth at the Palaeocene/Eocene boundary through productivity feedback. Nature 407, 171–174.
Baldauf, J.G., 1984. Cenozoic Diatom Biostratigraphy and Paleoceanography of the Rockall Plateau Region, North Atlantic, Deep Sea Drilling Project Leg 81. Initial Rep. Deep Sea Drill. Proj. 81, 439–478.
Barker, P., Dalziel, I.W.D., et al., 1977. Site 327. Initial Rep. Deep Sea Drill. Proj. 36, 27–86.
Barron, J.A., Bukry, D., Gersonde, R., 2014. Diatom and silicoflagellate biostratigraphy for the late Eocene: ODP 1090 (sub-Antarctic Atlantic). Nova Hedwig. Beih. 143, 1–31.
Barron, J.A., Stickley, C.E., Bukry, D., 2015. Paleoceanographic, and paleoclimatic constraints on the global Eocene diatom and silicoflagellate record. Palaeogeogr. Palaeoclimatol. Palaeoecol. 422, 85–100.
Bornemann, A., D'haenens, S., Norris, R.D., Speijer, R.P., 2016. The demise of the early Eocene greenhouse – decoupled deep and surface water cooling in the eastern North Atlantic. Glob. Planet. Chang. 145, 130–140.
Boyle, P.R., Romans, B.W., Tucholke, B.E., Norris, R.D., Swift, S.A., Sexton, P.F., 2017. Cenozoic North Atlantic deep circulation history recorded in contourite drifts, offshore Newfoundland, Canada. Mar. Geol. 385, 185–203.
Bukry, D., 1977. Coccolith and silicoflagellate stratigraphy, South Atlantic Ocean, Deep Sea Drilling Project Leg 39. Initial Rep. Deep Sea Drill. Proj. 39, 825–839.
Bukry, D., 1978. Cenozoic coccolith, silicoflagellate, and diatom stratigraphy, Deep Sea Drilling Project, Leg 44. Initial Rep. Deep Sea Drill. Proj. 44, 807–863.
Burns, R.E., Andrews, J.E., et al., 1973. Site 208. Initial Rep. Deep Sea Drill. Proj. 21, 271–331.
Cappelli, C., Bown, P.R., Westerhold, T., Bohaty, S.M., de Riu, M., Lobba, V., Yamamoto, Y., Agnini, C., 2019. The early to Middle Eocene transition: an integrated calcareous nannofossil and stable isotope record from the Northwest Atlantic Ocean (Integrated Ocean Drilling Program Site U1410). Paleoceanography and Paleoclimatology 34, 1913–1930.
Caves, J.K., Jost, A.B., Lau, K.V., Maher, K., 2016. Cenozoic carbon cycle imbalances and a variable weathering feedback. Earth Planet. Sci. Lett. 450, 152–163.
Cody, R.D., Levy, R.H., Harwood, D.M., Sadler, P.M., 2008. Thinking outside the zone: high-resolution quantitative diatom biochronology for the Antarctic Neogene. Palaeogeogr. Palaeoclimatol. Palaeoecol. 260, 92–121.
Cody, R.D., Levy, R.H., Crampton, J., Naish, T., Wilson, G., Harwood, D.M., 2012. Selection and stability of quantitative stratigraphic age models: Plio-Pleistocene glaciomarine sediments in the ANDRILL 1B drillcore, McMurdo Ice Shelf. Gobal and Planetary Change 96-97, 143–156.
Conley, D.J., Frings, P.J., Fontorbe, G., Clymans, W., Stadmark, J., Hendry, K.R., Marron, A.O., De La Rocha, C., 2017. Biosilicification drives a decline of dissolved Si in the oceans through geologic time. Frontiers in Marine Science 4, 397.
Cramer, B.S., Wright, J.D., Kent, D.V., Aubry, M.-P., 2003. Orbital climate forcing of δ^{13}C excursions in the late Paleocene-early Eocene (chrons C24n-C25n). Paleoceanography 18, 1097.
Crampton, J.S., Cody, R.D., Levy, R., Harwood, D., McKay, R., Naish, T.R., 2016. Southern Ocean phytoplankton turnover in response to stepwise Antarctic cooling over the past 15 million years. Proc. Natl. Acad. Sci. U. S. A. 113, 6868–6873.
DeMaster, D.J., 2014. The diagenesis of biogenic silica: chemical transformations occurring in the water column, seabed, and crust. In: Holland, H.D., Turekian, K.K. (Eds.), Treatise on Geochemistry, 2nd edition. vol. 9. pp. 103–111.
DePrado, C., Ling, H.-Y., 1981. Early to early-middle Paleocene diatom zonation. Antarct. J. US 16, 124–125.
Edgar, K.M., Wilson, P.A., Sexton, P.F., Gibbs, S.J., Roberts, A.P., Norris, R.D., 2010. New biostratigraphic, magnetostratigraphic and isotopic insights into the Middle Eocene Climatic Optimum in low latitudes. Palaeogeogr. Palaeoclimatol. Palaeoecol. 297, 670–682.
Edwards, L.E., 1989. Supplemented graphic correlation: a powerful tool for paleontologists and nonpaleontologists. Palaios 4, 127–143.
Edwards, L.E., 1995. Graphic correlation: some guidelines on theory and practice and how they relate to reality. SEPM Spec. Publ. 53, 45–50.
Egan, K.E., Rickaby, R.E.M., Hendry, K.R., Halliday, A.N., 2013. Opening the gateways for diatoms primes Earth for Antarctic glaciation. Earth Planet. Sci. Lett. 375, 34–43.
Egger, L.M., Śliwińska, K.K., van Peer, T.E., Liebrand, D., Lippert, P.C., Friedrich, O., Wilson, P.A., Norris, R.D., Pross, J., 2016. Magnetostratigraphically-calibrated dinoflagellate cyst bioevents for the uppermost Eocene to lowermost Miocene of the western North Atlantic (IODP Expedition 342, Paleogene Newfoundland sediment drifts). Rev. Palaeobot. Palynol. 234, 159–185.
Eldrett, J.S., Harding, I.C., Firth, J.V., Roberts, A.P., 2004. Magnetostratigraphic calibration of Eocene–Oligocene dinoflagellate cyst biostratigraphy from the Norwegian–Greenland Sea. Mar. Geol. 204, 91–127.
Fenner, J., 1977. Cenozoic diatom biostratigraphy of the equatorial and southern Atlantic Ocean. Initial Reports of the Deep Sea Drilling Project 39 (supplement), 491–624.
Fenner, J., 1984. Eocene-Oligocene planktic diatom stratigraphy in the low latitudes and the high southern latitudes. Micropaleontology 30, 319–342.
Fenner, J., 1991. Taxonomy, stratigraphy, and paleoceanographic implications of Paleocene diatoms. Proceedings of the Ocean Drilling Program, Scientific Results 114, 123–154.
Fenner, J., 1994. Diatoms of the Fur Formation, their taxonomy and biostratigraphic interpretation. - results from the Harre borehole, Denmark. Aarhus Geoscience 1, 99–163.
Finkel, Z.V., Katz, M.E., Wright, J.D., Schofield, O.M.E., Falkowski, P.G., 2005. Climatically driven macroevolutionary patterns in the size of marine diatoms over the Cenozoic. Proc. Natl. Acad. Sci. U. S. A. 102, 8927–8932.
Florindo, F., Farmer, R.K., Harwood, D.M., Cody, R.D., Levy, R., Bohaty, S.M., Carter, L., Winkler, A., 2013. Paleomagnetism and biostratigraphy of sediments from Southern Ocean ODP Site 744 (southern Kerguelen Plateau): implications for early-to-middle Miocene climate in Antarctica. Glob. Planet. Chang. 110, 434–454.
Fontorbe, G., Frings, J., De La Rocha, C.L., Hendry, K.R., Conley, D.J., 2016. A silicon depleted North Atlantic since the Palaeogene: evidence from sponge and radiolarian silicon isotopes. Earth Planet. Sci. Lett. 453, 67–77.
Fourtanier, E., 1991. Paleocene and Eocene diatom biostratigraphy and taxonomy of eastern Indian Ocean Site 752. Proceedings of the Ocean Drilling Program, Scientific Results 121, 171–187.
Fourtanier, E., Oscarson, R., 1994. Ultrastructure of some interesting and stratigraphically significant diatom taxa from the upper Paleocene to lower Eocene sedimentss of ODP Site 752, eastern Indian Ocean. In: Kociolek, J.P. (Ed.), Proceedings of the 11th International Diatom Symposium. Memoirs of the California Academy of Sciences 17. pp. 399–410.
Gleser, S.I., Jousé, A.P., 1974. Diatoms and silicoflagellates in the Eocene of the Equatorial Atlantic. In: Jousé, A.P. (Ed.), Mikropaleontologiya okeanov i morei, pp. 49–62.
Gleser, S.I., Sheshukova-Poretzkaja, V.S., 1967. De speciebus tertiariis Barbadossicis ac Novozeelandicis in aeocaeno superiore Ucrainae. Novitates Systematicae Plantarum non Vascularium. vol. 4. pp. 25–37 (in Russian, with Latin title).
Gombos Jr., A.M., 1977. Paleogene and Neogene diatoms from the Falkland Plateau and Malvinas Outer Basin: Leg 36, Deep Sea Drilling Project. Initial Rep. Deep Sea Drill. Proj. 36, 575–687.
Gombos Jr., A.M., 1982. Early and Middle Eocene diatom evolutionary events. Bacillaria 5, 225–243.
Gombos Jr., A.M., 1984. Late Paleocene diatoms in the Cape Basin. Initial Rep. Deep Sea Drill. Proj. 73, 495–511.
Gombos Jr., A.M., 1987. Middle Eocene Diatoms from the North Atlantic, Deep Sea Drilling Project Site 605. Initial Rep. Deep Sea Drill. Proj. 93 (793–399).
Gombos Jr., A.M., Ciesielski, P.F., 1983. Late Eocene to early Miocene diatoms from the Southwest Atlantic. Initial Rep. Deep Sea Drill. Proj. 71, 583–634.
Gradstein, F.M., Ogg, J.G., Schmitz, M.D., Ogg, G.M., 2012. The Geologic Time Scale 2012. 2 Elsevier, Amsterdam (1144 pp).
Greville, R.K., 1865. Descriptions of new and rare Diatoms. Series XVII. Transactions of the Microscopical Society. New Series 13, 97–105.
Harwood, D.M., 1988. Upper Cretaceous and lower Paleocene diatom and silicoflagellate biostratigraphy of Seymour Island, eastern Antarctic Peninsula. Geological Society of America Memoir 169, 55–129.
Hollis, C.J., Rodgers, K.A., Parker, R.J., 1995. Siliceous plankton bloom in the earliest Tertiary of Marlborough, New Zealand. Geology 23, 835–858.
Hollis, C.J., Stickley, C.E., Bijl, P.K., Schiøler, P., Clowes, C.D., Li, X., Campbell, H., 2017. The age of the Takatika Grit, Chatham Islands, New Zealand. Alcheringa 41, 383–396.
Holmes, M.A., Watkins, D.K., Norris, R.D., 2004. Paleocene cyclic sedimentation in the western North Atlantic, ODP Site 1051, Blake Nose. Mar. Geol. 2004, 31–43.
Homann, M., 1991. Die Diatomeen der Fur-Formation (Alttertiär, Limfjorden/Dänemark). Geologisches Jahrbuch Reihe A 123 (285 pp.).
Janus Web Database http://www-odp.tamu.edu/database/ (accessed 16 December 2019).
Jousé, A.P., 1951. Diatomeae et silicoflagellatae aetatis Cretae Superne e Montibus Uralensibus Septentrionalibus. Notulae Systematicae E Sectione Cryptogamica Instituti Botanici Nomine V.L. Komarovii Academiae Scientiarum URSS 7, 42–65 (in Russian).
Jousé, A.P., 1955. Species novae diatomacearum aetatis Paleogenae. Notulae Systematicae E Sectione Cryptogamica Instituti Botanici Nomine V.L. Komarovii Academiae Scientiarum URSS 10, 81–103 (in Russian).
Kamikuri, S.-I., Moore, T.C., Ogane, K., Suzuki, N., Pälike, H., Nishi, H., 2012. Early Eocene to early Miocene radiolarian biostratigraphy from the low-latitude Pacific Ocean. Stratigraphy 9, 77–108.
Khokhlova, I.E., Oreshkina, T.V., 1999. Early Palaeogene siliceous microfossils of the Middle Volga region: stratigraphy and palaeogeography. Geodiversitas 21, 429–451.
Kitchell, J.A., Clark, D.A., Gombos Jr., A.M., 1986. Biological selectivity of extinction: a link between background and mass extinction. Palaios 1, 504–511.
Krotov, A.I., Schibkova, K.G., 1959. Species novae diatomacearum e Palaeogeno Montium Uralensium. Notulae Systematicae E Sectione Cryptogamica Instituti Botanici Nomine V.L. Komarovii Academiae Scientiarum URSS 12, 112–129 (in Russian).
Ling, H.Y., 1985. Paleogene Silicoflagellates and Ebridians from the Goban Spur, Northeastern Atlantic. Initial Rep. Deep Sea Drill. Proj. 80, 663–668.
Luciani, V., Giusberti, L., 2014. Reassessment of the early-middle Eocene planktic foraminiferal biomagnetochronology: new evidence from the Tethyan Possagno section (NE Italy) and western North Atlantic Ocean ODP Site 1051. J. Foraminifer. Res. 44, 187–201.
Luciani, V., Dickens, G.R., Backman, J., Fornaciari, E., Giusberti, L., Agnini, C., D'Onoforio, R., 2016. Major perturbations in the global carbon cycle and photosymbiont-bearing planktic foraminifera during the early Eocene. Clim. Past 12, 981–1007.
Luciani, V., D'Onoforio, R., Dickens, G.R., Wade, B.S., 2017. Did photosymbiont bleaching lead to the demise of planktic foraminifer *Morozovella* at the early Eocene climatic optimum? Paleoceanography and Paleoclimatology 32, 1115–1136.
MacLeod, N., Sadler, P., 1995. Estimating the line of correlation. SEPM Spec. Publ. 53, 51–64.
Martini, E., 1971. Standard Tertiary and Quaternary calcareous nannoplankton zonation. In: Proceedings of the 2nd Planktonic Conference, Roma, 1970, pp. 739–785.
McLean, H., Barron, J.A., 1988. A late middle Eocene diatomite in northwestern Baja California Sur, Mexico: implications for tectonic translation. In: Filewicz, M.V.,

Squires, R.L. (Eds.), Paleogene Stratigraphy, West Coast of North America, Pacific Section, SEPM, West Coast Paleogene Symposium. 58. pp. 1–8.

Mita, I., 2001. Data report: early to late Eocene calcareous nannofossil assemblages of Sites 1051 and 1052, Blake Nose, Northwestern Atlantic Ocean. In: Proceedings of the Ocean Drilling Program, Scientific Results 171B, pp. 1–28 (Online).

Mitlehner, A., 1995. *Cylindrospira*, a new diatom genus from the Palaeogene of Denmark with palaeoecological significance. Diatom Research 10, 321–331.

Mukhina, V.V., 1976. Species composition of the Late Paleocene diatoms and silicoflagellates in the Indian Ocean. Micropaleontology 22, 151–158.

Nicolo, M.J., Dickens, G.R., Hollis, C.J., Zachos, J.C., 2007. Multiple early Eocene hyperthermals: their sedimentary expression on the New Zealand continental margin and in the deep sea. Geology 35, 699–702.

Nigrini, C., Sanfilippo, A., Moore Jr., T.J., 2006. Cenozoic radiolarian biostratigraphy: a magnetobiostratigraphic chronology of cenozoic sequences from ODP sites 1218, 1219, and 1220, equatorial Pacific. In: Proceedings of the Ocean Drilling Program, Scientific results 199, pp. 1–76 (Online).

Nikolaev, V.A., Harwood, D.M., 2002. Morphology, Taxonomy and System Classification of Centric Diatoms. Nauka, St. Petersburg (118 pp.).

Norris, R.D., Kroon, D., et al., 1998a. Introduction. Proceedings of the Ocean Drilling Program, Initial Reports 171B, 5–10.

Norris, R.D., Kroon, D., et al., 1998b. Site 1049. Proceedings of the Ocean Drilling Program, Initial Reports 171B, 47–92.

Norris, R.D., Kroon, D., et al., 1998c. Site 1050. Proceedings of the Ocean Drilling Program, Initial Reports 171B, 93–170.

Norris, R.D., Kroon, D., et al., 1998d. Site 1051. Proceedings of the Ocean Drilling Program, Initial Reports 171B, 171–240.

Norris, R.D., Kroon, D., et al., 1998e. Site 1052. Proceedings of the Ocean Drilling Program, Initial Reports 171B, 241–320.

Norris, R.D., Kroon, D., et al., 1998f. Site 1053. Proceedings of the Ocean Drilling Program, Initial Reports 171B, 321–348.

Norris, R.D., Klaus, A., Kroon, D., 2001. Mid-Eocene deep water, the Late Palaeocene Thermal Maximum and continental slope mass wasting during the Cretaceous-Palaeogene impact. In: Kroon, D., Norris, R.D., Klaus, A. (Eds.), Western North Atlantic Palaeogene and Cretaceous Palaeoceanography. Geological Society of London Special Publications 183. pp. 23–48.

Norris, R.D., Wilson, P.A., et al., 2014a. Methods. Proceedings of the Integrated Ocean Drilling Program. vol. 342. pp. 1–78 (Online).

Norris, R.D., Wilson, P.A., et al., 2014b. Site U1410. Proceedings of the Integrated Ocean Drilling Program. vol. 342. pp. 1–87 (Online).

Ocean Drilling Stratigraphic Network http://www.odsn.de (accessed 16 December 2019).

Ogg, J.G., Bardot, L., 2001. Aptian through Eocene magnetostratigraphic correlation of the Blake Nose Transect (Leg 171B), Florida continental margin. In: Proceedings of the Ocean Drilling Program, Scientific Results. vol. 171B. pp. 1–58 (Online).

Okada, H., Bukry, D., 1980. Supplementary modification and introduction of code numbers to the low-latitude coccolith biostratigraphic zonation (Bukry, 1973; 1975). Mar. Micropaleontol. 5, 321–325.

Oreshkina, T.V., Aleksandrova, G.N., 2007. Terminal Paleocene of the Volga Middle Reaches: biostratigraphy and paleosettings. Stratigr. Geol. Correl. 15, 206–230.

Oreshkina, T.V., Aleksandrova, G.N., 2017. Paleocene-lower Eocene paleontological record of the Ulyanovsk-Syzran facial district, Volga-Peri-Caspian Region. Stratigr. Geol. Correl. 25, 307–332.

Oreshkina, T.V., Oberhänsli, H., 2003. Diatom turnover in the early Paleogene diatomite of the Sengiley section, Middle Povolzhie, Russia: a response to the initial Eocene thermal maximum? Geological Society of America Special Paper 369, 169–179.

Penman, D., 2016. Silicate weathering and North Atlantic silica burial during the Paleocene-Eocene Thermal Maximum. Geology 44, 731–734.

Penman, D., Keller, A., D'haenens, S., Turner, S.K., Hull, P.M., 2019. Atlantic deep-sea cherts associated with Eocene hyperthermal events. Paleoceanography and Paleoclimatology 34, 287–299.

Piela, C., Lyle, M., Marcantonio, F., Baldauf, J., Olivarez Lyle, A., 2012. Biogenic sedimentation in the equatorial Pacific: carbon cycling and paleoproduction, 12–24 Ma. Paleoceanography 27, 1–18 PA2204.

van der Ploeg, R., Selby, D., Cramwinckel, M.J., Li, Y., Bohaty, S.M., Middelburg, J.J., Sluijs, A., 2018. Middle Eocene greenhouse warming facilitated by diminished weathering feedback. Nat. Commun. 9, 2877.

Radionova, Khokhlova, 1994. Paleogene episodes of biogenic silica accumulation in the northern Caucasus and adjacent Tethyan regions. Stratigr. Geol. Correl. 2, 61–169.

Renaudie, J., Danelian, T., Saint Martin, S., Le Callonnec, L., Tribovillard, N., 2010. Siliceous phytoplankton response to a Middle Eocene warming event recorded in the tropical Atlantic (Demerara Rise, ODP Site 1260A). Palaeogeogr. Palaeoclimatol. Palaeoecol. 286, 121–134.

Renaudie, J., Drews, E.-L., Böhne, S., 2018. The Paleocene record of marine diatoms in deep-sea sediments. Fossil Record 21, 183–205.

Röhl, U., Ogg, J.G., Geib, T.L., Wefer, G., 2001. Astronomical calibration of the Danian time scale. In: Kroon, D., Norris, R.D., Klaus, A. (Eds.), Western North Atlantic Palaeogene and Cretaceous Palaeoceanography. Geological Society of London Special Publications 183. pp. 163–183.

Röhl, U., Norris, R.D., Ogg, J.G., 2003. Cyclostratigraphy of upper Paleocene and lower Eocene sediments at Blake Nose Site 1051 (western North Atlantic). Geological Society of America Special Paper 369, 567–589.

Ross, R., 1995. A revision of *Rutilaria* Greville (Bacillariophyta). Bulletin of British Museum (Natural history). Botany Series 25, 1–93.

Ross, R., Sims, P.A., 1985. Some genera of the Biddulphiaceae (diatoms) with interlocking linking spines. Bulletin of the British Museum (Natural History) 13, 277–381.

Round, F.E., Crawford, R.M., Mann, D.G., 1990. The Diatoms. Biology and Morphology of the Genera. Cambridge University Press, Cambridge (747 pp.).

Sanfilippo, A., Blome, C., 2001. Biostratigraphic implications of mid-latitude Palaeocene-Eocene radiolarian faunas from Hole 1051A, ODP Leg 171B, Blake Nose, western North Atlantic. In: Kroon, D., Norris, R.D., Klaus, A. (Eds.), Western North Atlantic Palaeogene and Cretaceous Palaeoceanography. Geological Society of London Special Publications 183. pp. 185–224.

Sanfilippo, A., Nigrini, C., 1998. Code numbers for Cenozoic low latitude radiolarian biostratigraphic zones and GPTS conversion tables. Mar. Micropaleontol. 33, 109–156.

Scherer, R.P., Gladenkov, A.Yu., Barron, J.A., 2007. Methods and applications of Cenozoic marine diatom biostratigraphy. In: Starratt, S.W. (Ed.), Pond Scum to Carbon Sink. Geological and Environmenta Applications of the Diatoms. The Paleontological Society Papers 13. pp. 61–83.

Schrader, H.-J., 1969. Die pennaten Diatomeen aus dem Obereozän von Oamaru, Neuseeland. Nova Hedwig. Beih. 28, 1–124.

Schrader, H.-J., Gersonde, R., 1978. Diatoms and silicoflagellates. In: Zachariasse, W.J. (Ed.), Micropaleontological Counting Methods and Techniques: An Exercise of an Eight Metres Section of the Lower Pliocene of Cap Rossello. Sicily. Utrecht Micropalaeontological Bulletin 17. pp. 129–176.

Shaw, A.B., 1964. Time in Stratigraphy. McGraw-Hill, New York (365 pp.).

Sims, P.A., 1988. The fossil genus *Trochosira*, its morphology, taxonomy and systematics. Diatom Research 3, 245–257.

Sims, P.A., 1998. The early history of the Biddulphiales. I. The genus *Medlinia* gen. nov. Diatom Research 13, 337–374.

Sims, P.A., Mann, D.G., Medlin, L.K., 2006. Evolution of the diatoms: insights from fossil, biological and molecular data. Phycologia 45, 361–402.

Sims, P.A., Witkowski, J., César, E., 2020. *Crawfordia* gen. nov.: Solving the Riddle of *Triceratium hardmannianum* Grev. (Bacillariophyta). Submitted to Nova Hedwigia, Beiheft. (under review).

Strelnikova, N.I., 1971. Species novae Bacillariophytorum e sedimentis Cretae posterioris in declivitate orientali partis polaris ac praepolaris montium Uralensium. Novitates Systematicae Plantarum non Vascularium. vol. 8. pp. 41–50 (in Russian, with Latin title).

Strelnikova, N.I., 1974. Diatomei pozdnego mela. Nauka, Leningrad (201 pp., in Russian).

Strelnikova, N.I., 1992. Paleogenov'ye diatomov'ye vodorosli. St. Petersburg University Press, St. Petersburg (311 pp.).

Strelnikova, N.I., Nikitina, E.N., 2018. Some Cretaceous and Paleogene *Trinacria, Medlinia, Sheshukovia* species from Russia (Volga river region, Western Siberia), Kazakhstan and Ukraine. Nova Hedwig. Beih. 147, 193–228.

Suto, I., 2004a. Taxonomy of the diatom resting spore form genus *Liradiscus* Greville and its stratigraphic significance. Micropaleontology 50, 59–79.

Suto, I., 2004b. Fossil marine diatom resting spore morpho-genus *Xanthiopyxis* Ehrenberg in the North Pacific and Norwegian Sea. Paleontological Research 8, 283–310.

Suto, I., 2006. Taxonomy of the fossil marine diatom resting spore morpho-genera *Xanthioisthmus* Suto gen. nov. and *Quadrocistella* Suto gen. nov. in the North Pacific and Norwegian Sea. J. Micropalaeontol. 25, 3–22.

Suto, I., 2007. The Oligocene and Miocene record of the diatom resting spore genus *Liradiscus* Greville in the Norwegian Sea. Micropaleontology 53, 145–159.

Wade, B.S., Pearson, P.N., Berggren, W.A., Pälike, H., 2011. Review and revision of Cenozoic tropical planktonic foraminiferal biostratigraphy and calibration to the geomagnetic polarity and astronomical time scale. Earth Sci. Rev. 104, 111–142.

Westerhold, T., Röhl, U., Frederichs, T., Agnini, C., Raffi, I., Zachos, J.C., Wilkens, R.H., 2017. Astronomical calibration of the Ypresian timescale: implications for seafloor spreading rates and the chaotic behavior of the solar system? Clim. Past 13, 1129–1152.

Westerhold, T., Röhl, U., Donner, B., Zachos, J.C., 2018. Global extent of early Eocene hyperthermal events: a new Pacific benthic foraminiferal isotope record from Shatsky Rise (ODP Site 1209). Paleoceanography and Paleoclimatology 33, 626–642.

Witkowski, J., 2018. From museum drawers to ocean drilling: *Fenneria* gen. nov. (Bacillariophyta) offers new insights into Eocene marine diatom biostratigraphy and palaeobiogeography. Acta Geol. Pol. 68, 53–88.

Witkowski, J., Harwood, D.M., Chin, K., 2011. Taxonomic composition, paleoecology and biostratigraphy of Late Cretaceous diatoms from Devons Island, Nunavut, Canadian High Arctic. Cretac. Res. 32, 277–300.

Witkowski, J., Bohaty, S.M., McCartney, K., Harwood, D.M., 2012. Enhanced siliceous plankton productivity in response to middle Eocene warming at Southern Ocean ODP Sites 748 and 749. Palaeogeogr. Palaeoclimatol. Palaeoecol. 326–328, 78–94.

Witkowski, J., Bohaty, S.M., Edgar, K.M., Harwood, D.M., 2014. Rapid fluctuations in mid-latitude siliceous plankton production during the Middle Eocene Climatic Optimum (ODP Site 1051, western North Atlantic). Mar. Micropaleontol. 106, 110–129.

Witkowski, J., Sims, P.A., Strelnikova, N.I., Williams, D.M., 2015. *Entogoniopsis* gen. nov. and *Trilamina* gen. nov. (Bacillariophyta): a survey of multipolar pseudocellate diatoms with internal costae, including comments on the genus *Sheshukovia* Gleser. Phytotaxa 209, 1–89.

Witkowski, J., Penman, D.E., Bryłka, K., Wade, B.S., Matting, S., Harwood, D.M., Bohaty, S.M., 2020. Lower Paleocene through upper Eocene chert and porcellanite in the Atlantic Ocean: testing the inorganic origin hypothesis. In: Submitted to Palaeogeography, Palaeoclimatology, Palaeoecology, (under review).